Towards silicon quantum dot solar cells : comparing morphological properties and conduction phenomena in Si quantum dot single layers and multilayers

Kavita Surana

UNIVERSITÉ DE GRENOBLE

THÈSE

Pour obtenir le grade de

DOCTEUR DE L'UNIVERSITÉ DE GRENOBLE

Spécialité : **Matériaux, Mécaniques, Génie Civil, Electrochimie**

Arrêté ministériel : 7 août 2006

Présentée par

Kavita SURANA

Thèse dirigée par **Daniel BELLET** et
Co-encadrée par **Pierre MUR** et **Philippe THONY**

préparée au sein du **Laboratoire :**
Laboratoire Composants Electroniques pour l'Energie (CEA/Leti/LC2E)
dans **l'École Doctorale :** *Ingénierie - Matériaux, Mécanique, Environnement, Energétique, Procédés, Production*

Towards Silicon Quantum Dot Solar Cells:
Comparing Morphological Properties and Conduction Phenomena in Si Quantum Dot Single Layers and Multilayers

Thèse soutenue publiquement le *21 septembre 2011*
devant le jury composé de :

M. Gavin CONIBEER
Professeur associé et directeur adjoint du "Photovoltaic Centre of Excellence", Université de New South Wales, Australie, Président
M. Fabrice GOURBILLEAU
Directeur de Recherche, CNRS, France, Rapporteur
M. Salvatore LOMBARDO
Directeur de Recherche, CNR, Italie, Rapporteur
M. Daniel BELLET
Professeur, Grenoble-INP, France, Examinateur
M. Pierre MUR
Ingénieur-chercheur, CEA-Leti, France, Examinateur
M. Philippe THONY
Ingénieur-chercheur, CEA-Liten/Ines, France, Examinateur
Mme. Rose-Marie CAPELLA
Responsable du domaine scientifique Nanotechnologies, DGA, France, Examinateur

UNIVERSITÉ DE GRENOBLE

THESIS

To obtain the rank of

DOCTOR OF THE UNIVERSITY OF GRENOBLE

Speciality: **Materials, Mechanical, Civil Engineering, Electrochemistry**

Ministerial Order: 7 August 2006

Presented by

Kavita SURANA

Thesis advisor: **Daniel BELLET**
Co-supervisors: **Pierre MUR** and **Philippe THONY**

prepared in the **Laboratory :**
Power Devices Laboratory (CEA/Leti/LC2E)
in the **Doctoral School :** *Engineering - Materials, Mechanics, Environment, Energy, Process, Production*

Towards Silicon Quantum Dot Solar Cells:
Comparing Morphological Properties and Conduction Phenomena in Si Quantum Dot Single Layers and Multilayers

Thesis publicly defended on *21st September 2011*
before the following committee:

Gavin CONIBEER
Associate Professor and Deputy Director of Photovoltaic Centre of Excellence, University of New South Wales, Australia, President
Fabrice GOURBILLEAU
Research Director, CNRS, France, Reviewer
Salvatore LOMBARDO
Research Manager, CNR, Italy, Reviewer
Daniel BELLET
Professor, INP Grenoble, France, Examiner
Pierre MUR
Research Engineer, CEA-Leti, France, Examiner
Philippe THONY
Research Engineer, CEA-Liten/Ines, France, Examiner
Rose-Marie CAPELLA
Head of Nanotechnologies Scientific Domain, DGA, Examiner

Acknowledgements

Thanking people in just a few words after working with them for three years makes these few pages the hardest and most incomplete part of this thesis. I learnt a lot of things from a lot of people, and it was of course more than just about silicon quantum dots. I know I have too many people to thank, and I apologize to those that I am surely likely to forget.

First of all, I would like to thank the director of ex-D2NT, Olivier Demolliens for the opportunity to work on this very interesting topic. Thanks to Jean-René Lequepeys and Olivier Faynot, the heads of DCOS and SCME respectively. Also thanks to Thierry Billon, head of L2MA and then of LC2E for always being very approachable and concerned. Thanks to DGA for co-funding this thesis.

Next, thank you to all the jury members for their time and attention, for their constructive criticism and also for coming all the way to Grenoble, from literally around the world.

I was lucky enough to have three supervisors, all very different but equally important. This work would surely not have been possible without their vision. Thanks to Daniel Bellet, my PhD director at LMGP, for his patience, cheerfulness and valuable inputs. Thanks to Philippe Thony, my supervisor at INES, for his sound advice and remarks, that were always very precise but still made me think. And thanks to Pierre Mur, my supervisor at LETI, who I worked and interacted with most often, for his optimism, confidence in me, and work ethics that I greatly respect and hope to emulate in the future.

I also had the opportunity to work with a large number of people, for a lot of experiments but also for very valuable discussions. Thanks Mathieu Baudrit for his enthusiasm that led to some good results. Hadrien Lepage for essential inputs on electrical transport mechanisms, and also Jean-Marie Lebrun, Gilles Poulain who worked on this topic. Gilles Le Carval for his advice on all things related to this thesis. Yves Morand and Jean-Michel Pedini for their help with lots and device fabrication. Laurent Vandroux, Catherine Charrier and everyone in the Zone Dépot, Karim Yckache and

Zone Recuit for helping me make those really great layers. François de Crecy for the ultra-thin layers that solved a lot of problems, design of experiments and other important discussions. Dominique Lafond for TEM. Beatrice Doisneau also for TEM. Emmanuel Nolot and Christophe Licitra for their training and important inputs on ellipsometry. Pierre Gidon for the incredible effort and analysis that went into obtaining spectral response measurements. Guillaume Rodriguez for ITO and Frédéric Gonzatti for polysilicon depositions. The parametric electrical tests team for help with the characterizations. Xavier Garros, Gabriel Molas and Luca Perniola for their time and help with analysis of electrical measurements. Jaques Cluzel, Patrick Grosgeorges and Denis Blachier for electrical characterizations, low temperature experiments, and also for their help in lifting the cryo tube that was big and heavy and really not made for short people. Also, thanks to Veronique Robert for her help with the patents.

These three years wouldn't be the same without a lot of people, who still correct my French like only true friends would do, make great food especially cakes, and of course, never talk about football. Yoann for knowing all the answers to everything, and along with Thibaud for the endless entertainment in and outside work, especially on Wednesdays. Loubs for his bottomless bag of incredible questions counterbalanced by Celine's common sense. Cedric and Ju for their papa-thésard wisdom, which is still valid. Edrisse for les pauses bonbons, and for all the help during and after the thesis. Richard with the super-human vision who can create magical anana cakes with one piercing look. Raul who has sung beautiful melodies in the office and kept me going with the *"there, there"* pat on the back. Sylvia and Audrey for their girl time. Giada, my Italian twin queen. And so many others Agnès, Pierre-Antoine, Emeline, Loïc, Valentina, Romain, Fox, Bilel, Nathalie, Matthew and everyone else who was part of what used to be L2MA...

To my other friends in Grenoble, who I can't even begin to list, thanks for all the great evenings and weekends, and also the much needed *verres* that helped switch off from work and contributed significantly to writing this thesis. Thanks Alex, Chick Corea and Neil Peart for creating all the music that motivated to write. Mr. H for winning the paratha world cup. Thomas and Christian for their hugs, korners and happy-ness.

Karine my *pita* for feeding me a lot of cakes and coffee. Santiago and Jan for all their mountain sports for dummies, and for always looking out for me.

Moving on to those who are more than a thousand kilometres away, thanks Dóri and Igor for being such great friends and for the super holidays. Aravind, for always being there to support everything I do and for being part of all the highs and lows of this thesis. Finally, thanks to my mother from whom I learnt the most valuable lesson, that we must do the hardest of things with a smile.

Abstract

Quantum confined silicon, in the form of silicon quantum dots of diameters 5 nm or less, has the property of bandgap control and light emission. This bandgap engineering gives silicon quantum dots applications in novel photovoltaic devices, while maintaining compatibility with existing silicon technologies. These dots can help reduce lattice thermalisation losses in a single-junction solar cell. This work focusses on the large scale fabrication of silicon quantum dots in SiO_2 using Plasma Enhanced Chemical Vapour Deposition (PECVD), followed by high-temperature annealing. Thick single layers are compared with multilayers for morphological, electrical and optical properties. Devices with these layers are compared with different electrode materials. Film thickness dependent organization of dots is observed in thick single layer structures which demonstrate improved electrical conductivity, but poor optical response. Multilayer films demonstrate augmented and controlled Si bandgaps and improved absorption in the blue-green visible range, accompanied by poor electrical conductivity. The improved optical properties are a promising sign for any potential photovoltaic integration.

Keywords: Photovoltaics, silicon, nanostructures, quantum dots, solar cells, nanocrystals, third generation.

Résumé

Le confinement quantique dans le silicium, sous forme de boîtes quantiques de silicium de diamètre 5 nm, permet de contrôler le bandgap et donc l'émission de lumière. Cette ingénierie du bandgap des nanocristaux de silicium est utile pour les applications photovoltaïques avancées et présente l'avantage de conserver la compatibilité avec les technologies silicium existantes. Ces boîtes quantiques peuvent aider à réduire les pertes par thermalisation dans une cellule solaire homo-jonction. Ce travail se concentre sur la fabrication à grande échelle des nanocristaux de silicium dans SiO_2 en utilisant le Dépôt Chimique en Phase Vapeur assisté par Plasma (PECVD), suivi d'un recuit à haute température. Des monocouches sont comparées avec des multicouches pour les propriétés morphologiques, électriques et optiques et des dispositifs avec ces différents couches sont comparés. Dans le cas d'une structure monocouche, l'épaisseur de la couche contrôle l'organisation des nanocristaux et permet de mettre en évidence l'amélioration de la conductivité électrique, avec cependant une réponse optique faible. Les multicouches montrent un bandgap du Si augmentée et contôlée, avec une meilleure absorption dans la gamme bleu-vert visible, accompagnée d'une conductivité électrique faible. L'amélioration de ces propriétés optiques est un signe prometteur pour une potentielle intégration photovoltaïque.

Mots-clés: photovoltaïque, silicium, nanostructures, boîtes quantiques, cellules solaires, nanocristaux, troisième génération.

Contents

List of Figures **8**

List of Tables **9**

Abbreviations and Acronyms **9**

Introduction **17**

1 An Introduction to Si Quantum Dots **21**

1.1 Silicon Technology - More than Microelectronics 21

1.2 Silicon Nanotechnology - Beyond Bulk Silicon 23

1.2.1 Quantum Confinement in Silicon 24

1.2.2 Applications of Silicon Nanocrystals 27

1.3 Silicon in Solar Cells 29

1.3.1 Photovoltaic Technologies 30

1.4 Si Quantum Dots in Third Generation Photovoltaics 31

1.4.1 Efficiency Losses in a Solar Cell 31

1.4.2 Quantum Dots in Photovoltaics 33

1.4.3 Si Quantum Dot Photovoltaics 34

1.5 Aim of this Thesis 37

2 Developing Single Layers of Si Quantum Dots **39**

2.1 Introduction 39

2.1.1 Fabrication Techniques 39

2.2 Synthesis of Si Quantum Dots in Silicon Dioxide 41

2.2.1 Plasma Enhanced Chemical Vapour Deposition 41

2.2.2 Thermal Annealing 43

2.3 Composition of the Silicon Rich Oxide Layers . . . 45
2.3.1 Fourier Transform Infrared Spectroscopy . . . 45
2.3.2 Spectroscopic Ellipsometry . . . 48
2.3.3 Summary . . . 53
2.4 Quantum Confinement in Si Quantum Dots . . . 54
2.4.1 Photoluminescence Spectroscopy . . . 54
2.4.2 Transmission Electron Microscopy . . . 56
2.4.3 Grazing Incidence X-ray Diffraction . . . 58
2.5 Summary of Characterization Techniques . . . 60

3 Film Thickness Dependent Order in Single Layers 63
3.1 Spatial Organization of Si Quantum Dots . . . 63
3.1.1 Elucidation of Thickness Dependent Order in Si Quantum Dots . . . 66
3.2 Electrical Conduction in Si Quantum Dot Films . . . 67
3.2.1 Characterizing Conduction Phenomena . . . 67
3.2.2 Current-Voltage Characteristics of Si Quantum Dot Layers . . . 68
3.2.3 Low Temperature Conductivity . . . 68
3.2.4 Capacitance-Voltage and Photocarrier Generation . . . 73
3.3 Summary and Concluding Remarks . . . 73

4 From Single Layers to Multilayers 75
4.1 Single Layers Structures . . . 75
4.1.1 Challenges for Multilayer Depositions . . . 76
4.1.2 Preliminary Experiments . . . 76
4.1.3 Controlling PECVD Depositions . . . 79
4.2 Design of Experiments . . . 80
4.2.1 Introduction . . . 80
4.2.2 Description of the Experimental Design . . . 80
4.2.3 Results of the Experimental Design . . . 82
4.3 Optimizing Annealing Conditions . . . 87
4.3.1 Structural Characterizations of Different Annealed Films . . . 87
4.3.2 Influence of Annealing Conditions on Photoluminescence . . . 88
4.3.3 Energy Filtered Transmission Electron Microscopy (EFTEM) . . . 90
4.4 Photoluminescence Studies of the Multilayer Structure . . . 92

4.4.1 Varying SiO_2 Thickness . . . 92
4.4.2 Comparison with Thick Single Layer . . . 93
4.4.3 Varying Number of Multilayer Stacks . . . 94
4.4.4 Discussion . . . 94
4.5 Summary and Conclusions . . . 95

5 Electrical and Optical Properties of Single Layers and Multiple Bilayers 97
5.1 Introduction . . . 97
5.2 Device Materials . . . 97
5.2.1 Bandgap Optimization in the Active Layer . . . 97
5.2.2 Electrode and Substrate Materials . . . 100
5.3 Electrical Conduction in Multilayers . . . 102
5.4 Low-Temperature Electrical Conductivity . . . 106
5.4.1 Poole-Frenkel Conduction . . . 108
5.4.2 Elucidating Conduction Mechanisms in Si Quantum Dots . . . 109
5.5 Illumination Effects on Silicon Nanocrystals . . . 112
5.6 Summary . . . 114

Conclusion and Outlook 117

References 120

A Quantum Confinement in Nanocrystals 135

B Experimental Design 139

Résumé en Français 142

List of Figures

1.1 Schematic energy band diagram of silicon showing electron excitation and absorption in silicon. . . . 23
1.2 Idealized density of states for quantum confined structures showing discrete energy levels in quantum dots. . . . 24
1.3 Comparison of theoretical calculations for band gap evolution with silicon quantum dot diameter. . . . 25
1.4 Bulk band alignments between crystalline silicon and SiO_2, Si_3N_4 and SiC. 26
1.5 Si quantum dot applications in microelectronics, photonics and photovoltaics. 27
1.6 Historical evolution of photovoltaic technology market share and future trends. . . . 29
1.7 Photovoltaic technology status and prospects till 2030. . . . 31
1.8 Solar spectral irradiance with Air Mass (AM) 1.5. . . . 32
1.9 Loss mechanisms in solar cells 32
1.10 Efficiency limits for different photovoltaic concepts. . . . 33
1.11 Si quantum dot based photovoltaic device with reported 10.6% efficiency. . 34
1.12 Schematic of all-Si based tandem solar cell. . . . 35
1.13 Schematic of a hot carrier solar cell. . . . 36

2.1 Schematic diagram of a plasma enhanced chemical vapour deposition (PECVD) reactor. . . . 41
2.2 Silicon quantum dot formation on high temperature annealing of silicon rich oxides. . . . 43
2.3 Schematic of a typical FTIR setup with a Michelson interferometer. . . . 45
2.4 Change in FTIR with annealing and with thickness of silicon rich oxides. . 47
2.5 De-convoluted FTIR peaks confirming Si-O stretching of SiO_2 in annealed films. . . . 47

2.6 Schematic of the principle and setup used in spectroscopic ellipsometry. . . 49
2.7 Spectroscopic ellipsometry data showing variation in refractive index and extinction coefficient with energy for annealed SiO_x films. 51
2.8 Optical indices of annealed films with silicon quantum dots. 51
2.9 Comparison of ellipsometry fits with the Tauc-Lorentz dispersion model and the Bruggeman Effective Medium Approximation. 52
2.10 Photoluminescence intensity versus wavelength for thick single layer films. . 55
2.11 Plan-view TEM micrograph, corresponding EFTEM and size distribution of quantum dots for sample Q30. 57
2.12 Grazing incidence x-ray diffraction patterns showing presence of crystalline silicon quantum dots. 59

3.1 Plan-view EFTEM micrograph for sample Q75 showing silicon dislocations and lattice defects. 64
3.2 Plan-view TEM micrographs with copper re-deposition on silicon quantum dots show an evolution from randomly arranged quantum dots to an ordered spatial distribution. 64
3.3 Plan-view EFTEM micrograph for Q75 confirming ordered silicon quantum dots in dark zones. 65
3.4 Fabrication process for formation of capacitor-like devices with electrical contacts, and Al contact electrode. 67
3.5 Capacitive devices used for electrical characterizations of quantum dots. . . 68
3.6 Current density vs voltage for Q30, Q50 and Q75 show decreasing conduction in thicker films. 69
3.7 Low temperature current-voltage measurements and Arrhenius plots for single layers, showing different electrical conduction mechanisms. 70
3.8 Low temperature electrical conductivity comparison for single layers. . . . 71
3.9 C-V measurements at 1 MHz for Q75 ordered films show hysteresis broadening under ambient illumination, confirming photocarrier generation. . . . 73

4.1 Fabrication of silicon quantum dot multilayers with dot-size control. 76
4.2 Effect of inter-electrode distance on PECVD. 77
4.3 Influence of gas flow ratio on refractive index and deposition rate of SiO_x. . 78
4.4 Influence of deposition time on the deposition rate. 79

4.5 Percentage influence of each deposition parameter on the film properties. . 83
4.6 Desirability values assigned for thickness, deposition rate and refractive index. 85
4.7 Influence of SiH_4 and chamber pressure on PECVD. 85
4.8 Influence of gas flow ratio γ on PECVD. 86
4.9 FTIR for multilayer samples. 88
4.10 Photoluminescence of multilayer samples for different annealing conditions. 89
4.11 Comparison of photoluminescence intensities for different annealing times. 90
4.12 Cross- section TEM micrographs of multilayer samples annealed at different temperatures. 91
4.13 Plan-view TEM micrographs of multilayer samples annealed at 1100°C for 60 minutes 91
4.14 Increasing photoluminescence intensity with increasing SiO_2 thickness in multilayers. 92
4.15 Comparison of photoluminescence in single and multiple layer structures. . 93
4.16 Increase of photoluminescence intensity with increasing bilayers stacks. . . 94

5.1 Bandgap engineering of silicon quantum dots observed by photoluminescence. 98
5.2 Experimental and theoretical values of photoluminescence peak for different dot diameters. 99
5.3 p-i-n type devices with Al or polysilicon (boron doped) electrodes. 100
5.4 n-i-p devices with ITO thickness 100 nm and 250 nm, allowing passage of more than 80% of light through the substrate. 101
5.5 Light transmission in ITO versus wavelength. 102
5.6 Current versus voltage characteristics for different electrode materials - (a) Al, (b) polycrystalline Si, (c) ITO - 100 nm and (d) ITO 250 nm. 103
5.7 I-V characteristics comparison of thick single layers and multiple bilayers. . 104
5.8 Current vs voltage characteristics showing hysteresis. 105
5.9 Comparison of low temperature electrical conduction characteristics of multilayers and thick single layers. 107
5.10 Poole-Frenkel conduction in multilayers and single layers at high electric fields. 108

5.11 Schematic of expected and actual quantum dot configuration formed after annealing of the SRO-SiO_2 bilayers. 110
5.12 Arrhenius plots for different samples fabricated in this thesis. 111
5.13 Schematic showing the distribution of inter-dot distances in a SiO_2 matrix. 112
5.14 Spectral response of multilayer and thick single layer films 113

A.1 E-k diagrams depicting quantum dot formation. 137

List of Tables

1.1 Confirmed terrestrial cell efficiency records under the global AM 1.5 spectrum. 30

2.1 Deposition conditions used for fabrication of one-step deposited single layers. 42
2.2 Samples used for characterizations of one-step deposited single layers. . . . 43
2.3 FTIR peak frequencies for Q75 post-annealing 48
2.4 Comparison of fit parameters obtained using Tauc-Lorentz dispersion model and the Bruggeman's Effective Medium Approximation 53
2.5 Comparison of calculated diameters and expected photoluminescence peaks for different samples using TEM, GIXRD and ellipsometry. 61

4.1 Factors used in the D-optimal Design of Experiments for PECVD of SiO_x. 81
4.2 Samples used for characterizations of multi-layer structures. 87

5.1 Multilayer samples (with 10 bilayers) and a thick single layer sample used for electrical characterizations with different electrode materials. 102

B.1 Experimental runs used in Design of Experiments. 139

Abbreviations and Acronyms

μm	Micrometres
A	Amperes
Al	Aluminium
AM	Air Mass
BEMA	Bruggeman's Effective Medium Approximation
cm	Centimetres
CMOS	Complementary Metal Oxide Semiconductor
Cu	Copper
CVD	Chemical Vapour Deposition
D	Desirability
d	Diameter of the quantum dot
DOE	Design of Experiments
EFTEM	Energy-Filtered Transmission Electron Microscopy
FTIR	Fourier Transform Infrared Spectroscopy
FWHM	Full Width Half Maximum
GIXRD	Grazing-Incidence X-Ray Diffraction
ITO	Indium Tin Oxide
LPCVD	Low Pressure Chemical Vapour Deposition

MEG	Multiple Exciton Generation
mil	Thousandth of an inch
MIS	Metal-Insulator-Semiconductor
mm	Millimetres
MOS	Metal-Oxide-Semiconductor
MSE	Mean Squared Error
nc	Nanocrystal
nm	Nanometres
NNH	Nearest Neighbour Hopping
PECVD	Plasma Enhanced Chemical Vapour Deposition
poly	Polycrystalline
PV	Photovoltaic
QD	Quantum Dot
QE	Quantum Efficiency
RTA	Rapid Thermal Annealing
sccm	Standard Cubic Centimetres per Minute
SCLC	Space Charge Limited Current
SE	Spectroscopic Ellipsometry
Si	Silicon
SRO	Silicon Rich Oxide
T	Temperature
TCO	Transparent Conducting Oxide
TEM	Transmission Electron Microscopy

TL	Tauc-Lorentz Dispersion Model
V	Volts
VRH	Variable Range Hopping
W	Watts
XRD	X-Ray Diffraction

"The most beautiful experience we can have is the mysterious - the fundamental emotion which stands at the cradle of true art and true science."

— Albert Einstein

Introduction

Silicon based technology is present in nearly every electronic product in the world today. Current microelectronics and photovoltaic industries are both dominated by silicon, and thus have silicon compatible processing technologies. Technological developments in either of these domains have given a technology push to the other.

Bulk crystalline silicon is a poor emitter due to its indirect bandgap. The discovery of light emission in nanostructured silicon in the 1990s opened up new avenues of research in nano-silicon based microelectronics, photovoltaics and even photonics. One such pathway is the application of silicon quantum dots in advanced photovoltaic devices. Current single p-n junction based Si solar cells, that dominate the solar cell market, are limited by the theoretical efficiency maximum of 29%. The necessity for decreasing carbon emissions, reaching grid parity for photovoltaic devices and increasing solar cell efficiencies are important issues that face the near future.

Silicon quantum dots allow the bandgap engineering of Si and demonstrate improved emission, which are both promising properties for photovoltaic applications. The bandgap engineering of silicon can potentially lead to all-Si based tandem solar cells with appropriate bandgaps, which can reduce lattice thermalisation losses and overcome the single junction efficiency limit.

In this work, the scientific and technical expertise on silicon quantum dots for microelectronics applications, and silicon compatible technology at *Leti* (Laboratoire d'Electronique des Technologies de l'Information) was used to transfer the microelectronics technology to photovoltaics, with expertise at *Liten/Ines* (Le Laboratoire d'Innovation

pour les Technologies des Energies Nouvelles et les Nanomatériaux / L'Institut National de l'Energie Solaire). Both of these laboratories are part of the *CEA* (Commissariat à l'Energie Atomique et aux Energies Alternatives).

Such an approach, based on microelectronics, can allow rapid integration of these materials into future commercial technologies. The Si quantum dots are fabricated in a dielectric matrix like SiO_2. The challenges involved in integrating these nanostructures in devices include precise dot size/bandgap control, optimizing electrical conductivity and improving optical response, while considering the limitations of large scale fabrication. This thesis deals with these issues in the following chapters:

The **First Chapter** establishes the parallels in the silicon based microelectronics and photovoltaics industry with the state-of-the-art in the latter. The role of quantum confined silicon nanocrystals in improving photovoltaic efficiencies is established.
The **Second Chapter** describes the fabrication of thick single layer films (more than 30 nm) of SiO_2 with embedded Si quantum dots, using plasma enhanced chemical vapour deposition of silicon rich oxide followed by high temperature annealing. Characterization techniques for describing the film properties and determining dot size/quantum confinement in Si quantum dots are established for the thick single layers.
The **Third Chapter** discusses the film thickness dependent ordered formation of silicon quantum dots which is a result of the Si diffusion in the thick layers. Its consequences on the electrical conductivity in the films and photocarrier generation are discussed.
The **Fourth Chapter** deals with the fabrication of ultra-thin multiple bilayer structures (less than 3 nm) with full control on the deposition process to control film thickness and silicon enrichment. Size controlled quantum dots with controlled inter-dot distances will thus be fabricated.
In the **Fifth Chapter**, devices with different quantum dot layers are fabricated to compare the optical and electrical properties in single layers and multiple bilayer films. The conduction mechanisms and spectral response for different device structures are evaluated, and their utility for photovoltaic devices is discussed.

This work was carried out in collaboration with between the laboratories *LC2E* (Laboratoire Composants Electroniques pour l'Energie) at *CEA/LETI*, *LCP* (Laboratoire des Composants Photovoltaïques) at *CEA/LITEN/INES* and *LMGP* (Laboratoire des Matériaux et du Génie Physique) at the *INPG*. This research was partially funded by the *DGA* (La Délégation Générale pour l'Armement).

Chapter 1

An Introduction to Si Quantum Dots

1.1 Silicon Technology - More than Microelectronics

Silicon Technology

Silicon based technology is present in nearly every electronic product in the world around us and has contributed tremendously to our changing lifestyles. Advances in high precision technologies on silicon wafer substrates for integrated circuits (ICs) and electronic devices have paved the way for enormous progress in improving performance and reducing costs of the semiconductor industry. Over the past five decades, the growth of the semiconductor industry has followed Moore's law,[1] which roughly states that the number of components that can be placed inexpensively on an IC doubles approximately every two years. Keeping up with these targets have consequently boosted research efforts concerning silicon, and this active research in semiconductor technology has also given a push to other industries, including photonics and photovoltaics.

Silicon Beyond Microelectronics

Complementary Metal Oxide Semiconductor (CMOS) represents the dominant semiconductor technology used in the fabrication of memories, microprocessors and other electronic integrated circuits. Silicon, a CMOS compatible material, has dominated the semiconductor industry primarily because of its abundance in the earth's crust and low toxicity. Silicon's good thermal conductivity and mechanical strength aid in relatively simpler processing techniques and its electrical conduction can be further enhanced by

doping with other elements. However, bulk crystalline silicon has an indirect bandgap of 1.12 eV at ambient temperature, which makes it a poor light emitter.

The discovery of light emission from porous silicon in the early 1990s by Canham and Cullis,[2,3] led to new avenues of research involving enhancement of optical properties of silicon, while sticking to CMOS compatible materials for rapid integration and scaling up. Silicon photonics, first mentioned by Soref,[4] have thereafter become increasingly important to keep up with "more-Moore" (higher performances by increasing integration parallelism) and "more-than-Moore" (new computation principles and diversified technologies) evolution in the electronics industry.[5]

The semiconductor industry therefore has significant technological expertise on the different forms of silicon, from bulk to porous nanostructured materials and quantum dots, which can all be extended beyond IC fabrication. There has been a vast migration of resources between the three domains of microelectronics, photonics and photovoltaics as they run in parallel, yet overlap in terms of applications. Research and development advancements in either one of these technologies has consequently led to progress in the other two.[6,7] As an illustration of this trend, system integration and product development for CMOS photonic devices have become an important part of research efforts in companies like Luxtera, Lightwire, Intel and IBM.[8,9] Furthermore, in the past five years giant chip manufacturers including Intel, IBM and HP have also started venturing into commercial photovoltaic manufacturing.[10] This has been supported thanks to a strong backing from their fine-tuned manufacturing processes and technology equipment along with already existing R&D centres.

Such an interconnected mesh of technological expertise has opened broad pathways for novel research opportunities in silicon, going well beyond silicon microelectronics. *Quantum dots* are an important part of this trend and will be discussed during this research work.

1.2 Silicon Nanotechnology - Beyond Bulk Silicon

Although bulk silicon is the most commonly used material in the photovoltaic industry and is also a strong candidate for photonics applications, its indirect bandgap makes it an inefficient light absorber and a very poor emitter. The low absorption coefficient (α), is due to the participation of a phonon during absorption or emission to conserve both energy and momentum. This *three-particle interaction* (electron, hole and phonon) makes the process less probable (See Figure 1.1). Since phonon mediated light emission depends on the inverse of the photoelectric effect, the absorption properties depend strongly on the emission. Therefore, a good emitter is essentially a better absorber. In silicon, a small value of α increases the required penetration depth for photons. Silicon solar cells thus have a thickness of more than 100 micrometers and need surface texturization treatments and anti-reflection coatings to actually absorb all photons and minimize problems of front surface transmission. A possible pathway to overcome this drawback in bulk indirect bandgap silicon is to use *"silicon nanocrystals"* or *"silicon quantum dots"*.

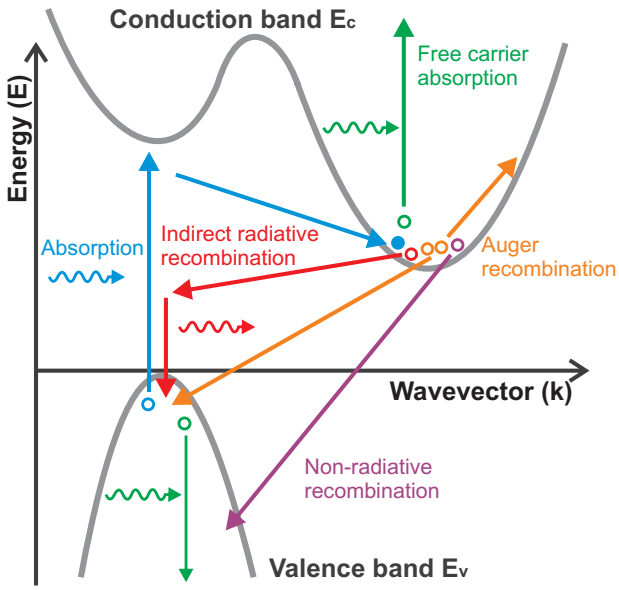

Figure 1.1: Schematic energy band diagram of silicon showing electron excitation and absorption in silicon (adapted from Yuan et al[5]). Blue arrows indicate indirect absorption. Red arrows indicate phonon assisted indirect radiative recombination. Purple arrows show non-radiative recombination and orange arrows show Auger recombination. Green arrows indicate free-carrier absorption.

1.2.1 Quantum Confinement in Silicon

In a bulk crystal, the optical and electronic properties of the material do not depend on the size. However, as we go into the quantum mechanics regime with sizes in the order of nanometres, there is a completely different story. The material properties can then be engineered to our advantage, as will be discussed in this section. In quantum confined materials, *excitons* (electron-hole pairs) can be confined in 1D (quantum well), in 2D (quantum wire) or in 3D (quantum dots), as shown in Figure 1.2.

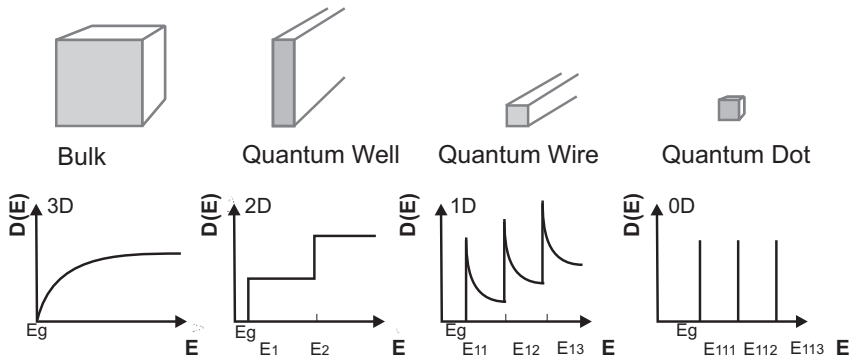

Figure 1.2: Idealized density of states for one band of a semiconductor structure of 3, 2, 1 and 0 dimensions. In the 3D case, the energy levels are continuous, while in the 0D or molecular limit the levels are discrete.[11]

A simplified approach to understanding confined electrons can be made by using the famous *particle-in-a-box* problem, described in Appendix A for silicon dots embedded in an insulating matrix. For strong quantum confinement, the size of the quantum dot is smaller than its *Bohr exciton radius*, which is defined as the minimum natural separation between electrons in conduction band and their corresponding holes in the valence band. For weak confinement, the size is 2-4 times greater than the Bohr exciton radius. For silicon, this radius is $\sim$4.9 nm,[12] meaning that quantum dots of around 5 nm are required for strong confinement. The quantum confinement effect leads to an increase in the bandgap, as explained in Appendix A.

Brus[13,14] came up with a simple generalised analytic model describing the size-effective

bandgap (E_{QD}) for the lowest energy states for 3D confinement:

$$E_{QD} = E_{bulk} - \frac{3.6q_e^2}{\epsilon d} + \frac{2\hbar^2\pi^2}{d^2\mu} + smaller\ terms \tag{1.1}$$

where E_{bulk} is the bulk bandgap, ϵ is the silicon dielectric constant taken to be 11.7, μ is the reduced mass of the electron-hole pair, and d is the nanocrystal diameter.

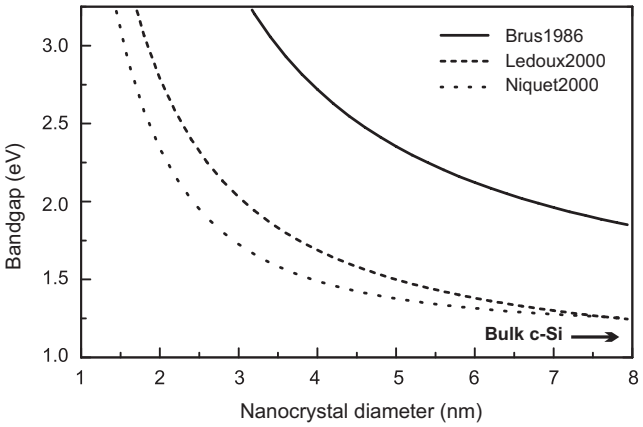

Figure 1.3: Comparison of theoretical calculations for the evolution in band gap with quantum dot diameter.[13,15,16]

An improved and corrected phenomenological version pertinent to the case of silicon quantum dots, and based on photoluminescence measurements, was published by Ledoux et al.[15] Additionally, theoretical calculations (tight binding parametrization) were published by Niquet et al.[16] The results of these models have been compared in Figure 1.3. In general, trends in experimental data for silicon quantum dots have corresponded well with these theoretical calculations,[15,17–23] even though the values obtained are consistently lower than theoretical predictions of confined energy levels.[24–26] These reported results thus confirm that the silicon bandgap can indeed be engineered depending on the size or diameter of the quantum dots.

Solid state silicon quantum dots are usually fabricated in a dielectric insulating matrix (SiO_2, Si_3N_4, SiC) in a technique first established by Tsybeskov et al.[27] The process involves deposition of non-stoichiometric compounds followed by high temperature annealing for silicon quantum dot segregation and precipitation in thick single

or ultra-thin multiple bilayer structures. In the case of the SiO_2 matrix, high oxide energy barriers do lead to strong confinement in the Si quantum dots. However for inter-dot tunnelling conduction through wide bandgap barriers, the wavefunction of an electron confined to a spherical dot should penetrate into the surrounding material, as it decreases exponentially into the barrier. The tunnelling probability through these insulating barriers can be approximated through the transmission coefficient T_e for quantum tunnelling. This is given by[24]

$$T_e \simeq 16\, exp\left[-l\sqrt{\frac{8m^{*2}\Delta E}{\hbar^2}}\right] \tag{1.2}$$

where l is the barrier width or the spacing between the dots, ΔE is the energy difference between the conduction band edge of the matrix and the confined energy level of the quantum dots and m^* is the effective mass of the electron within the barrier. Because of the large ΔE, quantum dots in a SiO_2 matrix should be separated by no more than 1 to 2 nm (See Figure 1.4). This value could go up to 4 nm for a silicon carbide matrix. However, confinement in the dots is then lower due to the non-infinite barrier and lowering of confined energy. The segregation and precipitation effect for Si in SiC also decreases, making crystalline dot formation in amorphous SiC more difficult.[24]

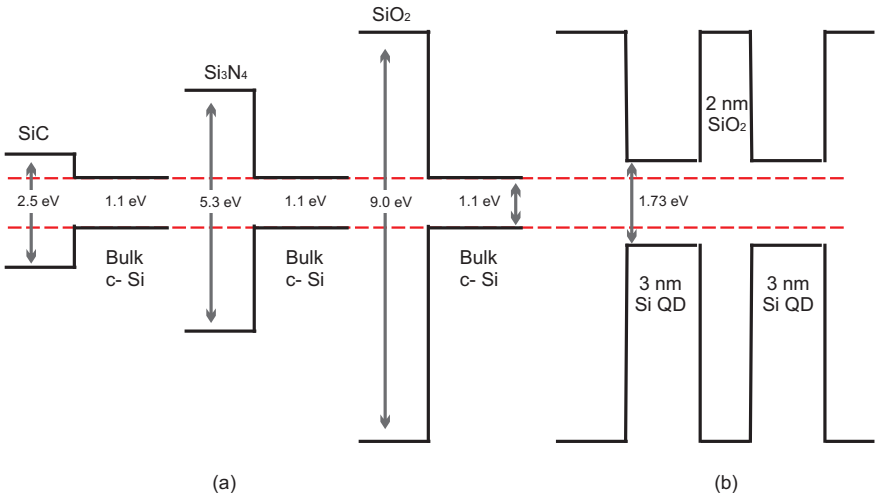

Figure 1.4: (a) Bulk band alignments between crystalline silicon and SiO_2, Si_3N_4 and SiC. (b) The band gap increases for quantum confined silicon dots of 3 nm diameter to 1.73 eV.[16] To ensure tunnelling between silicon dots embedded in SiO_2, the distance between dots should be less than 2 nm.

For nanocrystals in SiO_2, smaller dots (less than 3 nm diameter) are highly surface sensitive due to their large surface-to-volume ratio. Silicon oxygen double bonds are present on the nanocrystal surface and can capture and localize the excitons,[25,28,29] although they can be passivated by hydrogen.

Nevertheless, quantum confined silicon quantum dots show improved emission and absorption compared to bulk crystalline silicon. Experimentally, this improvement cannot be attributed to an enhancement of the absorption coefficient. Rather, improved emission occurs due to decrease in non-radiative recombinations which go down as compared to bulk silicon as small mid-gap defects and impurities grow out of the dots and into the interface.[30] Furthermore, the excitons cannot diffuse for large distances, reducing the probability of finding non-radiative recombination centres.[5] The radiative recombination rate is improved as the electron-hole wavefunctions are now squeezed in real space in the potential well when the size of the dot gets smaller than the Bohr exciton radius.[31] Therefore, in spite of the indirect band gap, zero-phonon transitions may occur, giving quantum confined silicon dots a *"quasi-direct bandgap"*.[32–34] For these reasons, silicon quantum dots may possess a high emission efficiency after passivation of surface defects, as will be discussed later in this work.

1.2.2 Applications of Silicon Nanocrystals

Quantum mechanical effects on silicon have indeed led to several applications involving silicon quantum dots, as illustrated in Figure 1.5. However, in spite of the advantages

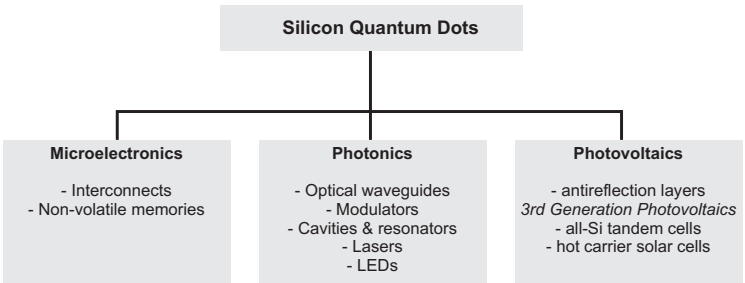

Figure 1.5: Si quantum dots have diverse applications in microelectronics, photonics and photovoltaics.

of silicon nanostructures over bulk silicon, it is still a poor optical material compared to III-V semiconductors. Research and development has nevertheless continued due to advantages of silicon including lower costs and full CMOS compatibility. More than 5000 publications (as of April 2011) mention silicon nanocrystals or silicon quantum dots. As discussed earlier, the three main domains of applications of silicon quantum dots of interest in the scope of this thesis are photonics, microelectronics (microphotonics) and photovoltaics, each of which have been described below.

- **Photonics** - Improvement in the light emission properties of nanostructured silicon, as compared to bulk Si, has led to research and applications in light emitters, lasers and photodetectors[35–38] where III-V materials were traditionally used. Active optical waveguide and modulator structures based on quantum dots have been reported[39,40] along with optical microcavities and resonators for lasing applications.[41–43]

- **Microelectronics and Microphotonics** - As the number of transistors in an IC increase to keep up with Moore's law, the number of interconnecting wires also increase. These interconnects are currently made of copper. A future "interconnect bottleneck" can be avoided using silicon photonics. This solution is based on replacing copper interconnections by a series of lasers, modulators, optical waveguides and photodiodes which can also decrease delay times and power dissipation.[30,44–46] Multidimensional confinement of free carriers in silicon quantum dots in SiO_2, along with their robustness to oxide defects, has led to applications in optical and non-volatile memories.[47–51]

- **Photovoltaics** - Bandgap engineering in silicon quantum dots along with improved optical properties, has led to applications in photovoltaics.[24,52–55] Recent interest in solar cell applications is evident as out of a total of around 200 papers on the subject published since 2004, more than 100 of have been published since 2008.

This thesis will focus on these photovoltaic applications which will be discussed in the next sections.

1.3 Silicon in Solar Cells

The photovoltaic (PV) industry has been growing at the annual rate of 40% over the last decade,[56] and is mostly based on mono and multi crystalline bulk silicon (c-Si). Further rapid growth is expected thanks to extensive efforts for increasing renewable energy use and decreasing carbon emissions for coping with climate change. National and international long-term initiatives are pushing the solar energy industry to increase efficiency and decrease costs.[57] The International Energy Agency's PV roadmap estimates that by 2050, PV will provide around 11% of global electricity production and avoid 2.3 gigatonnes of CO_2 emissions per year. In addition, it will achieve competitiveness with electricity grid retail prices by 2020.[58]

Historically, c-Si has been the most popular solar cell material, deriving its technology know-how from the microelectronics industry. Silicon based technologies currently occupy 80% of the market share, mostly due to the nearly ideal bandgap of 1.1 eV. By 2020 traditional silicon based solar cells are still expected to dominate even as other technologies emerge (Figure 1.6).[56]

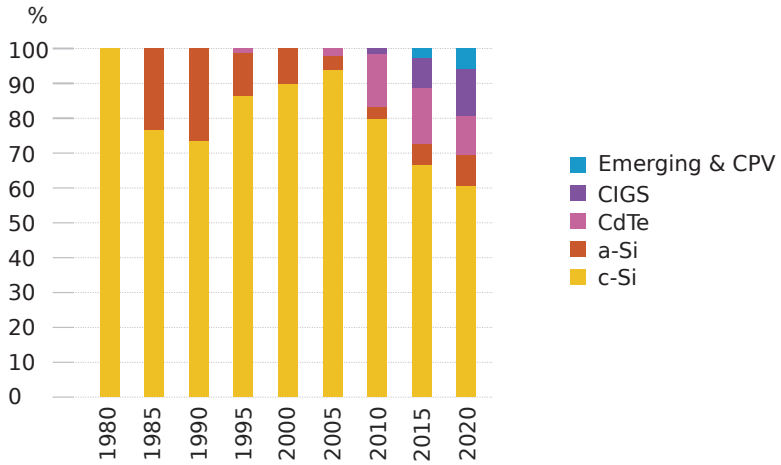

Figure 1.6: Historical evolution of technology market share and future trends. Silicon is projected to be the dominant material till 2020 even as other technologies emerge. Source: EPIA[56]

1.3.1 Photovoltaic Technologies

Currently used photovoltaic technologies can be classified into three broad categories based on the photovoltaic materials and fabrication techniques used. These have been briefly described below:

- *First generation* photovoltaics consist of basic *crystalline silicon* (c-Si) including single crystalline Si (sc-Si), multicrystalline (mc-Si) and are p-n junction devices.
- *Second generation* solar cells include *thin films* technologies of amorphous silicon (a-Si) and micromorph-Si (a-Si/μ-Si), CdTe, CIGS and $CuInSe_2$ or $CuInS_2$.
- *Third generation* photovoltaics include new and emerging technologies. Concentrator photovoltaics (CPV) are already in the market while advanced thin films, tandems and organic cells are set to be commercialized. Other high efficiency photovoltaics aim to use advanced conversion concepts and novel innovative materials and are mostly at the research stage. Several of these new concepts involve quantum confined materials and will be discussed later in this chapter.

As of January 2011, the highest independently confirmed efficiencies for some solar cells have been listed in Table 1.1.[59] In addition, III-V triple junction cells have already demonstrated 35.8% efficiency under one sun.[60]

First Generation		**Second Generation**		**Third Generation**	
c-Si	25.0 ± 0.5	CIGS	19.6 ± 0.6	Dye sensitized	10.4 ± 0.3
mc-Si	20.4 ± 0.5	CdTe	16.7 ± 0.5	Organic polymer	8.3 ± 0.3
		a-Si	10.1 ± 0.3	*GaInP/GaAs/Ge**	32.0 ± 1.5
				*a-Si/μc-Si**	11.7 ± 0.4
				*Organic**	8.3 ± 0.3

Table 1.1: Confirmed terrestrial cell efficiency records under the global AM 1.5 spectrum 1000W/m^2 at 25°C.[59] *Italic data represents multi-junction PV devices.

The IEA's Photovoltaic Roadmap[58] lays tremendous stress on the need for increasing R&D efforts to reduce costs and ensure PV readiness for scaling up and rapid deployment of new innovative concepts. One of the important targets of research efforts in this domain

is to achieve *grid parity*. Grid parity means that the cost of generating a unit of energy with photovoltaic power becomes competitive with existing grid electricity prices.

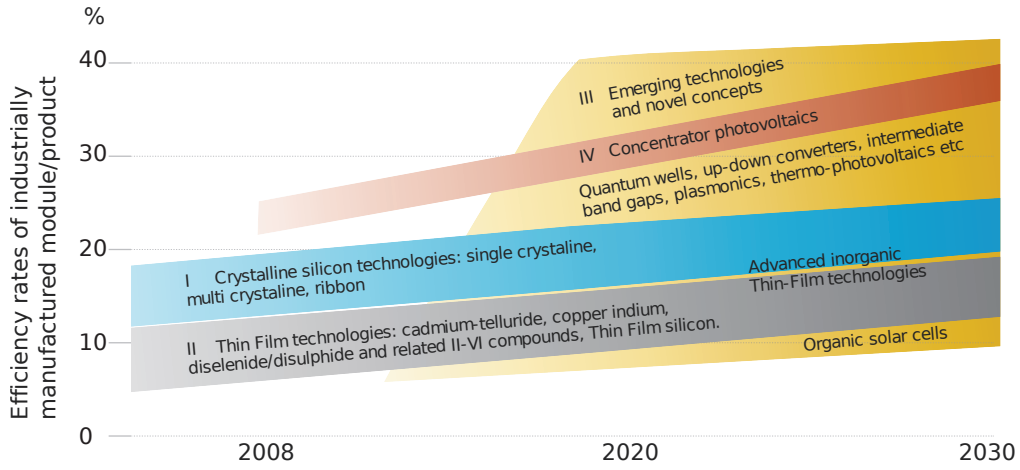

Figure 1.7: Photovoltaic technology status and prospects till 2030. Contribution from emerging technologies and novel concepts from third generation photovoltaics is projected to increase industrially manufactured cell efficiencies in the upcoming decades. Source: IEA - Photovoltaic Technology Roadmap[58]

Technological innovation is therefore essential for cost reduction in a photovoltaic system, and some of the ways to do this are decreasing material quantity used and improving cell efficiencies. In addition, continuous research efforts are important for constant industrial growth, keeping in mind compatibility with existing technologies. To illustrate the importance of these future technologies, PV technology status and prospects till 2030 have been illustrated in Figure 1.7. We can clearly see that third generation technologies are projected to provide high efficiency photovoltaic cells in the coming decades.

1.4 Si Quantum Dots in Third Generation Photovoltaics

1.4.1 Efficiency Losses in a Solar Cell

The solar spectrum consists of light between wavelengths of approximately 100 to 3000 nm. This range includes infrared radiation, visible light and ultraviolet light. More than 90% of the solar radiation reaching the earth's surface is visible light and near-infrared radiation, with a wavelength range of around 350 to 1500 nm (Figure 1.8).

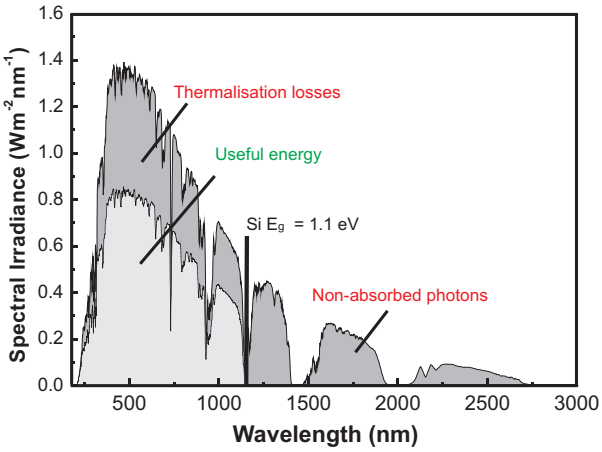

Figure 1.8: Global Total Spectral Irradiance ($W/m^2/nm$) on a 37° sun facing tilted surface with Air Mass (AM) 1.5. Regions of thermalisation losses and non-absorbed photons are shown.[61]

As illustrated in Figure 1.9, only those photons are absorbed by a solar cell whose energies are greater than or equal to the band gap of the semiconductor material (E_g of silicon at 300 K = 1.12 eV), while lower energy photons are lost. Furthermore, the excess kinetic energy of the absorbed photons creates hot carriers which are basically electrons and holes with more energy than the band gap. As these carriers relax to their band edges, the excess energy is lost as it is converted to heat via lattice vibrations.

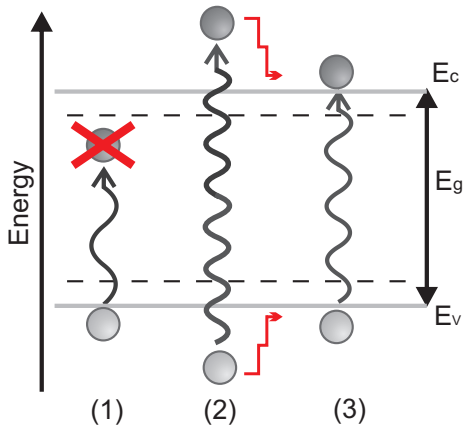

Figure 1.9: Schematic of loss mechanisms in solar cells. Photons with energy lower than the semiconductor bandgap are not absorbed (1), while those with excess energy (2) lose it as heat in the form of lattice vibrations. In (3) the incoming absorbed photon has the same energy as the bandgap of the material.

This is one of the major factors affecting the efficiency of bulk silicon based single band gap solar cells and is commonly known as the *"Shockley-Queisser"* limit of 31%,[62] valid for a general single gap material. This limit exists even though the thermodynamic efficiency of solar energy conversion is 86.8% under maximum concentration (assuming the sun to be a black body at 6000 K).[63]

1.4.2 Quantum Dots in Photovoltaics

Quantum dots incorporated in photovoltaics have the possibility of increasing solar cell efficiencies well beyond the Shockley-Queisser limit.[63,64] This efficiency improvement can be achieved through novel concepts based on increasing either photocurrents or photovoltages. Quantum dots are a good material candidate as quantum confinement leads to improved absorption, along with a tunable bandgap. Group II-VI and IV-VI (CdSe, PbSe, CdS, PbS), Group III-V (GaInAs, GaAs) and group IV (Si, Ge) dots have been used for their enhanced properties. The theoretical efficiency limits of such concepts have been illustrated in Figure 1.10.[65]

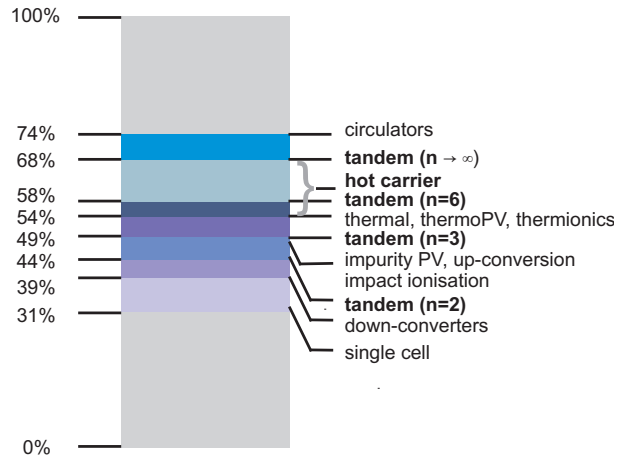

Figure 1.10: Efficiency limits for different photovoltaic concepts.[65] Silicon quantum dots can potentially be used in those indicated in bold.

Tandem solar cells improve absorption by using multiple bandgaps.[66] Hot carrier solar cells extract the carrier before it cools down.[65,67–70] Multiple exciton generation involves generation of more than one exciton per photon through impact ionization.[71–73] Intermediate bandgap solar cells may allow sub-bandgap energies to be absorbed.[74,75]

Quantum dots can even be used in low efficiency - low cost hybrid solar cells with organic materials.[76,77] Most of these applications are still in the research phase for third generation photovoltaics. So far, tandem cells are the only commercially available high-efficiency concepts. 32% efficiency has been achieved for GaInP/GaAs/Ge devices.[59]

1.4.3 Si Quantum Dot Photovoltaics

Silicon quantum dots can be incorporated in solar cells to improve cell efficiencies and test novel conversion concepts. Several research efforts have been dedicated to optimising silicon nanocrystal properties for solar cell applications. Kim[78] recently published results for silicon quantum dots with absorption enhanced 14 times in blue and green light regions as compared to bulk silicon. Other works include studies on quantum dot doping[54,79,80] deposition conditions and optical properties.[81,82] Silicon quantum wells have also been examined for third generation applications.[55,83–85] Si nanocrystals have also already been integrated into photovoltaic devices, as will be discussed below.

p-n Devices

Heterojunction devices with p-n or n-p junctions have been used with doped silicon quantum dots on a bulk c-Si substrate. Such devices have demonstrated efficiencies of 10.6% for phosphorous-doped dots[53] (Figure 1.11) and 9.5% for boron-doped dots.[86] While these values are not comparable to standard silicon solar cell efficiencies, they are a positive step towards device integration, as they demonstrate electrical conduction via quantum dots through a wide bandgap matrix. Although most absorption is expected to be in the silicon substrate, p-i-n devices fabricated on quartz have shown promising results.[87]

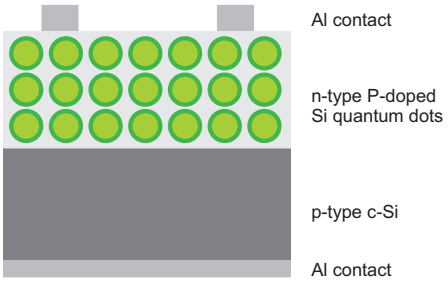

Figure 1.11: Schematic of the device used by Cho et al[53] for 10.6% cell efficiencies.

Tandem solar cells

Tandem cells involve cascading multiple p-n junctions with bandgaps matched to the incident light spectrum. Lattice thermalisation losses occur for incident energies higher than the bandgap of silicon. In a three-cell tandem as shown in Figure 1.12, highest energy photons are absorbed in the highest bandgaps, while lower energies are absorbed in the middle or bottom cell, reducing thermalisation losses. This can lead to theoretical radiative efficiencies of 42.5% for two-cell tandems and 47.5% for 3-cell stacks. Under AM 1.5 illumination, for a bulk Si bottom-cell (1.1 eV) the optimal top-cell bandgap for achieving maximum conversion efficiencies is $\sim$ 1.7 eV for a 2-cell tandem. For a 3-cell tandem, the bandgaps are $\sim$ 1.5 eV and $\sim$ 2.0 eV for the middle and top cells respectively.[88] Additionally, improved optical properties of silicon quantum dots contribute to less material use, requiring thinner films for efficient light absorption.

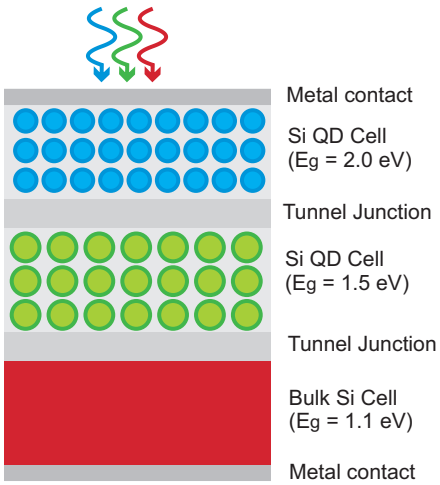

Figure 1.12: Schematic of an all-Si based tandem solar cell. Varying bandgaps can be achieved by varying silicon quantum dot size. For a 3-tandem cell as shown here, the theoretical efficiency limit is 47.5%.

Hot carrier solar cells

With theoretical efficiencies even higher than a six-cell tandem stack, research efforts for fabricating silicon quantum dot based hot carrier solar cells have gained popularity.[65] Silicon nanocrystals can be used as selective energy contacts in a hot carrier solar cell. The absorber material comprises of larger quantum dots and is like a p-i-n (or n-i-p) device

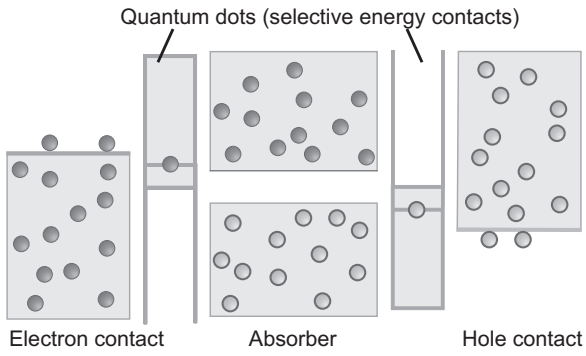

Figure 1.13: Schematic of a hot carrier solar cell with an absorber and selective energy contacts that can be made of quantum dots.[65]

with silicon quantum dots as the intrinsic array. The silicon dots form a superlattice that slows down photo-excited carrier cooling and allows transport of hot carriers. The absorber is connected to the electron or hole contact metal with a selective energy contact. The selective energy contact is made of smaller quantum dots with high resonant state energy for resonant tunnelling.[65,89–92]

Other conversion concepts

- *Quantum cutting* can be achieved by doping silicon quantum dots with Er^{3+}.[93] In the quantum cutting process, energy is transmitted outside the photo-excited system, in this case to Er^{3+} ions. High energy photons can be split into two or three photons of lower energy, increasing the efficiency of a device.

- *Hybrid solar cells* of silicon quantum dots and P3HT have been reported with 1.15% efficiency conversion.[94] Hybrid solar cells combine the attractive properties of strong visible absorption in conjugated polymers with size tunable absorption spectra in quantum dots.

- *Metal-Insulator-Semiconductor* (MIS) type devices have been reported with a super-linear photovoltaic effect.[95] This is due to secondary carrier generation from photons in the the sub-bandgap state, which have been created due to traps at the interface.

- *Multiple exciton generation* (MEG) has been reported in colloidal silicon quantum dots.[96] For dots of 1.2 eV bandgap, 2.6±0.2 excitons per photon have been observed

to be absorbed at 3.4 times the bandgap energy.

Anti-reflection coatings

Silicon quantum dots can also be used for down-shifting in an anti-reflection coating for improving absorptance at particular wavelengths.[97] While this is not really a third generation high efficiency concept for overcoming the Shockley-Queisser limit, yet 0.4% efficiency improvement has been reported so far.[98] Improved luminescence from the nanocrystals can possibly further increase this efficiency value.[99]

1.5 Aim of this Thesis

Silicon nanotechnology concepts have proved to be promising for photovoltaic applications, especially considering their processing compatibility with both CMOS technology and the photovoltaic industry. Recent interest in silicon nanostrutures for solar energy conversion has intensified as high efficiency third generation photovoltaic concepts begin to consider quantum confined silicon as a promising material. Silicon quantum dots are embedded in an insulating matrix like SiO_2 and demonstrate a bandgap tunable with dot size, improved absorption and photoluminescence.

However, as we move from bulk silicon to quantum confined silicon quantum dots, several challenges need to be addressed before integrating these dots into high efficiency devices. These challenges include:

- improving film material quality and minimizing defects and surface states arising due to the nanometric dimensions of the dots.
- controlling the uniformity of the quantum dot size distribution, which is essential for optimum bandgap control.
- optimizing electrical properties like charge carrier mobility, efficient electrical injection and charge separation as the nanocrystals are embedded in an insulating matrix.

Most importantly, there is a need for futuristic outlook and constant innovation for new device architectures.

The motivation behind this research work is to use existing microelectronics and CMOS technologies for solar cells of the future. The bulk silicon processing technology, developed in the clean room at *Leti*, for fabrication and characterization of commercial-scale microelectronic devices will be utilised for progress in advanced photovoltaic cells which are still at the research phase. Silicon nanotechnology and silicon quantum dots have a wide range of applications. Focussing on solar cells, the aim of this thesis is to understand and improve the material properties while ensuring electrical conduction and optical enhancement for integration of silicon quantum dots into photovoltaic devices. These Third Generation photovoltaic devices based on silicon quantum dots may provide high efficiency devices, contributing to a green and clean energy based future.

Chapter 2

Developing Single Layers of Si Quantum Dots

2.1 Introduction

In this chapter, we will discuss the fabrication and characterization of silicon nanocrystals embedded in a singly deposited silicon dioxide layer, using CMOS compatible technologies on 200 mm silicon wafer substrates. This will form the basis of the rest of the thesis as the analysis of these layers will be extended to more complex structures in the next chapters. We will compare the stoichiometric properties of the silicon rich oxide layers using ellipsometry and infrared spectroscopy, while properties that are more inherent to quantum dots like band gap and size will be analysed using x-ray diffraction, photoluminescence and transmission electron microscopy.

2.1.1 Fabrication Techniques

Silicon nanocrystals can be fabricated through a range of techniques that can be broadly categorized based on the physical principal involved. The most commonly used techniques are based on the property of the low mobility of silicon in its oxide,[100] which leads to silicon precipitation with other Si atoms that diffuse in the vicinity, thus forming a nanocrystal. The low diffusivity necessitates higher temperatures for silicon precipitation. Silicon rich oxide layers are deposited and then annealed, leading to a high-temperature equilibrium phase separation of Si and SiO_2 in sub-stoichiometric silicon dioxide layers. The low mobility of silicon in silicon dioxide consequently leads to formation of small nanometric sized silicon clusters. Techniques based on this principle

include chemical vapour deposition,[27,100] ion implantation,[101] aerosol synthesis,[102] magnetron sputtering,[27,52] ion sputtering[103] and reactive evaporation[104] of silicon oxides. Other fabrication techniques are laser ablation,[105] colloidal synthesis[106,107] and in-situ nucleation on the dielectric surface during chemical vapour deposition.[108] Top-down approaches like electrochemical etching of bulk crystalline Si in HF or machining can also be used. Considering its compatibility with semiconductor processing, including both photovoltaics and the high-quality demanding CMOS, we have chosen the fabrication approach of chemical vapour deposition followed by thermal annealing for silicon quantum dot formation.

The main requisites for a silicon quantum dot layer for photovoltaic applications are control over dot size, bandgap and inter-dot distance, each of which depend on the choice of the dielectric matrix.[34] The different options for the dielectric matrix are oxides (SiO_2), nitrides (Si_3N_4), carbides (SiC) and oxynitrides (SiO_xN_y). The advantage of embedding in an oxide matrix is that due to the larger gap of SiO_2, the energy barriers are higher leading to stronger confinement. On the other hand, charge transport properties are also likely to depend on the choice of the dielectric matrix and its barriers, as the tunnelling probability depends on the height of the barriers. Si_3N_4 and SiC are known to have lower barriers than SiO_2 (Chapter 1), permitting a larger inter-dot distance for tunnelling current. For a square potential well, the decay length L_d is given by[109]

$$L_d = \frac{0.1952\,nm}{\sqrt{\frac{m^*\Delta E}{m_0}}} \tag{2.1}$$

where m^* is the bulk effective mass in the respective band of the matrix, and ΔE is the energy difference (in eV) between this bulk band and the band formed by the quantum dot confined energy level.

For silicon dioxide matrix, the inter-dot distance should be no larger than 1-2 nm. Improved conduction can be observed in carbide and nitride matrices due to less constraint over the inter-dot distances. However, due to lower control over the confinement

and fabrication procedure, in this work we will focus on silicon quantum dots in SiO_2.

2.2 Synthesis of Si Quantum Dots in Silicon Dioxide

2.2.1 Plasma Enhanced Chemical Vapour Deposition

Deposition of silicon rich oxides by plasma enhanced chemical vapour deposition (PECVD) has been favoured over low pressure chemical vapour deposition (LPCVD) because of its lower thermal budget, and improved film density. While PECVD processes occur at 300°C - 500°C, LPCVD (500°C - 800°C) may already provoke a primary demixing of the silicon rich oxide even before the annealing step.

PECVD uses electrical energy from a continuous radio frequency (rf) source (AC) to generate a glow discharge between two electrodes. This plasma energy is then transferred into a gas mixture which is subsequently transformed into reactive radicals, ions, neutral atoms and molecules, and other highly excited species, as shown in Figure 2.1.

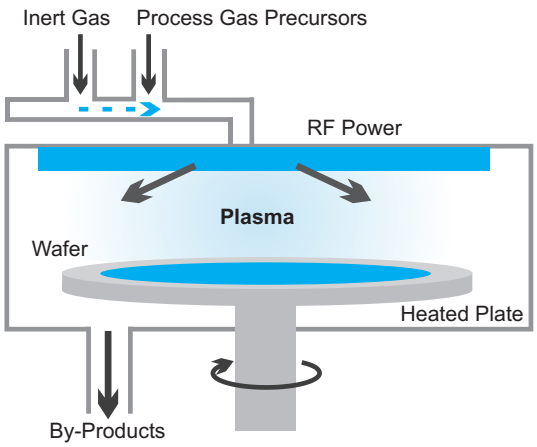

Figure 2.1: Schematic diagram of a plasma enhanced chemical vapour deposition (PECVD) reactor.

For SiO_2 deposition, the gas precursors involved are silane (SiH_4) and nitrous oxide (N_2O), along with the possibility of helium as the inert gas. The following reactions take place in the plasma[110]:

$$e^- + SiH_4 \longrightarrow SiH_2 + 2H + e^- \tag{2.2}$$

$$e^- + N_2O \longrightarrow N_2 + O + e^- \tag{2.3}$$

SiH_2 and O are free radicals which are both highly reactive. They react very quickly on the surface of the heated wafer, maintained at 300°C - 500°C, to form the desired SiO_2 film.

$$SiH_2 + O \longrightarrow SiO_2 + other\ reactive\ species \tag{2.4}$$

The overall reaction can be described by the following equation:

$$SiH_4 + 3N_2O \longrightarrow SiO_2 + 3N_2 + H_2 + H_2O + other\ reactive\ species \tag{2.5}$$

200 mm (8 inch) Czochralski Si wafers have been used throughout this thesis for fabricating uniform, thin films of silicon rich oxides. The depositions were carried out at 400°C or 480°C in the *Chamber A* of the *Applied Materials* reactor *Centura 5200E*. All of the terms silicon rich oxide (SRO), $SiO_{x<2}$, and sub-stoichiometric silicon dioxide can be used to denote the essential as-deposited layer for silicon quantum dot formation.

The excess silicon in SiO_x can be attained by optimizing the SiH_4 and N_2O gas flow ratio ($\gamma = N_2O/SiH_4$), which thereby controls $R = [O]/[Si]$ ratio.[111–113] This parameter γ, along with the chamber pressure, plasma power etc. can all affect the deposition rate and the excess silicon in the deposited oxide. The deposition conditions used in this chapter for the lot named *Q552P* have been listed in Table 2.1.

N_2O sccm*	SiH_4 sccm	Temperature °C	Pressure Torrs	Power W	Distance† mils‡	γ	Dep. rate nm/sec
2000	490	400	2.7	130	460	4.08	12.5

* Standard cubic centimetres per minute
† Inter-electrode distance
‡ 1 mils = thousandth of an inch

Table 2.1: Deposition conditions used for fabrication of one-step deposited single layers.

For these samples, p-type Si (1 0 0) wafers were used with resistivity of 5-10 Ωcm. Expected thickness values of the deposited silicon rich oxides on the fabricated samples

used in this chapter have been listed in Table 2.2.

Number	Sample Name	Expected Thickness *(nm)*
1	Q30	30
2	Q50	50
3	Q75	75

Table 2.2: Samples used for characterizations of one-step deposited single layers.

SRO depositions and Si quantum dot formation have already been the subject of detailed studies,[27,104,114] with the most importance being given to the ratio γ, as well as the annealing conditions for dot formation.[54,115–117] Annealing conditions can also affect both the size and the crystallinity of the dots, as it has been shown that higher annealing temperatures give smaller quantum dots.[114,118]

2.2.2 Thermal Annealing

The formation of silicon quantum dots occurs as the sub-stoichiometric silicon rich oxide undergoes a phase separation at high temperatures to form stable stoichiometric clusters of silicon and SiO_2, as illustrated in Figure 2.2.

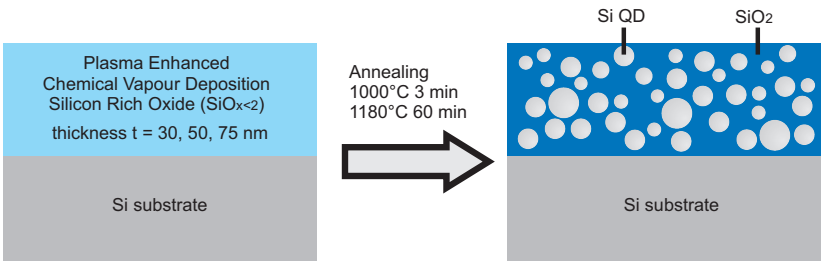

Figure 2.2: Silicon quantum dots are formed by the recrystallization of silicon rich oxides on high temperature annealing.

This high temperature annealing under nitrogen usually follows the deposition step. A minimum temperature of 500°C is required for the commencement of phase demixing and formation of amorphous clusters. For quasi-total phase separation and recrystallization,

a minimum temperature of 900°C is required.[117,119] The following reaction occurs and leads to the formation of silicon quantum dots:

$$SiO_x \longrightarrow \frac{x}{2}SiO_2 + (1 - \frac{x}{2})Si \tag{2.6}$$

In the *Reliance 850* furnace from *Eaton*, the temperature increases as resistances heat a SiC chamber, which then emits radiation. The heating module is at a constant temperature while the base is cooled. A temperature gradient (400°C to 1250°C) is thus established, and the substrate wafer can be annealed at the required temperature by moving it with the help of an elevator. The annealing therefore occurs with a fast ramp and cooling time. This is known as rapid thermal processing or rapid thermal annealing (RTA) as the substrates reach high temperatures at time scales of several seconds or less. This short ramp time makes RTA advantageous over conventional furnace processes. In this chapter, a two-step thermal treatment was used for the formation of Si quantum dots in SiO_2, similar to the technique used by Tsybeskov et al.[27] The first RTA at 1000°C (3 minutes) is expected to aid in the initial nucleation of silicon clusters which can be then further annealed in a regular furnace at 1180°C (60 minutes) for quantum dot growth.

In spherical quantum dots, the surface properties are extremely important because of the large surface to volume ratio. As the silicon dots are in an oxide matrix, a large number of defects may be present due to several factors. These include the spatial arrangement of silicon atoms in each nanocrystal and also the Si-SiO_2 interfaces which deteriorate the opto-electric properties of the film. An additional annealing step under forming gas (H_2/N_2) at 425°C for 30 minutes is known to passivate the Si-O dangling bonds and interface defects.[120,121] This additional annealing step can also take place after metallization of the device. The nature of these defects, and the consequences on photoluminescence and conduction will be detailed later in this chapter as we examine the structural properties of the films. It should be noted that the nitrogen content in the films was analysed using XPS (X-ray Photoelectron Spectroscopy) and found to be less than 4%, indicating good film quality.

2.3 Composition of the Silicon Rich Oxide Layers

Even though silicon quantum dots are formed only after the annealing step, the stoichiometry of the as-deposited films and especially the excess silicon content plays a vital role in the formation of the dots. The films have been studied using Spectroscopic Ellipsometry and Fourier Transform Infrared Spectroscopy for an insight into their stoichiometry.

2.3.1 Fourier Transform Infrared Spectroscopy

Principle Involved

Fourier Transform Infrared Spectroscopy (FTIR) is used in the domain of medium infra-red radiations (4000 to 400 cm^{-1}). FTIR involves the use of a Michelson interferometer with a fixed and a moveable mirror. The beamsplitter splits the incoherent infra-red source radiation into two coherent beams, one of which hits the fixed mirror and the other hits the moveable mirror. The movement of this mirror introduces a phase difference between the two waves leading to constructive or destructive interference on recombination. The beam is modulated into waves of different frequencies, thus translating the infrared spectrum into the form of an interferogram.

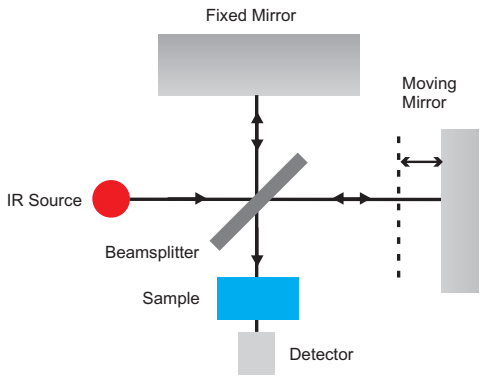

Figure 2.3: Schematic of a typical FTIR setup with a Michelson interferometer.

This modulated infra-red photon beam crosses through the sample, and some of it is absorbed because of molecular vibrations while the rest is transmitted. FTIR thus measures not only the spectral information of the source but also the transmittance char-

acteristics of the sample. Each chemical bond is known to have a range of characteristic resonant frequencies associated with various modes of vibration of the bond. The final spectrum representing the molecular absorption gives a molecular footprint of the sample. Using an interferometer, all the infra-red frequencies can be simultaneously measured as the interferometer produces a quick and unique type of signal which has all of the infra-red frequencies encoded. With each movement of the mirror (scan), an interferogram (intensity over time) is saved by the detector. The interferogram is then converted into the spectral response by using the Fourier transform.

FTIR of Silicon Oxides

For silicon oxides, the principal modes observed for Si-O bonds are stretching (1075 cm^{-1}), bending (800 cm^{-1}) and rocking (465 cm^{-1}).[122] The frequency of the Si-O-Si stretching band scales monotonically with the concentration of oxygen atom in sub-stoichiometric oxides. This value is 1075 cm^{-1} for stoichiometric SiO_2 and goes down to 940 cm^{-1} for O doped amorphous silicon. This frequency shift can be attributed to the higher probability of Si atoms to find silicon neighbours in Si quantum dot/SiO_x films, as compared to the case of stoichiometric SiO_2. Pai[122] and Tsu[123] used this information and calibrated the Si-O peak frequency (denoted by υ cm^{-1}) with the ratio $R = [Si]/[O]$ measured using electron microprobe technique. Using their results, the value of x (in SiO_x) and the ratio R in a pre-annealed film can be determined by the following equation:

$$x = 0.02\upsilon_{Si-O} - 19.3;\ or\ R = 50/(\upsilon_{Si-O} - 965) \tag{2.7}$$

The FTIR measurements were performed on the *Biorad QS500-ANA FTIR* spectrometer, and the bond configuration was investigated from FTIR absorption peak positions as has been described above. Each unprocessed wafer was pre-scanned before the deposition to eliminate background effects from the substrate and ensure that the results are only due to the spectral differences between the films.

Using the above relations for the peak at 1043 cm^{-1} in Figure 2.4a, the as-deposited film has been determined as $SiO_{1.56}$, with $R = 0.64$. The peak at 800 cm^{-1} can be either due

to Si-H and Si-O bending. Broad peaks between 1100 and 1300 cm^{-1} can be attributed to the lack of excess He in the deposition step, leading to the presence of SiH, SiN and NH bonding groups in the as-deposited film.[122]

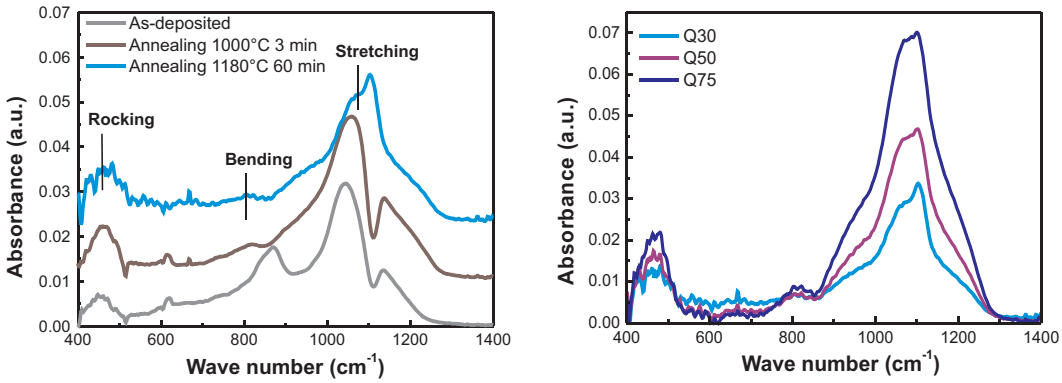

(a) (b)

Figure 2.4: (a) FTIR absorbance for the as-deposited (Q30) and annealed films showing Si-O rocking, bending and stretching. The excess silicon content can be determined from the Si-O stretching frequency. (b) Post-annealing samples Si-O stretching peak intensity scales with the film thickness.

Additionally, it is interesting to observe the change in the spectra after the annealing step (Figure 2.4b). On deconvolution of the Si-O stretching peak for Q75, the phase separation of silicon rich oxide into SiO_2 becomes evident as the Si-O stretching shifts towards 1079 cm^{-1}, which is close to the known value of 1075 cm^{-1} for SiO_2 (Figure 2.5a).

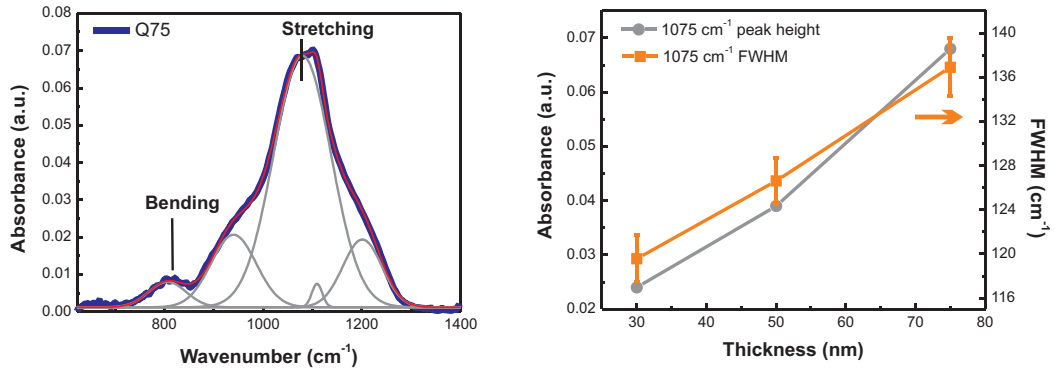

(a) (b)

Figure 2.5: Deconvolution of the FTIR data for annealed sample Q75. (a) The Si-O stretching peak at 1075 cm^{-1} becomes evident after the phase separation of SRO to SiO_2, and its height and FWHM (b) increase with the thickness of the film.

The various peak frequencies and the corresponding bonds are listed in Table 2.3.[122,124]

Observed Frequency cm^{-1}	**SiO_2 Vibrational Frequency** cm^{-1}	**Vibrational Assignment**
806	800	Si-O bending
940	935	O interstitial + Si interstitial in Si
1079	1075	Si-O stretching
1109	1105-1108	O impurity and O interstitial in Si

Table 2.3: FTIR peak frequencies and the corresponding bonds obtained for Q75.[122,124]

The peak intensities increase with an increasing thickness of the oxide layers. Furthermore, this Si-O stretching peak also shows larger FWHM (Figure 2.5b). The large FWHM represents the statistical arrangements of bonds for each atom of silicon and therefore corresponds to the Si-O-Si environment. This enlargement can therefore be attributed to the film comprising of an inhomogeneous silicon dioxide environment with Si-O bonds, also surrounded by a large number of Si-Si bonds in the form of quantum dots. Narrower FWHMs can be expected in a homogeneous SiO_2 environment, where the Si-O bonds are not perturbed by the presence of silicon nanocrystals.[122,124]

2.3.2 Spectroscopic Ellipsometry

Ellipsometry is a non-destructive, non-contact powerful optical analysis technique, commonly used for determining the thickness and composition of thin films. The properties that can be analysed include refractive index n, extinction coefficient k, roughness, material composition, degree of crystallinity, and even the fraction of pores.

Principle Involved

Incident polarized light can be resolved into two components, i.e. p (parallel to the plane of incidence) and s (perpendicular to the plane of incidence). These two components undergo different amplitudes and phase shifts on reflection from absorbing materials, and from multiple reflections in the measured thin film between air and the substrate.

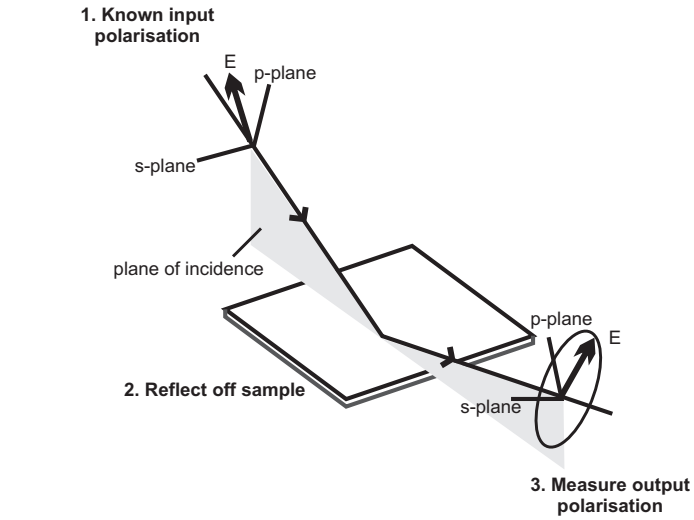

(a)

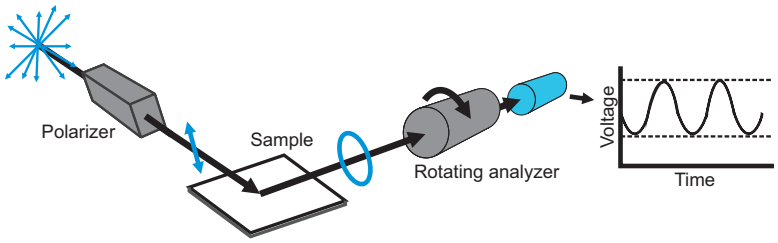

(b)

Figure 2.6: (a) Schematic of reflection of polarized light from a plane surface in ellipsometry. (b) Schematic of setup used in the Woollam VASE ellipsometer.[125]

The p component experiences a phase shift which makes the incident plane polarized light elliptically polarized. In the plane perpendicular to the reflected beam, the resultant electric field vector denotes an ellipse. The technique of ellipsometry thus measures the change in polarization state from the linearly polarised light, to the elliptically polarised light reflected off the sample surface.

Light travels as a fluctuation in electric and magnetic fields at right angles to the direction of propagation. The total electric field comprises of the parallel component ε_p and the perpendicular component ε_s. The Fresnel reflection coefficients r_p and r_s are expressed by:

$$r_p = \frac{\varepsilon_p \text{ (reflected)}}{\varepsilon_p \text{ (incident)}}; \; r_s = \frac{\varepsilon_s \text{ (reflected)}}{\varepsilon_s \text{ (incident)}} \tag{2.8}$$

These values are not directly measurable. However, the ratio ρ of the Fresnel reflection coefficients can be measured and is a function of the ellipsometric angles Δ and Ψ:

$$\rho = \frac{r_p}{r_s} = tan(\Psi)e^{i\Delta} \tag{2.9}$$

$\Delta = \Delta_p - \Delta_s$ characterizes the phase difference between the two polarizations.
$\Psi = \tan^{-1}\rho$ represents the amplitude ratio.

For a single layer, these terms are uniquely determined by the thickness and optical constants of the layer and the substrate, and need to be fitted with a model for extracting the required parameters. Finding the best match between the model and the experiment is typically achieved through regression using an estimator like Mean Squared Error (MSE) to quantify (and minimize) the difference between curves. Done over multiple wavelengths, this technique is called spectroscopic ellipsometry. Variable Angle Spectroscopic Ellipsometry (VASE), was performed on the J.A. Woollam ellipsometer and can acquire data at multiple angles of incidence (55°, 65°, 75°), thus having the advantage of large amounts of data which can then be optimized for improved fits.

Spectroscopic Ellipsometry of Silicon Oxides

In the case of SiO_x deposited by PECVD, we can use spectroscopic ellipsometry to determine the thickness of the deposited layer, as well as its index and composition. The refractive index of the silicon rich oxide (at 633 nm) evolves with Si enrichment, increasing from 1.47 for stoichiometric SiO_2, and approaching values higher than 2.48 for silicon monoxide (x=1). Using the model from San Andres et al,[126] an approximate indication of the silicon enrichment ($SiO_{x=1.3}$) in the film can be determined by the refractive index value at 633 nm (Figure 2.7).

The optical index increase upon annealing can be attributed to both the densification of the as-deposited film, and also the formation of silicon nanoclusters with higher absorption and refractive index.

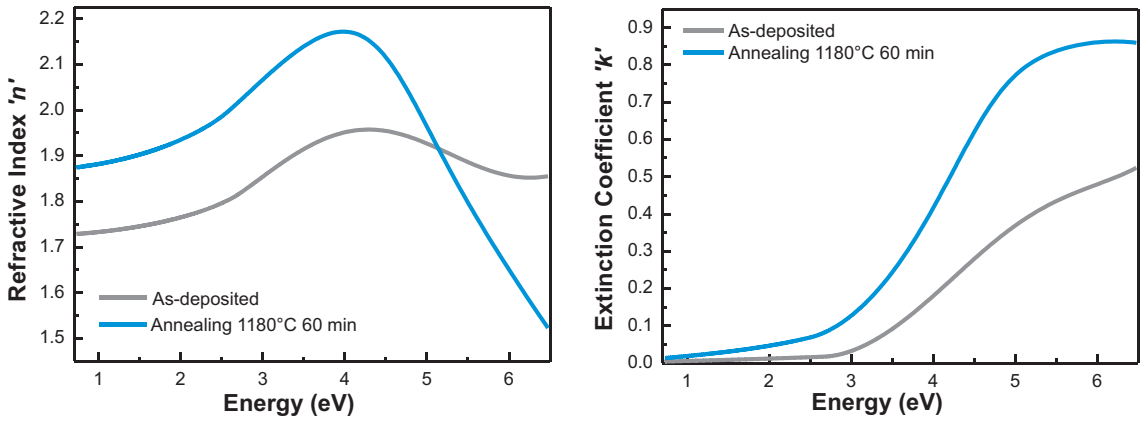

(a) (b)

Figure 2.7: Spectroscopic ellipsometry data showing the variation in refractive index and extinction coefficient with energy on annealing silicon rich oxide films. (a) Refractive index increases on annealing for Q30 due to the densification and formation of silicon nanocrystals (b) Extinction coefficient, related to the absorption in the material, also increases as the nanocrystals are formed.

Figure 2.8 shows the refractive index and extinction coefficient for the 3 different annealed films for variable angles (55°, 65°, 75°) and across a large range of energies. For sample Q75, the optical indices are observed to start approaching those of bulk crystalline silicon. This increase can be attributed to an increased volume of silicon nanocrystals in the annealed films.

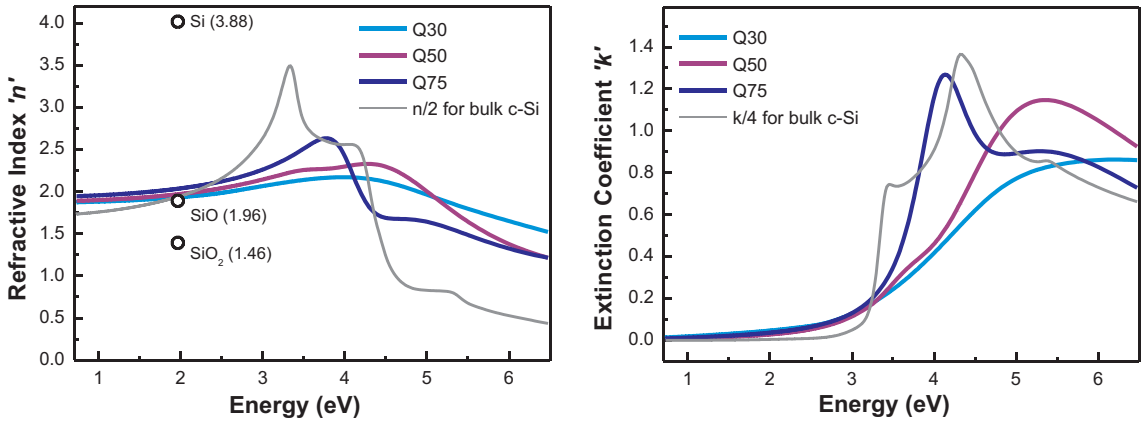

(a) (b)

Figure 2.8: (a) Refractive index n and (b) extinction coefficient k for three different annealed films. n and k for bulk c-Si have been added as a reference. n and k values approach bulk Si for thicker films.

For post annealed samples, two mathematical models, namely the Bruggeman Effective Medium Approximation (BEMA)[127,128] and Tauc-Lorentz Dispersion Model[129] have been compared in Figure 2.9.

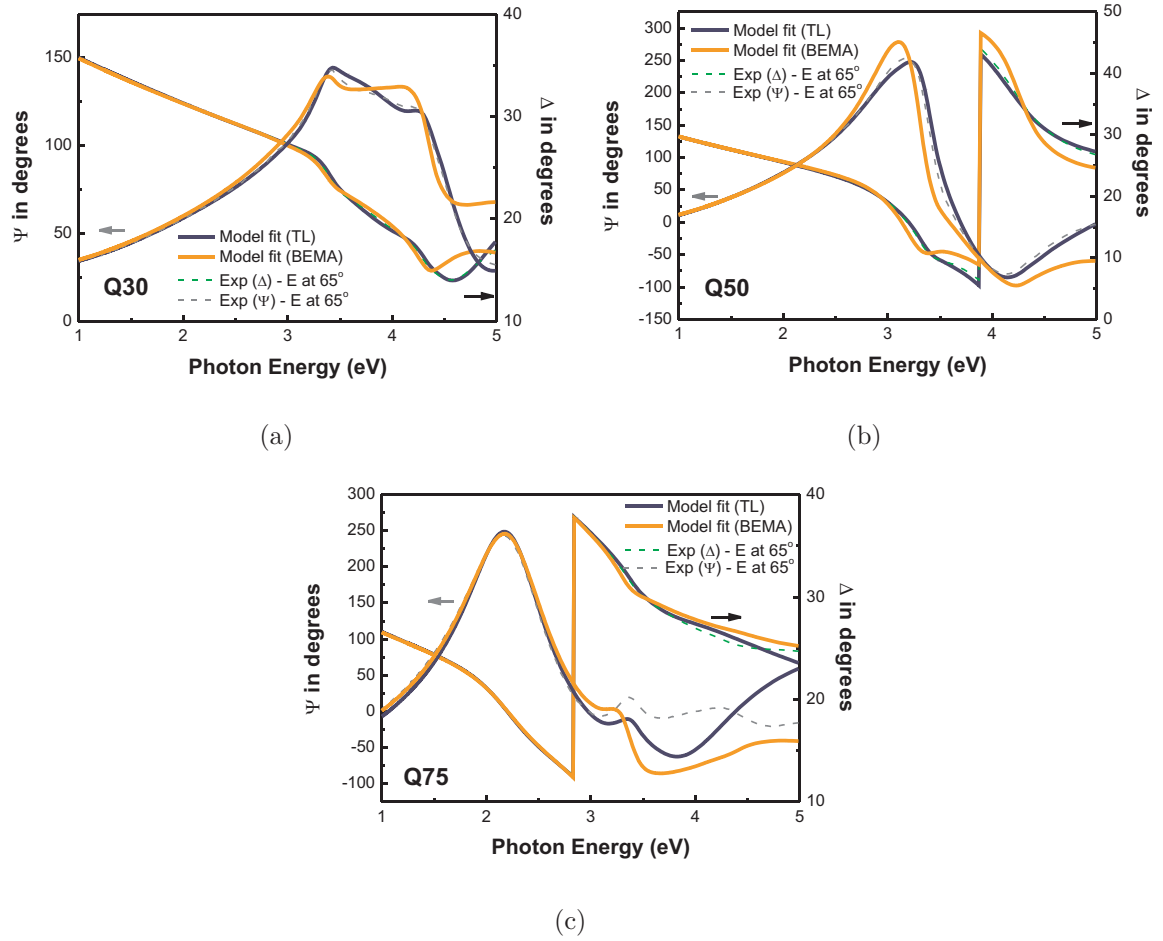

Figure 2.9: Comparison of ellipsometry fits with the Tauc-Lorentz dispersion model and the Bruggeman Effective Medium Approximation at an angle of 65 degrees.

For BEMA, the fit parameters are the film thickness and volume ratios of the different materials (crystalline Si, amorphous Si, SiO_2) in the effective medium. The Tauc-Lorentz model depends on the parametrization of the optical functions of the material. The Tauc-Lorentz model can also predict the optical bandgap of the annealed films, which should correspond to the gap of the quantum dots. Although improved fits with lower MSE were obtained with the Tauc-Lorentz model, some important data can still be extracted from BEMA.

The errors in BEMA are inevitable as the model uses a table of optical indices of bulk materials for the fit. In silicon quantum dots, these values, especially in the visible and ultraviolet region, are altered due to quantum confinement effects. Silicon content in the films can nevertheless be approximated as mentioned in Table 2.4. In all three cases, the SiO_2 content is evaluated to be around 70%, with around 20% crystalline silicon and the rest being amorphous silicon. Both models were used with an additional top rough layer of 1 nm, which combines 50% of the top layer material with 50% voids.

	Tauc Lorentz			**BEMA**				
Sample	*Thickness (nm)*	*E_g (eV)*	*MSE*	*Thickness (nm)*	*SiO_2 (%)*	*c-Si (%)*	*a-Si (%)*	*MSE*
Q30	29.54±0.01	1.96±0.01	12.04	30.12±0.04	76.0	19.2	4.8	41.26
Q50	48.83±0.04	1.86±0.01	25.08	48.80±0.09	73.6	22.5	3.9	82.83
Q75	73.71±0.08	1.81±0.02	67.18	75.21±0.08	70.5	23.5	6.0	97.08

Table 2.4: Tauc-Lorentz and Bruggeman's Effective Medium Approximation (BEMA) model parameters for the annealed films. The film thickness compares well in the two cases. BEMA fit parameters confirm the presence of around 20% crystalline silicon.

2.3.3 Summary

FTIR and spectroscopic ellipsometry are essential techniques for initial and rapid film characterization. Excess silicon content, essential for quantum dot formation, was confirmed, and the non-stoichiometric deposited film was determined to be $SiO_{x=1.56}$. Post-annealing FTIR peaks show a clear separation of the Si-O stretching which is characteristic of SiO_2, thus confirming phase separation. The intensity of this peak depends on the film thickness as the quantity of bonds increases. FTIR results clearly demonstrate the formation of stoichiometric SiO_2 on annealing. Similarly, the refractive index increase on annealing due to both densification and formation of Si confirms the presence of quantum dots. The three annealed films show nearly identical volume fractions of SiO_2, a-Si and c-Si. From the results obtained so far, film properties and quantum dot formation do not appear to significantly depend on the thickness of the initially deposited layer. These two techniques can therefore successfully be utilised for a rapid evaluation of Si enrichment after the deposition step, and the formation of quantum dots after the annealing step.

2.4 Quantum Confinement in Si Quantum Dots

As described in Chapter 1, quantum confinement for Si starts when the diameter of the dot is less than the Bohr exciton radius. A variety of techniques can be used to evaluate the diameter of the dots and obtain additional information on properties like their optical bandgap, crystallinity, size distribution and even spatial order. This section will deal with experimental results obtained with such techniques which involve the properties of these low dimensional systems.

2.4.1 Photoluminescence Spectroscopy

Photoluminescence can be described as the emission of photons by a material under optical excitation. Light is directed on a sample where it is absorbed producing excess energy inside the material in a process called photo-excitation. The photo-excitation causes electrons to move to permitted excited states. As the electrons relax back to the equilibrium state, excess energy is released producing light emission in a radiative process. This photoluminescence energy is thus related to the difference between the energy levels involved in the transition, i.e. the excited state and the equilibrium state.

Silicon nanocrystals are characterized by an energy gap that is enlarged and blue shifted with respect to that of bulk silicon. This bandgap can be approximated using photoluminescence using the following relation[15,130]:

$$E_{PL} = E_0 + \frac{3.73}{d^{1.39}} + \left[\frac{0.881}{d} - 0.245\right] \tag{2.10}$$

where E_{PL} (eV) is the energy with the maximum photoluminescence intensity, d (nm) is the quantum dot diameter and E_0 is the bulk silicon bandgap. The terms in the square bracket are a correction term to the original equation[130] due to changes in the nanocrystal lattice parameters.[15]

The spectral photoluminescence of silicon nanocrystals has been extensively studied, yet the origin of this room temperature luminescence is still under debate.[101,121,131,132] The

emission from Si quantum dots can be attributed to an overall contribution from: *(i)* Nanostructured silicon, where quantum confinement leads to shift in the emission band depending on quantum dot size.

(ii) The interfacial zone between Si and SiO_2, with emission at around 800 nm.

(iii) Sub-bandgap localized states in amorphous silicon, present in small quantities.

(iv) Radiative defects present in the SiO_2 matrix.

Although the near-infrared luminescence observed from 650 nm to 950 nm is characteristic of band-to-band recombination of quantum confined excitons, yet Si-O interface states and silicon lattice defects may play a major role by emitting photons at lower energies than predicted by theory. Thus the PL spectra may be attributed to misinterpreted defect luminescence within the oxide matrix, although it occurs due to both defects and quantum confinement. As discussed earlier, hydrogen can passivate these defects but UV excitation removes this hydrogen, again leaving the defect unpassivated.[121] The emission wavelength of the quantum dots can be controlled by tuning the diameter of the nanocrystals as it blueshifts with decreased nanocrystal size.

For the three samples discussed in this chapter, the room temperature photoluminescence spectra have been shown in Figure 2.10.

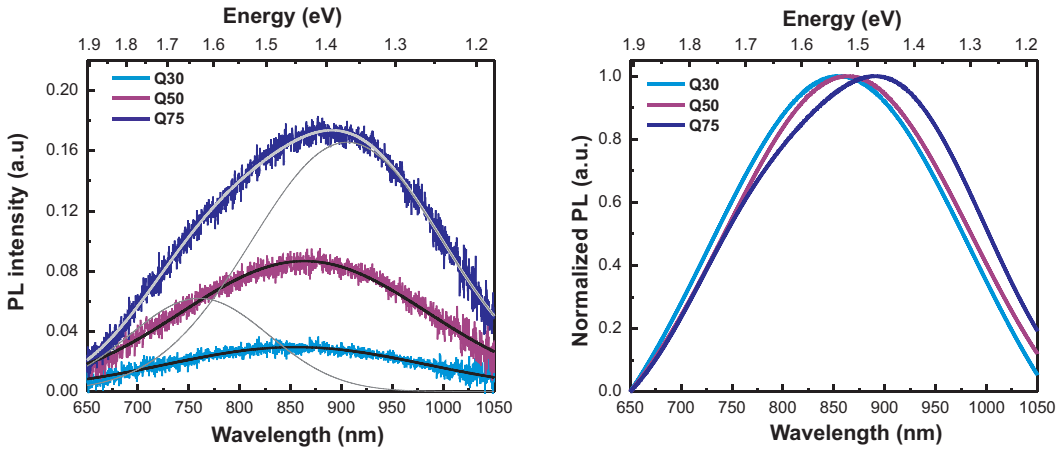

(a) (b)

Figure 2.10: PL intensity versus wavelength for samples Q30, Q50 and Q75. (a) The PL spectra and their fits show intensity scales with film thickness. (b) Normalized PL fits. The intensity maximum for the three samples lie at: Q30 - 855 nm; Q50 - 863 nm; Q75 - 890 nm. Multiple Gaussian distribution observed for Q75 (756 nm and 905 nm).

These samples were excited using a 355 nm laser and the emission was then measured. The exposure time was 1 second and the data have been corrected for disturbances coming from the white lamp. All three samples show large FWHM with similar intensity maximum at 855 nm (Q30), 863 nm (Q50) and 890 nm (Q75). Multiple Gaussian distributions are observed for the sample Q75 (756 nm and 905 nm). The large FWHM of the peaks can be due to both the uncontrolled size distribution and the defect luminescence. The average size of the nanocrystals can be related to the maximum emission wavelength. For the three samples, the average bandgap lies between 850 and 900 nm (1.46 and 1.36 eV), well within the range of quantum confinement. Additional experiments are however required to confirm the presence of quantum dots.

2.4.2 Transmission Electron Microscopy

Principle of Transmission Electron Microscopy

Transmission electron microscopy (TEM) is a microscopy technique where a thin beam of electrons, focussed using electromagnetic lenses, travels through and interacts with an ultra-thin specimen. Depending on the density of the material present, some electrons are scattered and disappear from the beam. The unscattered electrons hit a fluorescent screen, giving rise to an image of the specimen, varying in darkness according to the density of different parts. Diffraction contrast is also exhibited when the electron beam undergoes Bragg scattering in the case of crystalline samples. A series of lenses are used to magnify the sample, approaching high resolutions of up to 0.15 nm. Grain size and lattice defects can thus be studied using the image mode.

Energy-filtered Transmission Electron Microscopy (EFTEM) is a technique where only electrons of particular energies are used to form the image or diffraction pattern. The energy slit can be adjusted to allow only those electrons to pass through which haven't lost energy. This decreases contributions from inelastic scattering leading to high contrast images. Adjusting the slit to allow passage of specific energy electrons can also be used to differentiate between materials.

TEM Analysis of Si Quantum Dots

Conventional bright field (BF) TEM imaging of Si nanocrystals in SiO_2 can be difficult due to the low contrast in the elastic signal. This contrast can be improved by using plasmon filtered microscopy, by imaging in a narrow energy window around the Si (16 eV) or the SiO_2 (24.4 eV) plasmon energy loss peak.[133,134] Figure 2.11a shows the plan-view micrographs for the sample Q30.

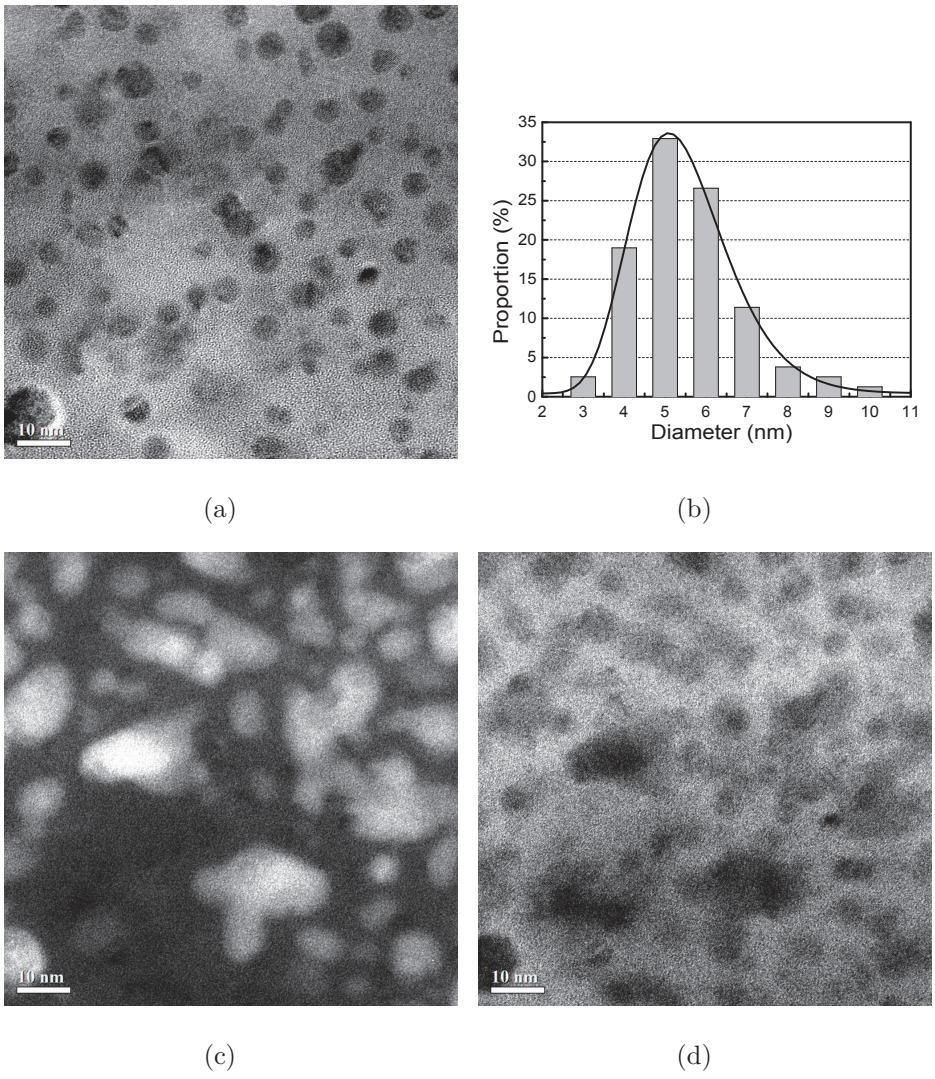

Figure 2.11: (a) Plan-view TEM micrograph of sample Q30. (b) Size distribution of the dots calculated using a log normal fit with mean dot diameter 5.34±0.03 nm. (c) EFTEM for the micrograph in (a) at 16 eV energy loss with Si in the bright zones and SiO_2 in dark contrast (d) EFTEM at 24.4 eV for Si in dark zones and SiO_2 in bright contrasts.

At 16 eV, silicon is in bright zones in contrast with the dark SiO_2, and vice versa

at 24.4 eV. In addition to distinguishing the two materials, we can observe the spatial distribution of the dots as well as presence of the dots that were not aligned to the plane of the TEM observations. High resolution TEM aids in visualization of the silicon quantum dots, and their crystallinity and size distribution.

Analysing the number of Si quantum dots as observed from Figure 2.11b, we obtain an average size of 5.34±0.03 nm using a log normal fit. Figure 2.11c and Figure 2.11d are the corresponding EFTEM micrographs at 16 eV and 24.4 eV respectively, showing a high density of dots throughout the measured sample. The large bright zones in Figure 2.11c can be attributed to large and irregular silicon nanoclusters or zones of amorphous silicon.

2.4.3 Grazing Incidence X-ray Diffraction

Description of GIXRD

X-ray diffraction at grazing/glancing incidence (GIXRD) is a technique allowing measurement of XRD patterns of thin films as the penetration depth is only a few nanometres. As the angle of incidence i of the x-ray beam decreases, the beam will not penetrate (or refract) as deeply into the sample. When this angle goes below a critical angle i_c, total external reflection occurs. Much of the x-ray beam is reflected, and the refracted beam propagates parallel to the interface, while being exponentially damped below the interface.

GIXRD of Silicon Nanocrystals

The silicon quantum dots are in fact small crystallites and can therefore be observed using x-ray diffraction, another powerful non-destructive tool for quantitative information on crystalline phases in thin films. Since these dots were embedded in films of less than 100 nm thickness, ordinary diffraction may be somewhat difficult due to small volume of crystalline material in the layers and strong contributions from the substrate. The refracted beam in GIXRD is used for the verification of crystallinity in the form of dots

in the otherwise amorphous SiO_2 matrix.

Linearly increasing intensities of crystalline Bragg peaks at 28.4°, 47.5° and 56.1° were observed which correspond to the Si Bragg peaks (111), (220) and (311) respectively (See Figure 2.12). This confirms that the crystallinity of the quantum dots depends and scales with the amount of material deposited initially.

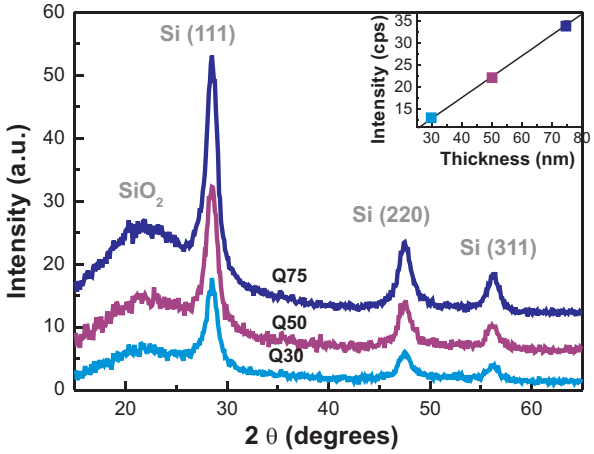

Figure 2.12: Grazing Incidence x-ray Diffraction patterns for the 3 films. The data has been translated for convenience. Si crystalline peaks are clearly visible. The inset shows that the peak intensity scales with the film thickness. Using the Scherrer equation, the nanocrystallite size was calculated to be 4.9 nm (Q30), 5.3 nm (Q50) and 5.1 nm (Q75).

XRD peak broadening due to the nanometric size of the dots can be used to estimate their diameter using the Scherrer formula for the 28.4° Si (111) peak. This occurs due to the increased acceptance angle satisfying Bragg condition in the small planes in very small crystallites. This well known equation is as follows,

$$L_{vol} = \frac{K\lambda}{\Delta 2\theta \, cos\theta} \tag{2.11}$$

where L_{vol} is the volume weighted size of the crystallites, K is the shape factor (a constant depending on shape and size distribution of crystallites. K = 0.9 for spheres), λ is the x-ray wavelength, $\Delta 2\theta$ (in radians) is the integral breadth of the Bragg peak.[54,135] The Scherrer equation has been used with the integral breadth and not the FWHM in order to be independent of the shape (Gaussian or Lorentzian) of the peak. Assuming spherical

quantum dots, the dot diameter d is then defined by[136]

$$d = \frac{4L_{vol}}{3} \tag{2.12}$$

Using the above equations for the 28.4° Si (111) peak, the quantum dot diameter was calculated to be d = 4.9 ± 0.5 nm, 5.3 ± 0.5 nm and 5.1 ± 0.5 nm respectively. These results thus not only confirm the formation of Si nanocrystals but also successfully permit an estimation of their size, which is in good agreement with the TEM interpretation.

2.5 Summary of Characterization Techniques

Plasma enhanced chemical vapour deposition followed by high temperature annealing of silicon rich oxides has been successfully used for the fabrication of nanocrystalline luminescent quantum dots of silicon in a matrix of SiO_2. Characterization techniques have been established that will further aid us in understanding and improving quantum dot properties and dot size control.

Dots of 5 nm average diameter were successfully fabricated although with little control over the dot size distribution. Excess silicon in the as-deposited films was characterized using FTIR and spectroscopic ellipsometry, which are both non-contact techniques for rapid characterizations. They also provide quick information on the phase separation of the silicon rich oxides after annealing, silicon enrichment, optical indices, band gap and film thickness.

Techniques like photoluminescence, grazing incidence x-ray diffraction and TEM give an insight into dot size, gap and defects. Photoluminescence proves the presence of absorbing and emitting quantum dots, and grazing incidence x-ray diffraction verifies the presence of nanocrystallite structures. TEM micrographs finally establish and allow the visualization of the quantum dots. A comparison of results from different techniques can be seen in Table 2.5 below.

Sample	**TEM**		**GIXRD**		**Ellipsometry**		**Photoluminescence**	
	Size	**E_{PL}***	**Size**	**E_{PL}***	**Size***	**E_g**	**Size***	**E_{PL}**
	nm	*eV*	*nm*	*eV*	*nm*	*eV*	*nm*	*eV*
Q30	5.3±0.5	1.45	4.9±0.5	1.51	3.2	1.96±0.01	5.4	1.44±0.2
Q50	5.3±0.5	1.45	5.3±0.5	1.45	3.4	1.86±0.01	5.4	1.44±0.2
Q75	8.2±0.8	1.25	5.1±0.5	1.48	3.5	1.81±0.01	5.8	1.39±0.2

Table 2.5: Comparing diameters and expected peak photoluminescence energy for the fabricated quantum dots show a fair similarity between the different techniques. E_{PL} has been calculated for the sizes determined by TEM and GIXRD for comparison. Average E_{PL} and dot diameter values were used in the case of Q75, in spite of multiple Gaussian distribution observed.$*$ represents calculated values using Ledoux et al[15]

.

Dot diameters estimated using different experimental techniques correspond well with each other, and also with calculated E_{PL} values. The differences in the energy gap evaluation from the Tauc-Lorentz model of spectroscopic ellipsometry can be due to the lack of perfect fits. The average quantum dot size in each of the three films can be estimated to be 5.0±0.8 nm. The techniques thus established in this chapter can now be used for quantum dot characterization of more complicated structures. The films developed in this chapter can be further characterized for electrical conduction phenomena.

Chapter 3

Film Thickness Dependent Order in Single Layers

Silicon quantum dots are formed by the diffusion of excess silicon in sub-stoichiometric silicon dioxide layers on high temperature annealing. The diffusion of silicon can vary in the films, depending on the enrichment and annealing conditions. In this chapter, the differences in the spatial organization of silicon quantum dots with different single layer thicknesses will be discussed. The consequence of these differences is further explored in electrical characterization of the films. The conduction phenomena in the silicon quantum dots and the outcomes of experiments on metal-insulator-semiconductor (MIS) type structures will also be examined. Samples Q30, Q50 and Q75 are analysed for an insight into the thickness dependent conduction mechanisms.

3.1 Spatial Organization of Si Quantum Dots

Samples Q30, Q50 and Q75, with identical initial stoichiometries, were annealed to form Si quantum dots due to the phase separation of Si and SiO_2. From the characterizations and analysis of Chapter 2, it was concluded that the films were identical and all nanocrystal properties like Si content, crystallinity etc. scale with layer thickness.

Silicon nanocrystallites fabricated with the phase separation technique comprise of structural faults, lattice defects, dislocations or twinning, especially as the crystalline quantum dots transition into the amorphous SiO_2 matrix. Only those dots whose crystal planes are aligned with the measurement can be observed with TEM. The presence of structural defects is illustrated in Figure 3.1 for sample Q75.

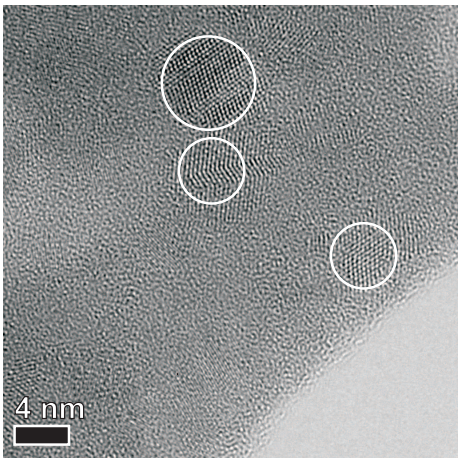

Figure 3.1: Plan-view EFTEM micrograph for sample Q75 showing silicon dislocations and lattice defects.

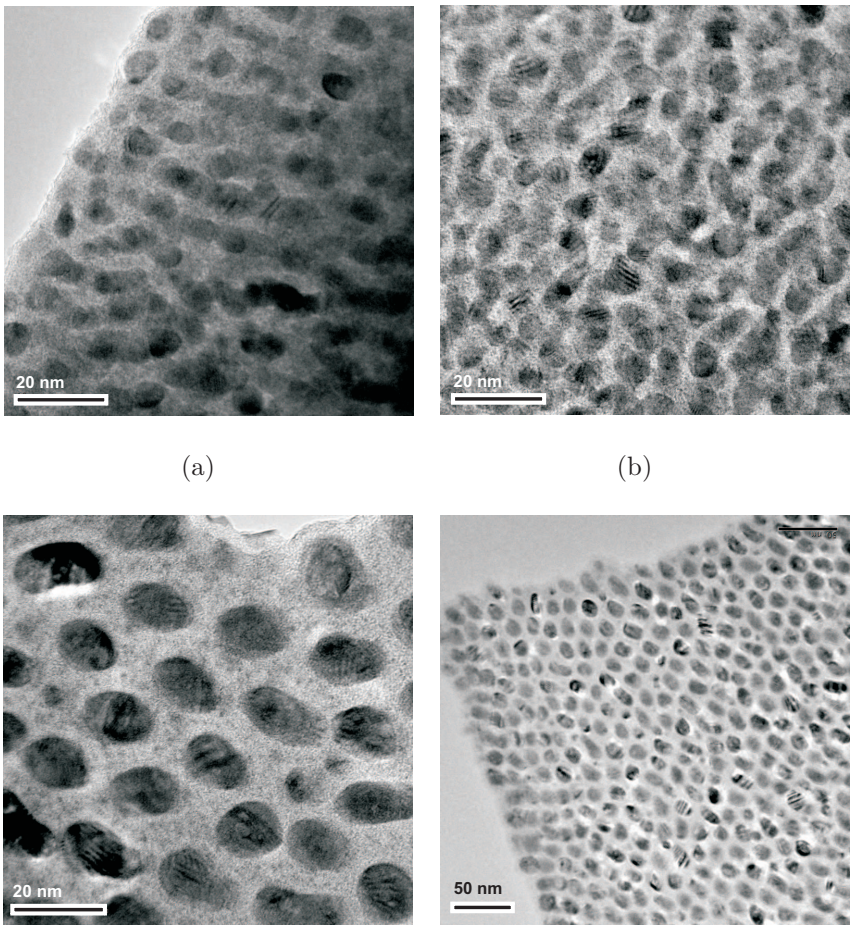

Figure 3.2: (a, b, c) Plan-view TEM of samples Q30, Q50 and Q75 respectively show an evolution from randomly arranged quantum dots to an ordered spatial distribution. (d) Sample Q75 shows an ordered formation of quantum dots.

Copper precipitation on defects and dislocations in silicon[137–139] is a well known phenomenon, as Cu is known to have an affinity for dislocations in silicon forming Cu_3Si configuration. During plan-view TEM sample preparation using ion-milling with the *Gatan Precision Ion Polishing System* for thinning the films, some of the copper from the Cu sample holder was re-deposited on the silicon dioxide with embedded Si quantum dots. Considering that the dots comprise of numerous lattice defects, the high contrast in the TEM micrographs of Figure 3.2 can be attributed to this copper that was deposited on the silicon dots. While this is disadvantageous for observing silicon crystals, it is a unique and extremely powerful technique for visualizing the spatial distribution of silicon in the layers as observed in Figure 3.2. A clear lateral organization of dots is observed which depends on the thickness of the initial as-deposited film. A shift from randomly organized dots in Figure 3.2a to an ordered superlattice in Figure 3.2d is clearly evident.

To confirm that this superlattice like structure is a result of self-organization in quantum dots and is not a consequence of arbitrary copper contamination of the sample, another sample was prepared (Figure 3.3) for Q75. Cu contamination was carefully avoided and EFTEM micrographs were observed to illustrate Si and SiO_2 contrast with 24.4 eV plasmon excitation energy. The ordered structure reappears with Si in dark zones.

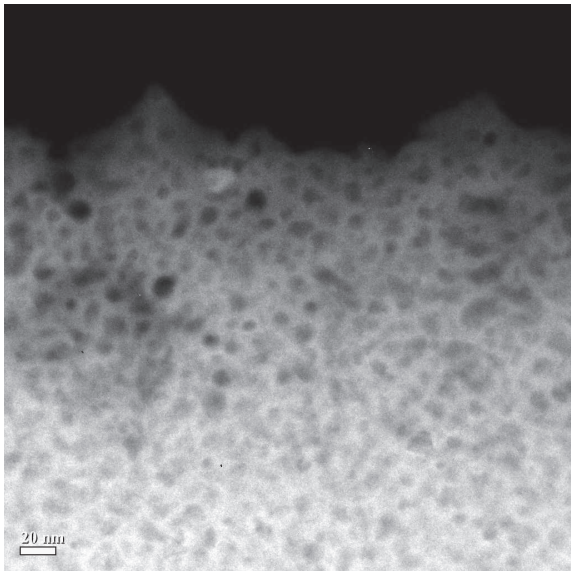

Figure 3.3: Plan-view EFTEM micrograph with 24.4 eV plasmon energy confirming ordered silicon quantum dots in dark zones for Q75.

3.1.1 Elucidation of Thickness Dependent Order in Si Quantum Dots

Short range hexagonally ordered silicon nanocrystal arrays have been previously reported by Gago et al.[103] Such hexagonal self-ordered configurations have also been observed for Ge in SiO_2, and can be attributed to both diffusion dynamics,[140–142] and also strain in the film[143] for an ordered array of quantum dots. Assuming a similar organization in our case, it can be inferred that spatial distribution of the quantum dots varies with the three different thicknesses, as observed in Figure 3.2. As the three samples were fabricated with the same initial deposition and annealing conditions, and structural characterizations show nearly identical film properties, this difference can be attributed to the initial thickness of the deposited films.

In our case, the most likely explanation for the formation of this 3D-superlattice arrangement of the Si quantum dots is the diffusion of Si in SiO_x. For formation of silicon nanocrystals, the nucleation step occurs at high temperatures at excess silicon sites in the silicon rich oxide. These nuclei capture neighbouring silicon atoms forming spherical silicon dots in a stable stoichiometric SiO_2, and thereby prevent the formation of another quantum dot in the close vicinity. For the present conditions of Si excess, annealing temperature and time in these samples, this diffusion length can be approximated to be 12 nm using the model established by Nesbit.[100]

We hypothesize that this diffusion phenomena is affected by the substrate-SiO_x layer interface, the surface of the film and also the silicon adatoms. In the case of sample Q30, it is certainly probable that the Si diffusion is affected by the boundaries of the SRO film that somehow hinders the formation of ordered QD arrays. Indeed, experimental data have shown that film interfaces play a key role on the dot crystallization phenomenon.[144] On the other hand, as the film thickness becomes much larger than both, the diffusion length of silicon in the matrix and size of the dots, a self-ordered array of quantum dots is formed like in the case of Q75.

3.2 Electrical Conduction in Si Quantum Dot Films

The differences in organization of quantum dots and their inter-dot distances are likely to affect the electrical conduction in the films. This difference can be characterized by measuring the current-voltage curves at ambient temperature, as well as low temperature conductivity for elucidating the conduction mechanism.

3.2.1 Characterizing Conduction Phenomena

Fabrication of capacitive devices for electrical characterizations

For electrical characterizations, lithographically defined aluminium pads with front side areas 100x100μm^2 and damascene electrodes were fabricated using standard micro-electronics techniques, as illustrated in Figure 3.4. An additional annealing step was performed under forming gas at 425°C for passivation of Si-SiO_2 interface states.

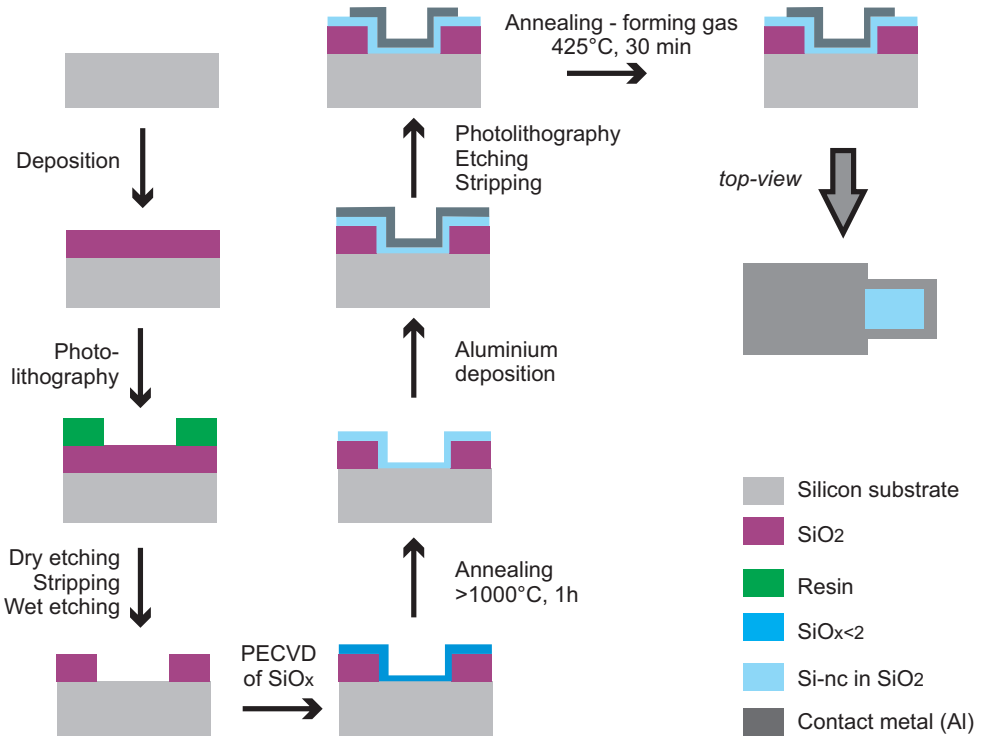

Figure 3.4: Fabrication process for formation of capacitor-like devices with electrical contacts, and Al contact electrode.

The chips used for electrical measurements are represented in a schematic in Figure 3.5

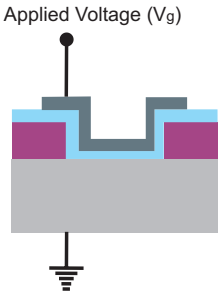

Figure 3.5: Capacitive devices used for electrical characterizations of quantum dots.

Transport mechanisms in Si Quantum dot arrays

Several conduction mechanisms have been proposed for conduction between silicon quantum dots. These include thermionic emission of electrons against grain boundaries, variable range hopping (VRH), nearest neighbour hopping (NNH), tunnelling, percolation and space charge limited current (SCLC).[145,146] While a detailed analysis on the conduction between dots is beyond the scope of this thesis, it is nevertheless imperative to examine the possible conduction mechanisms present in our films.

3.2.2 Current-Voltage Characteristics of Si Quantum Dot Layers

For dot-to-dot conduction, an inter-dot distance of less than 2 nm is prerequisite in the case of silicon oxides. The current density - voltage has been plotted at room temperature for parametric electric measurements made on mesas of area 100x100μm^2, measured on 49 different capacitors at the centre of the wafer. In Figure 3.6, a uniform current density distribution can be observed for Q30, in comparison with Q50 and Q75. Current density is observed to decrease by a factor of nearly 10^3 for a 20 nm increase in film thickness.

3.2.3 Low Temperature Conductivity

Conductivity of the three films was then studied using an *Agilent B1500* device, to analyse the relationship between the spatial distribution of the dots and the conduction phenomena. Low temperature current-voltage measurements were performed under

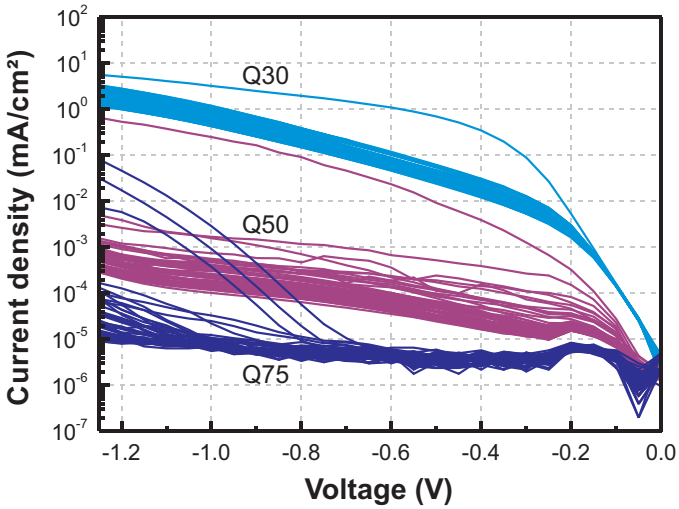

Figure 3.6: Current density vs voltage for 49 capacitors measured on each of the three samples. The current density decreases by an order of 10^3 as the thickness increases from 30 to 50 nm (at room temperature).

liquid N_2 under vacuum, with a temperature range of 80 K - 300 K. It was assumed that most Si-SiO_2 interface defects have been passivated by hydrogen after a forming gas anneal as suggested by Godefroo et al.[120] The role of hydrogen passivation is important in understanding conduction phenomena.

Tunnelling conduction[147] and Mott's equation[146,148] have previously been used to describe temperature (T) dependant conductivity (σ) in quantum dot systems, where Mott's equation is given by

$$\sigma(T) = k\, exp\left(\frac{T_0}{T}\right)^m \tag{3.1}$$

The value of m determines the conduction phenomena and possible values include 0 (corresponding to direct tunnelling), 0.25 (Variable Range Hopping), 0.5 (Nearest Neighbour Hopping NNH) and 1 (thermionic emission).

Figure 3.7 shows the complete current density versus voltage curves measured from 80 K to 300 K after H passivation, and these have been compared to the corresponding non passivated samples at -1.0 V. These graphs illustrate several important results.

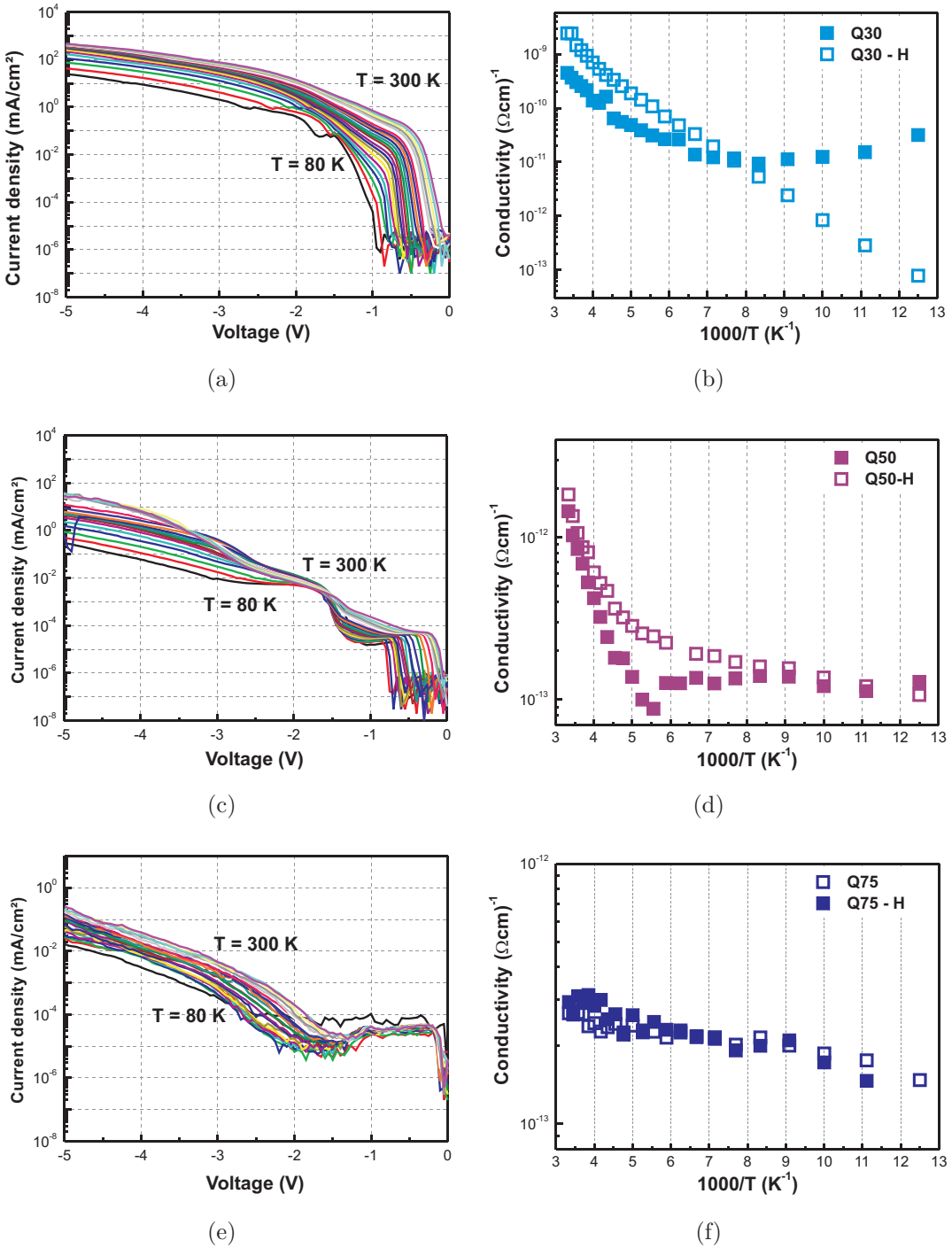

Figure 3.7: (a), (c) and (e) show current density measurements after hydrogen passivation and between 80K and 300K for films Q30 (30 nm), Q50 (50 nm) and Q75 (75 nm) respectively. The dependence of conduction mechanism on the applied voltage is evident. In the corresponding figures (b), (d) and (f), we can see conductivity vs 1000/T at -1.0 Volts before and after hydrogen passivation, showing changes in conduction phenomena but also slightly improved conductivities.

Effect of Hydrogen Passivation and Electric Field Dependence

For 30 nm film samples (Q30) and 50 nm samples (Q50), the change in conductivity before and after H-passivation is significant, confirming the effectiveness and necessity of forming gas annealing on the Si-SiO_2 interface defects. In addition, for Q50 and Q75 films, the conduction phenomena are strongly dependent on voltage (or applied electric field). The electrical data were compared for the temperature range 80 K - 300 K at -1.0 V in Figure 3.8, to characterize the Si quantum dot films instead of the Schottky junction formed due to Al on p-Si substrate. This Schottky junction leads to a flat band voltage of around -0.8 V for the Al-oxide-semiconductor device used. By comparing conduction phenomena at -1.0 V, the voltage was kept low enough to be in a range appropriate to any photovoltaic applications, as the conduction phenomena are likely to vary for higher electric fields.

Temperature Dependence of the Electrical Conductivity

Differences in conduction phenomena depending on film thickness are made clearer in the Arrhenius plot (conductivity vs 1000/T) of Figure 3.8, which shows the change in conduction mechanisms as well as decrease in conductivity with increasing film thickness.

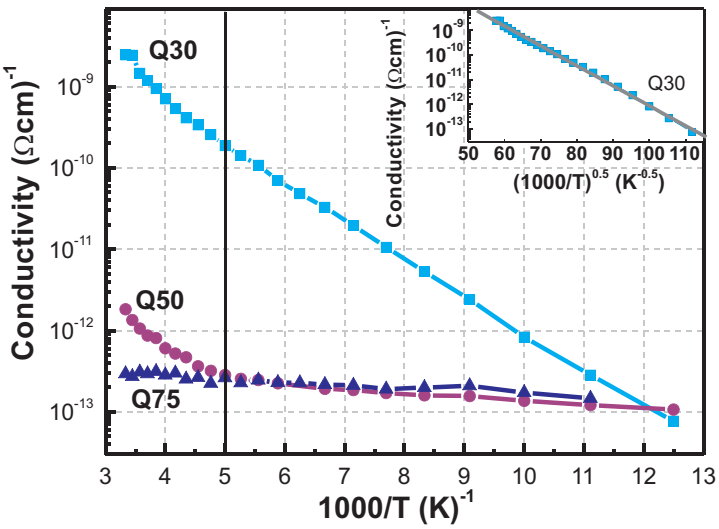

Figure 3.8: Conductivity as a function of temperature at low electric field (-1.0 V) between 80K and 300K for samples Q30, Q50 and Q75 (after H-passivation). A transition is observed at 200K. The inset shows a linear fit for m=0.5 in Mott's equation for sample Q30.

- In the case of Q30, the conductivity decreases strongly with decreasing temperature. On using Mott's relation, for Q30 we get $m = 0.5$, indicating Nearest Neighbour Hopping conduction.

- For Q50 at -1.0 V, after passivation the temperature dependence is still large for T>200 K, but decreases significantly for lower temperatures as has been observed previously by Rafiq et al[145,149] in amorphous semiconductors. This change has been attributed to a transition from thermally activated conduction to some kind of temperature-independent hopping mechanism at lower temperatures.

- For Q75, there is almost no dependence of conductivity on temperature in the Arrhenius plot ($m \simeq 0$).

The order in the structure and inter-dot distance for Q75, as seen from the TEM micrographs in Figure 3.2 strongly indicates direct tunnelling between dots. As the inter-dot distance is more homogeneous in the case of Q75, percolation conduction pathways are expected to decline. However the room temperature conductivity is lower than that for the films Q30 and Q50. The decrease in conductivity with thickness could be due to traps from a large number of crystal defects which were not passivated under hydrogen annealing. Furthermore, slightly larger inter-dot distance in case of ordered dots in Q75 limited the tunnelling probabilities, decreasing electrical conduction.

Conduction phenomena and ordered quantum dots

The conductivity results indeed correspond well to the TEM micrographs observed in the previous section. A completely disordered organization of dots in Q30 improves percolation hopping conduction pathways, leading to improved conductivity. As the dots demonstrate a quasi-hexagonal organization in Q75, the inter-dot distances show less variations and may be larger than 2 nm, therefore decreasing direct tunnelling probability. While the nature of the quantum dots formed in the oxide matrix remains the same in the three different films as seen from structural characterizations of Chapter 2, it is their spatial distribution that results in the change of electrical conduction mechanisms and charge transport.

3.2.4 Capacitance-Voltage and Photocarrier Generation

Finally, to demonstrate photocarrier generation in the Si quantum dot superlattice of sample Q75, capacitance-voltage measurements were performed on a sample with a semi-transparent Al film and a bus bar to form a metal-insulator-semiconductor (MIS) device. The aluminium film was 7 nm in thickness to allow incident light to be transmitted in the quantum dot layer. Rectifying behaviour was seen in dark and illuminated conditions (white light). A clear hysteresis effect was observed (Figure 3.9), which further broadened under ambient illumination. This behaviour can be attributed to photocarrier generation in the Si quantum dot layer and the charging-discharging cycle of the nanocrystals. This memory effect was only observed at high frequencies (1 MHz), corresponding to time scales of microseconds, which are much larger than time-scales of photovoltaic phenomena, and should thus not influence PV properties.

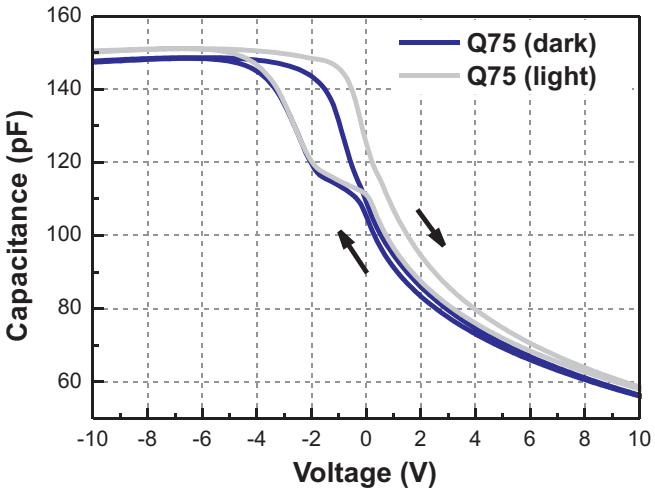

Figure 3.9: C-V measurements at 1 MHz for Q75 ordered films show hysteresis broadening under ambient illumination, confirming photocarrier generation.

3.3 Summary and Concluding Remarks

The thick single layer films show a thickness dependent ordered arrangement of quantum dots of an approximate average diameter of 5 nm. However, a large number of lattice defects are present in these dots. Affinity of copper to these silicon dislocations permits the visualization of the arrangement of the dots using TEM, as copper from the

sample holder was deposited on the quantum dot positions during the ion-milling process.

The quasi-hexagonally ordered arrangement can be explained by the diffusion of silicon in the silicon rich oxide layer during the annealing step, which is limited by the film boundaries. Thinner films show randomly ordered silicon quantum dots, and also demonstrate hopping conduction in electrical conductivity measurements. As a near-hexagonal order is achieved in thicker single layers, the inter-dot distance is more homogeneous. The electrical conductivity is then observed to be almost independent of temperature indicating tunnelling conduction. The decrease in conductivity can be attributed to inter-dot distances of larger than 2 nm, which decrease tunnelling probability.

The effect of H-passivation on the conduction phenomena was also clearly observed. While Si-SiO_2 interface defects can be passivated by annealing under forming gas, dislocations and lattice defects still remain in silicon quantum dots and can influence the opto-electrical properties. Nevertheless, photocarrier generation was observed in capacitance-voltage loops, being a positive sign for potential photovoltaic applications.

Chapter 4

From Single Layers to Multilayers

This chapter deals with the fabrication of alternating multilayer structures of ultra-thin SiO_2 and SiO_x on 200 mm silicon wafers. The problem of fine control over deposition rate, with simultaneous control over silicon enrichment and optical indices will be reviewed. Additionally, we will work towards achieving ideal and optimum deposition and annealing conditions for large scale formation of size-uniform luminescent silicon quantum dots embedded in SiO_2.

4.1 Single Layers Structures

In the preceding chapters, single layers were used for the initial understanding of the characterization techniques. The requirements for improvement of the device structure for eventually testing a photovoltaic device were established. Multiple bilayer structures simultaneously solve several problems of thick single layers - the inter-dot distance and also the size and statistical distribution of the quantum dots. Using a PECVD adaptation of the method established by Tsybeskov[27] and Zacharias,[104] multilayer silicon quantum dot superlattices were fabricated in SiO_2.

The process involves alternate depositions of silicon rich oxides and stoichiometric SiO_2 of less than 2 nm to ensure electrical conduction. The size of the quantum dots is limited by the thickness of SRO layer, as shown in Figure 4.1. The size is limited as excess silicon in the SRO layer cannot diffuse through the SiO_2, preventing formation of dots larger than the SRO thickness.

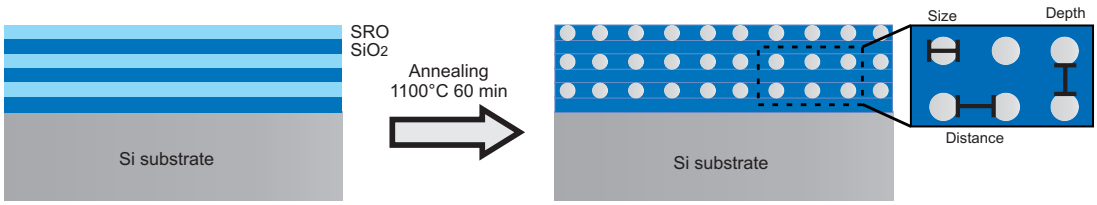

Figure 4.1: Multiple bilayers of SRO and SiO_2 are deposited and then annealed at high temperatures to form silicon quantum dots. The distance between the dots is limited by the thickness of the SiO_2 layers, and the size of the dots is controlled by the thickness of the SRO.[34]

4.1.1 Challenges for Multilayer Depositions

While in principle multilayer depositions are simple, the challenge lay in doing so in the industrial scale *Applied Materials Centura 5200E*, usually used for deposition rates higher than tens of nanometres per second. Furthermore, to obtain uniform ultra-thin layers of silicon rich oxide and SiO_2 on 200 mm wafers, the deposition process needs an in-depth understanding. A coordinated control over the excess silicon in the layers is required for ensuring formation of SiO_2 layers densely packed with silicon quantum dots.

However, it is indeed difficult to separate out the influence of each of the deposition parameters for optimizing the deposition process. These influential factors include, but are not limited to, SiH_4 gas flow, N_2O gas flow, He gas flow, plasma power, chamber pressure, inter-electrode distance and also the deposition time. Furthermore, these parameters are not mutually independent and may have an influence on each other in the form of interactions. Several models have been reported to describe the deposition process of silicon rich oxides. However, they either only consider the ratio $\gamma = N_2O/SiH_4$,[150,151] or a limited number of interactions e.g. plasma power and silane.[152] We attempt to obtain a more complete deposition model, by examining and eliminating all possibilities.

4.1.2 Preliminary Experiments

To decrease the deposition rate from 12.5 nm/sec (Chapter 2) to around 1 nm/sec, gas flow deposition parameters were varied, while an excess of helium was added as a neutral gas.

The deposition temperature was increased to 480°C from the previously used 400°C. This is because a higher temperature in the reaction chamber helps improve the uniformity of the deposited films. The thin-film depositions were carried out for different time periods, with the rf frequency constant at 13.56 MHz, pressure 5.5 Torrs and power 115 W.

Inter-electrode distance

Inter-electrode distance can affect the uniformity and quality of films deposited by plasma enhanced CVD.[153,154] The inter-electrode distance was varied from 400 mils (*1 mil = thousandth of an inch*) to 600 mils, with varying deposition times. Since the best values in terms of highest refractive index with low deposition rate were obtained at 400 mils (Figure 4.2) for $\gamma = N_2O/SiH_4 = 1.14$, all future experiments were performed with this distance.

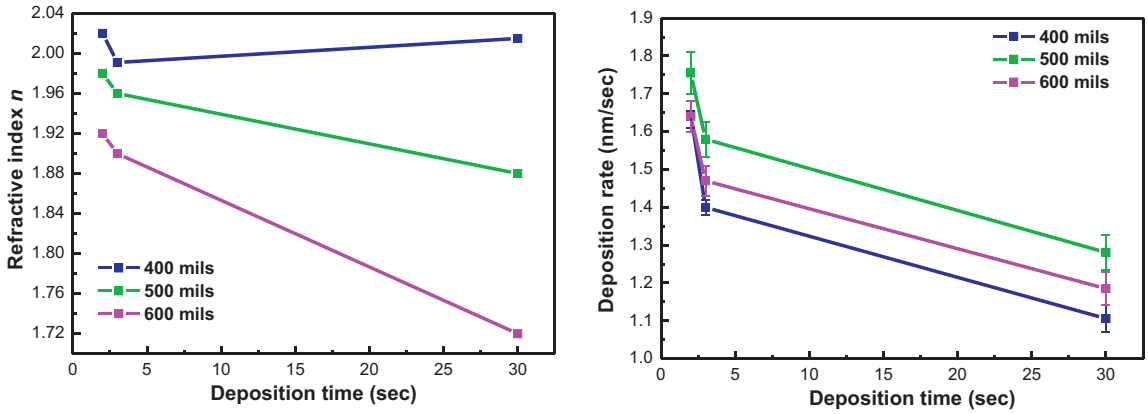

(a) (b)

Figure 4.2: Influence of inter-electrode distance on PECVD process. Improved refractive index (a) and deposition rate (b) were observed for inter-electrode distance of 400 mils.

The Role of Helium

PECVD deposited stoichiometric silicon dioxides without a large excess of helium are known to be porous with large number of defects as compared to a thermally grown SiO_2.[155] Batey et al[156] achieved controlled and slow deposition rates by using a low flow of reactive gases and a much higher proportion of helium as an inert carrier gas to ensure

uniformity. Improved electrical integrity, uniformity and density of deposited films were observed along with lower deposition rates.[157,158]

Helium was used as the inert gas because of its high thermal conductivity, and the ability to suppress unwanted gas-phase reactions. It thus reduces unwanted Si-H, Si-N, Si-OH, N-H bonds which can degrade electrical performance.[122,155] Using the same analogy for sub-stoichiometric silicon oxides, a large excess of helium was added along with low reactive gas flows for achieving the required properties. The volume of helium gas flow was left constant at 1900 sccm.

Gas Flow Ratio

For deposition times of 120 seconds, the influence of the ratio $\gamma = N_2O/SiH_4$ on the refractive index of the layers can clearly be observed in Figure 4.3a. However, the deposition rate depends on the gas ratio and also the individual quantity of either N_2O or SiH_4 as illustrated in Figure 4.3b. Evidently, the total gas flow volume increases, as the deposition rate increases.

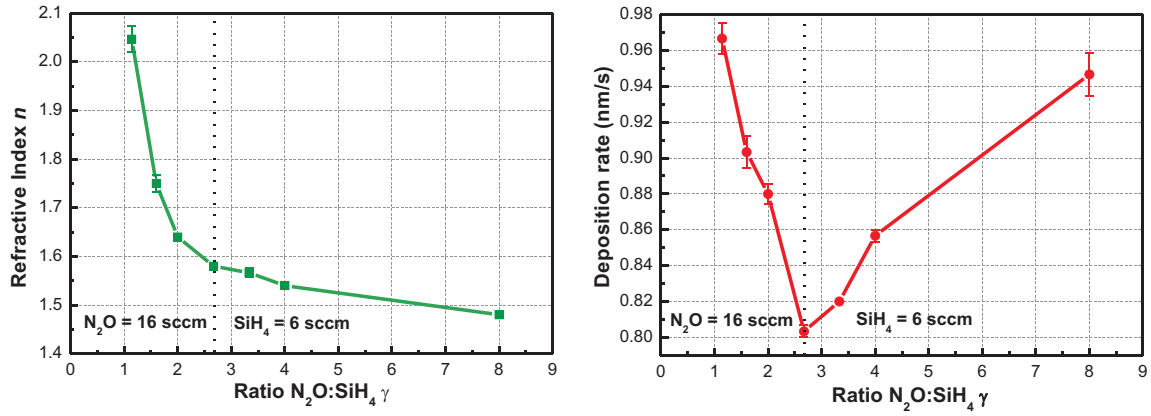

(a) (b)

Figure 4.3: Influence of gas flow ratio $\gamma = N_2O/SiH_4$ on refractive index and deposition rate of SiO_x . In (a) we observe that the highest values of refractive index were obtained for the lowest γ and the highest SiH_4 gas flow. (b) shows that indeed increasing gas flows increase deposition rates.

Deposition Time

Depositions were carried out for $\gamma = 1.14$, with N_2O at 16 sccm and SiH_4 at 14 sccm. For increasing deposition time, the deposition rate was found to decrease exponentially. The gas flows were allowed to stabilise before the deposition step but the plasma power was switched on only during the actual deposition step. Several phenomena thus run in parallel for low deposition times - the initial instability of the plasma, as well as their interaction with the gas flow volumes which need a few seconds to stabilise to give a constant deposition rate. The minimum recommended deposition time for the reactor is 3 seconds.

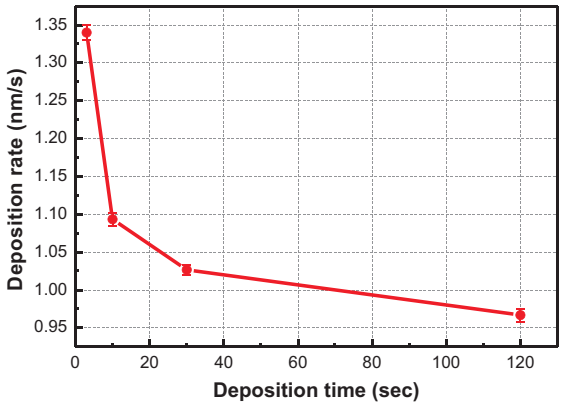

Figure 4.4: Influence of deposition time on the deposition rate. For constant γ= 1.14, the deposition rate clearly decreases as we increase the deposition time from 3 seconds to 120 seconds.

4.1.3 Controlling PECVD Depositions

Initial attempts at optimizing the deposition rate and refractive index successfully demonstrated the influence of the reactive gas flows (N_2O, SiH_4) along with the possible dependence on their ratio. However, it has also been observed that unlike the data reported in most publications, the ratio γ is not the only influential factor in silicon rich oxide depositions. Deposition time has a strong influence on the deposition rate. Furthermore, pressure and plasma power may also play a significant role. A complete model describing the sensitivity of the process to each of these parameters is therefore required.

4.2 Design of Experiments

Design of Experiments, or *Experimental Design*, is a rigorous and systematic tool based on statistical methods to select and organize the experimental trials to finally identify the effects of several input parameters on the desired response. It is a helpful method to obtain maximum information about a process influenced by several interacting parameters with a minimum number of experimental trials. Such a procedure is optimum for plasma enhanced chemical vapour deposition processes as the number of influential parameters and their interactions with each other are numerous, and not entirely well understood.

4.2.1 Introduction

Design of experiments was used to determine the key parameters of the deposition process and generate a model to evaluate their influence on the properties of the as-deposited silicon rich oxide film. SiH_4 gas flow, N_2O gas flow, pressure, power and deposition time have been used as the input parameters and the desired output was refractive index, thickness and deposition rate. Helium gas flow and distance between the electrodes were kept constant at 1900 sccm and 400 mils respectively. The rf frequency was 13.56 MHz. The expected outputs were measured experimentally using spectroscopic ellipsometry.

As a reminder, the average size and the density of the quantum dots formed in the layers is partially controlled by the thickness of the alternating bilayers and the excess silicon content in them. Ideally, the SRO film thickness should be less than 5 nm for quantum confinement, and the SiO_2 thickness should be less than 2 nm to ensure tunnelling conduction. Design of Experiments (DOE) was performed to achieve these conditions, while keeping an excess of silicon in the oxide, corresponding to refractive index $n \geq 2$ at 633 nm.

4.2.2 Description of the Experimental Design

A *factorial plan* allows variation of the input factors at two levels, i.e. a low level minimum and a high level maximum. For the five input parameters used in this design,

a high number of experimental trials are required with a factorial plan. As one of our aims was to limit the number of experimental trials, a *D-optimal (point exchange)* experimental design was used with a complete quadratic model to identify the most influential effects and their interactions. This design was generated using the *Design Expert* software, with a total of 27 experimental points.

D-optimal plans are used for factorial and screening designs where the most vital variables need to be identified. The *point exchange algorithm* uses a random design representing the model of the appropriate size created from the candidate (or experimental) points. Additionally, one of the candidate points was repeated to determine the reproducibility of the process. The input parameters and their range have been listed in Table 4.1. Details on the experimental candidate points have been listed in Appendix B.

Factor	Parameter	Units	Minimum	Maximum
A	N_2O gas flow	sccm	16.00	48.00
B	SiH_4 gas flow	sccm	6.00	24.00
C	Pressure	Torr	3.00	9.00
D	Power	Watts	50.00	114.00
E	Deposition time	sec	3.00	10.00
-	He gas flow	sccm	1900	-
-	Distance between electrodes	mils	400	-

Table 4.1: Different factors (A-E) varied in the D-optimal Design of Experiments along with their maximum and minimum values.

Description of the Model

The model used to describe the results of the Design of Experiments was a *complete-quadratic*, where the terms can be described by the following quadratic equation:

$$R = \underbrace{\alpha_0}_{\text{constant}} + \underbrace{\sum_{j=1}^{d} \alpha_j X_j}_{\text{linear terms}} + \underbrace{\sum_{j=1}^{\substack{k=d \\ j=d-1}} \sum_{\substack{k=j+1}} \alpha_{jk} X_j X_k}_{\text{interactions}} + \underbrace{\sum_{j=1}^{d} \alpha_{jj} X_j^2}_{\text{quadratic terms}} \tag{4.1}$$

Terms in the equation are therefore the linear terms *A, B, C, D, E*; interactions *AB, AC, AD, AE, BC, BD, BE, CD, CE, DE*; and quadratic terms A^2, B^2, C^2, D^2, E^2 with the corresponding coefficients represented by α. A, B, C, D and E have been described in Table 4.1. The presence of each of these terms is not compulsory for the final model and a combination of only the most significant terms was selected after an initial analysis with the *Design Expert* software.

4.2.3 Results of the Experimental Design

Before discussing the results of the design of experiments, it is important to note that spectroscopic ellipsometry is generally not used to simultaneously determine the thickness and refractive index of such ultra-thin oxide layers. Often, the optical indices are measured from thicker films and kept fixed, and subsequently the ultra-thin films are fitted for thickness. However, we tried to simultaneously measure both refractive index and thickness with ellipsometry, which inevitably led to unavoidable errors in the precision and accuracy of measurements.

For the results of the experimental design, the Sobol indices were evaluated which indicate the variance of the result variables caused due to a single input variable or its various combinations. The *Sobol variance analysis* thus allows a ranking of the different parameters in terms of sensitivity to the final deposition, and therefore analyse their influence on the deposition process (Figure 4.5).

Thickness

The thickness of the deposited films varied from 2.8±0.5 nm to 15.3±0.8 nm. A quadratic model used to describe the thickness is mentioned in Appendix B. However, quite obviously and as seen from Figure 4.5, the thickness has a strong dependence on the deposition time which varied between 3 and 10 seconds. To overcome this and see the real influence of the other parameters on the thickness of the film, the values for deposition rate were also fitted.

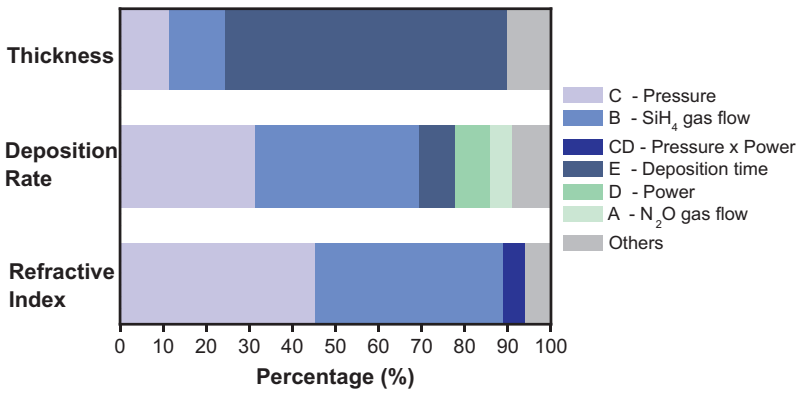

Figure 4.5: Percentage influence of each deposition parameter on the film properties. The most influential factors for thickness (C, B and E), deposition rate (BC, B^2, BD, AB, CD) and refractive index (AD, D, A) can be seen, with a strong influence of pressure (C) and SiH_4 (B) gas flow in all cases. A, B, C, D and E have been described in Table 4.1.

Deposition Rate

In the variance analysis for deposition rate in (Figure 4.5), a high sensitivity to SiH_4 gas flow and pressure is observed. An important albeit lower sensitivity to deposition time, plasma power and N_2O gas flow is also observed, and a coherent quadratic model describing the deposition rate has been mentioned in Appendix B.

The sensitivity of deposition rate to the deposition time may be due to the low deposition times (3-10 seconds) used in this experimental design. Plasma stabilisation occurs with higher deposition times, therefore influencing the deposition condition of the film for a time of 3 seconds.

Refractive index

The refractive indices were fitted using spectroscopic ellipsometry models. However, as described earlier, the error in the values is possibly too high as the technique is not completely adapted to the measurement of both refractive index and thickness of such ultra-thin films.

The *lack of fit* from the quadratic models in the Design Expert software was ob-

served to be significant. This means that the quadratic model doesn't correctly apply to the results obtained and failed to give any coherent results. Furthermore, the use of the ratio $\gamma = N_2O/SiH_4$ as an additional parameter in the model (which supposedly has a strong influence on the refractive index of the film) did not facilitate the analysis.

As the refractive index relation is clearly not satisfied by a quadratic model, a *Spline meta-model* was used to calculate the influence of the various parameters on the refractive index. Splines are often used when polynomial models fail. They can estimate the response surface over the entire experimental region of the problem. A spline response showing the best fits was selected with only four variables, with deposition time and gas ratios excluded as they did not seem to influence the outputs. The most influential parameters were SiH_4 gas flow and pressure along with the interactions of N_2O gas flow-plasma power and pressure-plasma power(Figure 4.5).

Desirability Analysis

The uncertainty from refractive index measurements must be emphasized as it doesn't allow complete confidence in these models, even if they show the best fits. 5000 values of the different parameters were generated according to the refractive index spline models and corresponding deposition rate and thickness were calculated using the equations generated by the quadratic model (with deposition time = 3 sec). These equations are mentioned in Appendix B. As two separate models have been used for thickness and deposition rate, only those cases were considered where for the fixed deposition time of 3 seconds, the following relation is valid:

$$Deposition\,Rate \times Deposition\,Time = Thickness \pm 10\% \tag{4.2}$$

A desirability analysis (Figure 4.6) was used to filter out the desired values in terms of these 3 parameters. The desirability factors for thickness ($d1$), deposition rate ($d2$) and the refractive indices ($d3$) have been shown in Figure 4.6.

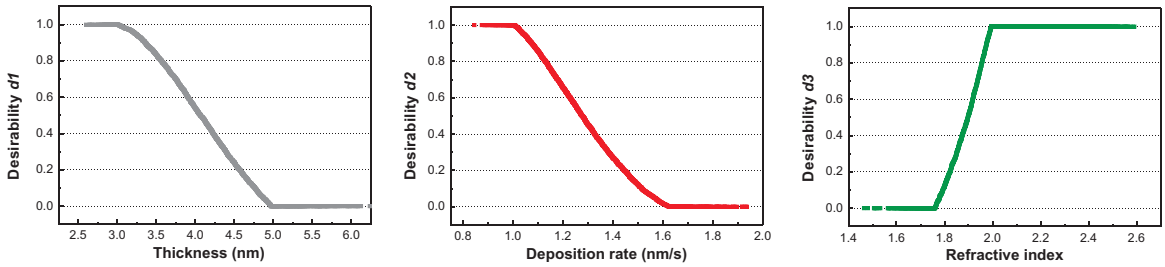

(a) (b) (c)

Figure 4.6: Desirability values assigned for (a) thickness, (b) deposition rate, and (c) refractive index.

Only the cases with total desirability $D > 0.67$ were considered where, the D is described by:

$$D = d1 \times d2 \times d3 \tag{4.3}$$

Finally, for the cases where the total desirability was more than 0.67, deposition rate and refractive index were plotted versus SiH_4 gas flow and pressure in Figure 4.7. Additionally, in spite of its exclusion from the quadratic and spline models used, the gas ratio $\gamma = N_2O/SiH_4$ was plotted in Figure 4.8, to see if it indeed does influence the as-deposited silicon rich oxide.

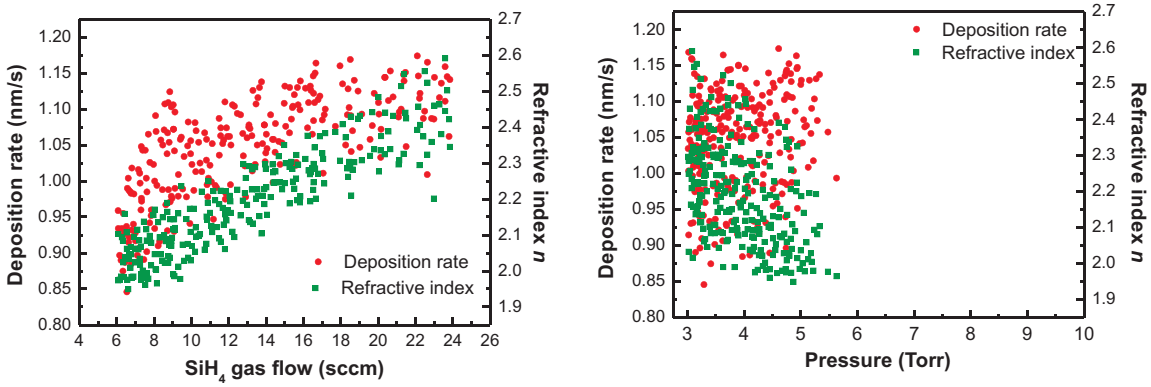

(a) (b)

Figure 4.7: Influence of SiH_4 and chamber pressure on PECVD. (a) Within the experimental design range, increasing SiH_4 flow increases both deposition rate and refractive index. (b) While the pressure was varied from 3 Torrs to 9 Torrs in the design, only those cases show appropriate desirability where the pressure is lower than 5.5 Torrs.

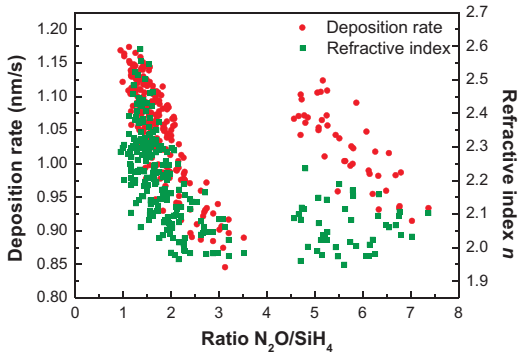

Figure 4.8: Influence of the ratio γ on the deposition rate and refractive index may be misleading, as the models clearly indicate a strong influence of only SiH_4.

Discussion

From the results of the design of experiments and the desirability analysis, we can define certain conditions for ultra-thin depositions for silicon rich oxides, with a strong control over the thickness and silicon enrichment (refractive index). The most influential parameters are *pressure* and *silane gas flow*. The deposition rate and refractive index are both observed to increase with increasing SiH_4 flow. The refractive index is higher for a higher quantity of silicon in the films. Interestingly, lower pressures are required for optimum deposition rates and refractive indices as no desirable experimental points were obtained for pressure more than 5.5 Torrs (Figure 4.7b).

While the models demonstrate no influence of γ, Figure 4.8 indeed shows higher refractive indices and deposition rates for lower ratios ($1.4<\gamma<3.1$), along with some scattered points for higher values ($\gamma>4.5$). This might be misleading as probably only the silane content plays a major role under the right pressure conditions during deposition.

Our model gives a thorough picture of the influential parameters for deposition, unlike different models in literature which examine the influences of one or two factors independently.

4.3 Optimizing Annealing Conditions

After obtaining the optimum criteria for ideal deposition conditions, the annealing step needs to be optimized to obtain size-controlled luminescent quantum dots. For this, single-step rapid thermal annealing (RTA) was used. The advantages of using a rapid thermal process over a traditional annealing step have been reported where the RTA results in decreased FWHM of photoluminescence peaks[159] and helps in the initial nucleation of the nanostructures under limited diffusion conditions.[160] Using a single-step annealing instead of a two step nucleation-crystallization limits the number of steps, while additionally reducing the annealing ramp time for formation of the quantum dots. For the multiple bilayers, the deposition conditions chosen have been described below, in Table 4.2.

Material	**N_2O** **sccm**	**SiH_4** **sccm**	**He** **sccm**	γ	**Pressure** **Torr**	**Power** **Watt**	**Temperature** **°C**	**Distance** **mils**
SiO_x	16	14	1900	1.14	5.5	114	480	400
SiO_2	550	6	1900	91.67	5.5	114	480	400

Table 4.2: Samples used for characterizations of multi-layer structures.

Ten alternating bilayers were deposited using a single deposition sequence, without removing the wafers from the PECVD reactor.

4.3.1 Structural Characterizations of Different Annealed Films

RTA annealing under N_2 was performed at 3 temperatures - 1000°C, 1050°C and 1100°C each for 5, 20 and 60 minutes. A defect passivation annealing step was performed under forming gas for 30 min at 425°C. Additionally a non-annealed sample was taken as reference. Using spectroscopic ellipsometry, the thickness of the silicon rich oxide layer was determined to be 3.1±0.5 nm and SiO_2 as 1.5±0.3 nm.

FTIR

The FTIR peak at 1042 nm^{-1} for the as-deposited film gives the stoichiometry of the silicon rich oxide, with $SiO_{x=1.54}$, and silicon atomic excess at 29%. On annealing, this peak is observed to shift towards that of stoichiometric SiO_2 (Figure 4.9a and b). This shift can be attributed to the phase separation of Si and SiO_2, and to increasing quantities of silicon nanoclusters surrounded by stoichiometric SiO_2 as the annealing temperature and annealing time increase.

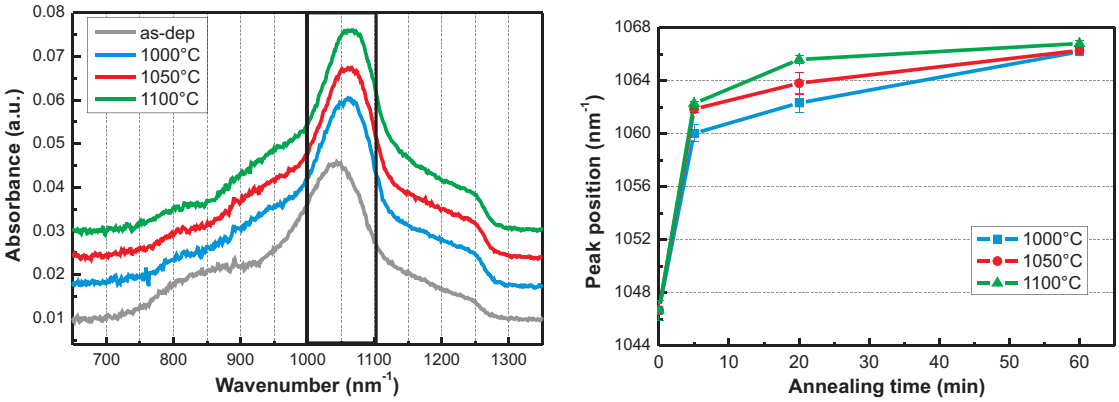

(a) (b)

Figure 4.9: FTIR for multilayer samples. (a) The Si-O stretching peak shifts from the as-deposited film (1042 cm^{-1}) to higher values for 60 min annealing time. (b) shows the shift of this peak position with time and temperature.

4.3.2 Influence of Annealing Conditions on Photoluminescence

Photoluminescence is extremely important for observing quantum dot properties and the intensity of the peak may depend strongly on the annealing conditions.[161] Using a combination of photoluminescence and EELS analysis, Iacona[162] and Daldosso[116] have reported the formation of amorphous silicon clusters starting from a temperature of 1000°C, which turn into crystalline quantum dots from 1100°C. Additionally, Lopez et al[22] reported no increase in quantum dot size between annealing at 1100°C for 1 min or 16 hours. However, they reported an increase in the photoluminescence peak intensity which saturates only after 3 hours, as well as the importance of a passivation annealing under forming gas.

The size of the quantum dots is limited by the thickness of the silicon rich oxide (3 nm). They should ideally demonstrate strong confinement due to the presence of the surrounding SiO_2 matrix in multilayers. The photoluminescence signal is expected to originate largely from the dots even if Si-O interface defects add on to the luminescence.

Comparing the room temperature photoluminescence on excitation at 355 nm, a strong photoluminescence signal was observed for the sample annealed at 1100°C 1h (Figure 4.10). It was indeed seen that the photoluminescence intensity only begins to increase at 1100°C, the minimum temperature required for formation of silicon nanocrystallites.[162]

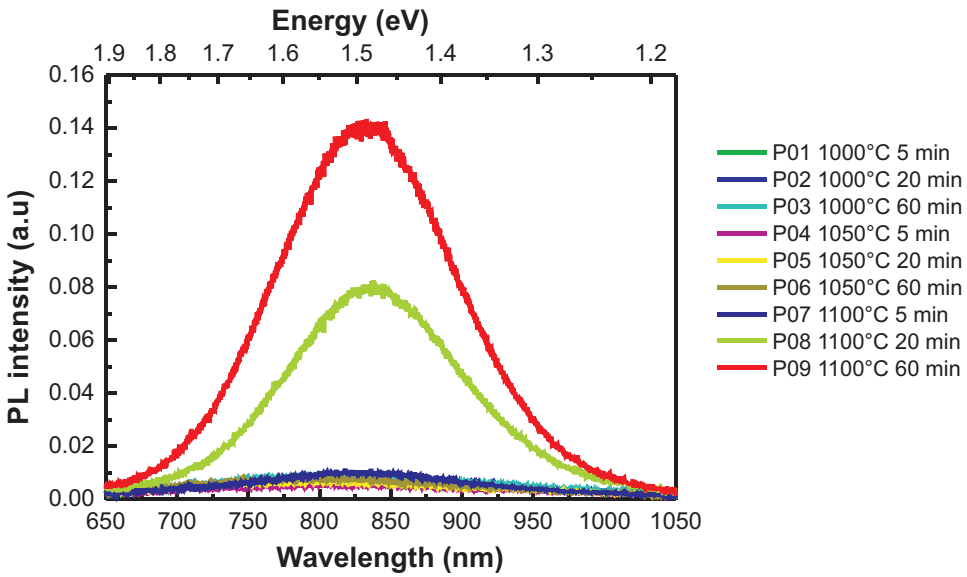

Figure 4.10: Photoluminescence of multilayer samples for different annealing conditions. The intensity of the PL peak increases substantially for the multilayers annealed at 1100°C, with maximum at 60 minutes annealing.

As the annealing time increases, this signal increases very strongly. Less time and lower temperatures are probably insufficient for silicon nanocluster formation, and the weak photoluminescence signals can be attributed to partially amorphous Si nanoclusters. The change in intensity becomes more evident on comparing the intensities of the photoluminescence peaks in Figure 4.11.

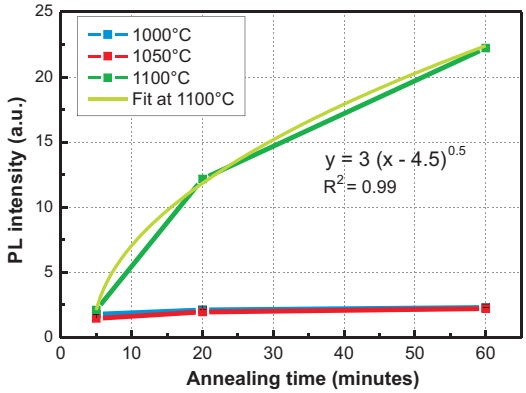

Figure 4.11: Comparison of photoluminescence intensities for different annealing times. The intensity increases substantially with annealing time at 1100°C.

The change in intensity with time for samples annealed at 1100°C can be fitted with a $\sqrt{time}$ relation that is given as follows, where $t_{minutes}$ is the annealing time in minutes.

$$PL\ intensity = 3\sqrt{t_{minutes} - 4.5} \tag{4.4}$$

The diffusion length of a material in a solid is known to be a function of $\sqrt{time}$. A similar observation in the relation arising from the intensity of the luminescent centres in the film indicates the presence of diffusion related phenomena in the SiO_x layers.

4.3.3 Energy Filtered Transmission Electron Microscopy (EFTEM)

Plan-view EFTEM micrographs with plasmon excitation at 16 eV (with silicon in bright zones) were compared for observing the presence of silicon quantum dots in the films annealed at 1100°C (Figure 4.12). At 1000°C, silicon is visible in the silicon rich oxide layers, but without any observable separation into clusters and silicon crystallites are not observed in the layers. At 1050°C, a small separation begins to emerge and clearly separated silicon quantum dots are observed at 1100°C, along with their crystalline planes. This corresponds well with the results from the photoluminescence data. The thickness of the silicon rich oxide with nanocrystals and silicon dioxide are confirmed to be ∼3 nm and ∼1.5 nm respectively. A plan-view micrograph (Figure 4.13) additionally shows a high density of silicon quantum dots, observed at 16 eV (silicon in bright zones) as well as 24.4 eV (silicon in dark zones).

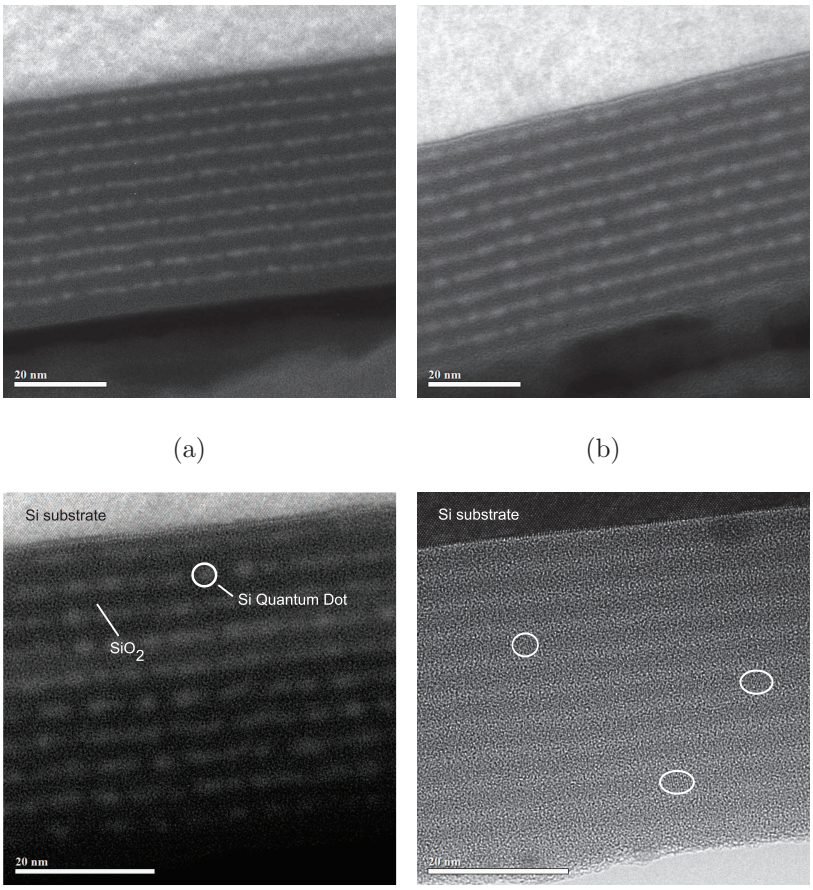

Figure 4.12: Cross-section TEM micrographs of samples annealed for 60 minutes at (a) 1000°C, (b) 1050°C and (c) 1100°C with plasmon energy loss at 16 eV, showing silicon in bright zones. Small separated crystallites can be observed for 1100°C in (d) which is the corresponding micrograph without plasmon excitation.

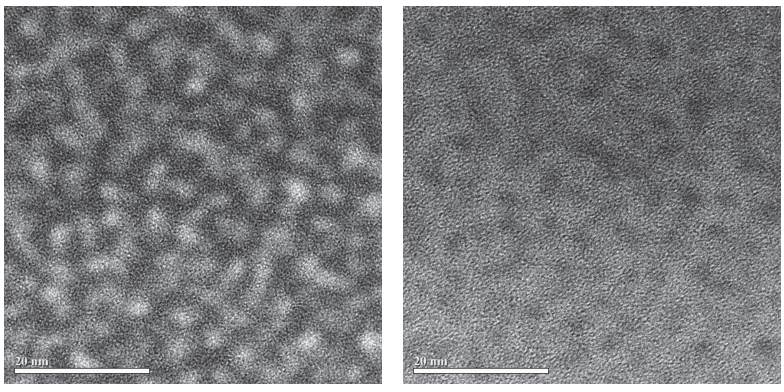

Figure 4.13: Plan-view EFTEM at (a) 16 eV and (b) 24.4 eV for sample annealed at 1100°C (60 minutes) showing a high density of Si quantum dots with ∼3 nm diameter.

4.4 Photoluminescence Studies of the Multilayer Structure

Other factors were varied during the deposition process to examine their influence on the formation of the quantum dots and consequently on the final photoluminescence. This was under the assumption that the Si nanocrystals contribute significantly to the photoluminescence signal, and that it does not originate solely from Si-O defect states, which have already been passivated.

The deposition time for the SRO was 6 seconds, corresponding to a thickness of $\sim$ 5.9 nm. All samples were annealed at 1100°C for 60 minutes followed by a forming gas anneal for passivation. In this section, the photoluminescence signals for 10 bilayer samples have been compared.

4.4.1 Varying SiO_2 Thickness

We observed in the previous chapter that the thickness of a single silicon rich oxide film plays a major role in the formation and arrangement of silicon quantum dots in its oxide matrix. To observe any influence of SiO_2 on dot formation in the case of bilayer structures the deposition time of the silicon dioxide was increased. Any change in the dioxide thickness should not affect the quantum dots formed in the silicon rich oxide layer, as the Si diffusion and phase separation occur only in this non-stoichiometric oxide.

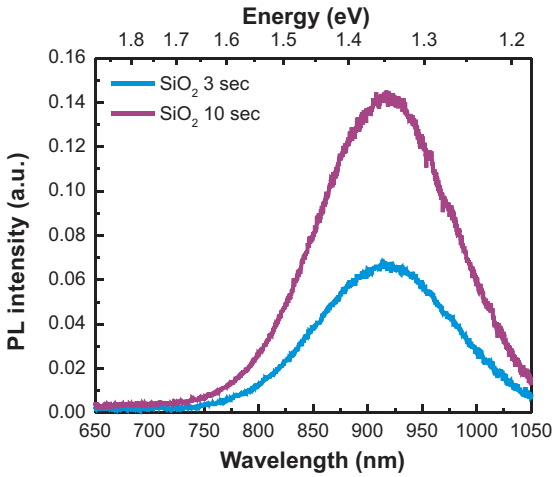

Figure 4.14: Increasing SiO_2 thickness from 1.5 nm to 5 nm more than doubles the photoluminescence peak intensity.

However, as seen in Figure 4.14, the photoluminescence signal was observed to more than double up in intensity as the SiO_2 thickness was increased from 1.5 nm to 5 nm. This demonstrates that SiO_2 indeed affects the silicon nanocrystal formation. Similar phenomena have previously been observed on the crystallinity of the silicon quantum dots in the case of a Si_3N_4 matrix by Scardera et al.[163]

4.4.2 Comparison with Thick Single Layer

In Chapter 2 for thick single layers, broad photoluminescence peaks (and a consequent large quantum dot size distribution) were observed for singly deposited layers which was one of the motivations behind optimizing multilayer depositions. To verify controlled quantum dot formation in multilayer samples the photoluminescence spectra of multiple bilayers (total thickness 85 nm) and single layers (thickness 75 nm) have been compared in Figure 4.15. It is clear that while quantum dots are present in single layers, the size distribution is fairly large and comparable to that observed in similar films of Chapter 2.

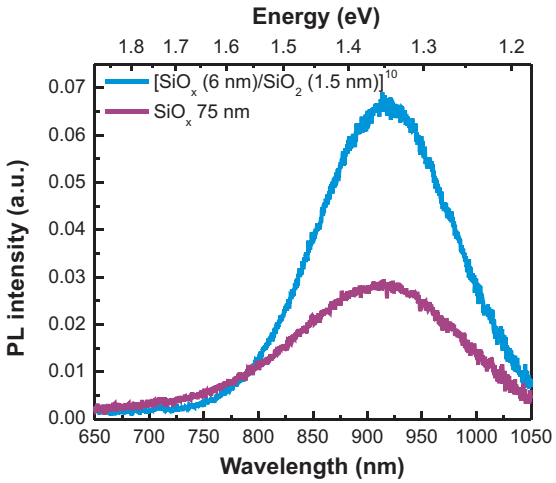

Figure 4.15: The photoluminescence intensity in multiple bilayer structures is much higher than that in a single layer.

The lower photoluminescence intensity can be attributed to the properties of the rest of the film as the environment within the film can influence dot formation. Other factors contributing to lower photoluminescence intensity are the broad size distribution of dots and possible lower quantum confinement in single layer structures.

4.4.3 Varying Number of Multilayer Stacks

The hypothesis that the silicon nanocrystals formed depend only on the thickness of the silicon rich oxide cannot be entirely true as on doubling the number of bilayers (i.e. from 10 to 20 stacks), the photoluminescence signal doesn't double up, but rather increases by a factor of 5 (Figure 4.16). This again confirms the influence of external parameters in the formation of quantum dots.

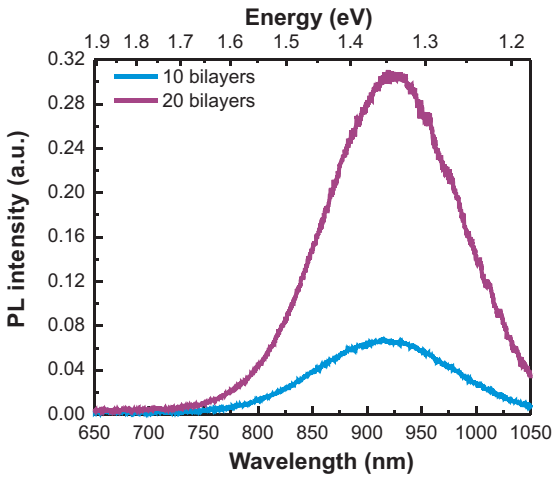

Figure 4.16: Doubling up the number of bilayers from 10 to 20 increases the photoluminescence intensity by a factor of 5.

4.4.4 Discussion

The differences in photoluminescence properties of these different films can be explained by variations in film structure. For example, a detailed study by Zacharias et al[114,118] indicates the importance of stacking faults or twinning that can influence x-ray interpretation of silicon nanocrystals in an amorphous silicon matrix. This discussion can be extended towards silicon quantum dots in SiO_2 as the presence of dislocations and growth faults has already been demonstrated in Chapter 3. Indeed, embedded nanocrystals show inhomogeneous strain that depends on thickness of the multilayers and the annealing temperature, along with the silicon enrichment.

For thinner layers, the strain was observed to decrease by one order of magnitude in a-Si/SiO_2 bilayer structures. Zacharias has attributed the origin of this strain to a

combination of one or more of the following:

- Increasing surface/volume ratio with decreasing nanocrystal size, leading to intrinsic strain from bond angle deviations.
- Differences in thermal expansion coefficients of Si, SiO_2 and also the silicon rich oxide layer.
- Volume shrinkage as we go from amorphous to crystalline materials.
- Strain from dislocations and growth faults.

The structural properties of the films may therefore be different as the multilayer thickness and interfaces can affect the crystallization temperature, which increases exponentially for thinner films, changing the nature of the dots from amorphous to crystalline.[118] Other factors influencing photoluminescence intensity include the differences in total film thickness of different samples, which can indeed change the quantity of luminescent clusters. Furthermore, differences in quantum confinement of the dots and the quantity of crystalline and amorphous silicon can influence the photoluminescence.

The influence of this strain in the quantum dot properties, along with presence of small quantities of amorphous silicon is not completely understood. This is the potential reason behind the differences in photoluminescence in the films. Furthermore, it is important to note that none of the multilayer films showed diffraction peaks when characterized with grazing incidence x-ray diffraction, reaffirming the importance and influence of the strain which has significant consequences on dot formation.

4.5 Summary and Conclusions

The deposition and annealing conditions play a significant role in the fabrication of size-controlled luminescent silicon quantum dots. For as-deposited films, contrary to what has been mostly published, we observed little dependence of the refractive index on the gas flow ratio, and a strong dependence of both the refractive index and deposition rate on the PECVD chamber pressure and SiH_4 gas flow. A complete model was

established for PECVD depositions, with simultaneous and precise control over silicon enrichment (refractive index) and ultra-thin layer thicknesses (SiO_x ∼3 nm and SiO_2 ∼1.5 nm). Crystalline and luminescent silicon quantum dots were fabricated. It was observed that a minimum temperature of 1100°C is required for formation of luminescent dots, and an annealing time of 60 minutes significantly increases emission.

However, the thickness of the silicon rich oxide layers and annealing conditions are not the only factors affecting the luminescence and the formation of the silicon dots in the SiO_2 matrix. Altering the number of multiple bilayers and changing SiO_2 thickness can affect the properties of the nanocrystals formed. This can be attributed to strain in the films arising from structural defects, which affects the structural properties of the dots. The amorphous and crystalline content, overall thickness and quantum confinement of the Si dots and luminescent defects can affect the photoluminescence intensity. Nevertheless, it is possible to form size controlled quantum dots with tunable bandgaps as will be discussed in the following chapter.

Chapter 5

Electrical and Optical Properties of Single Layers and Multiple Bilayers

5.1 Introduction

This chapter deals with the electrical and optical properties of multiple bilayer films developed in Chapter 4. Electrical conduction properties and carrier transport phenomena are compared with single layer structures, followed by a brief discussion of the response under illumination. Multilayer films were fabricated to have optimized control over quantum dot size and inter-dot distance, to consequently control the bandgap and electrical conductivity respectively.

5.2 Device Materials

5.2.1 Bandgap Optimization in the Active Layer

Different film thicknesses for the silicon rich oxide were used in 10 bilayer structures for optimizing the bandgap of the quantum dots. The silicon rich oxide thickness was varied from 3 nm to 8 nm. The thickness of SiO_2 was kept constant at 1.5 nm. These were compared with a single thick film of 75 nm using photoluminescence spectroscopy. The material properties of the silicon rich oxide and the annealing conditions used were identical to those used in Chapter 4.

The photoluminescence peak position of the these multilayer films is likely to vary

due to the effect of quantum confinement on the bandgap, which blue-shifts as the quantum dot size decreases. As the layer thickness increases from 3 nm to 8 nm, the bandgap should decrease from 1.73 eV to 1.25 eV respectively, calculated using the relation by Niquet et al.[16] Normalised photoluminescence spectra for these multilayers are shown in Figure 5.1. Photoluminescence of a thick single layer structure has been included for comparison.

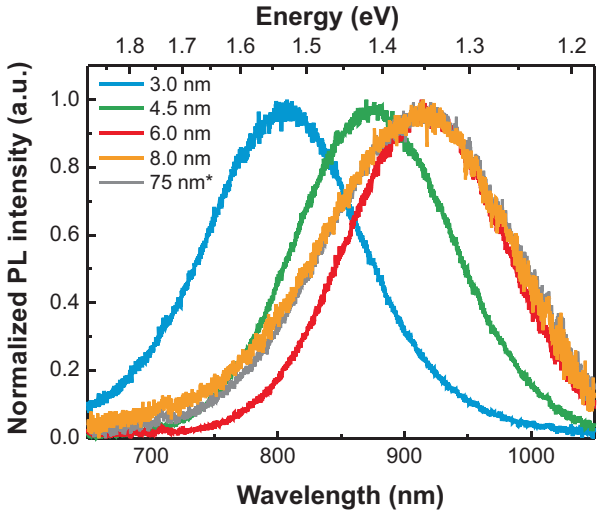

Figure 5.1: Photoluminescence as it varies with thickness of the as-deposited SRO layer in multilayers, showing a blue-shift for smaller dots.

From Figure 5.1, it can be inferred that photoluminescence peak position, related to the bandgap, depends on the quantum dot size, which does indeed depend on the thickness of the silicon rich oxide layer. The blue shift is clearly evident for 3 nm SiO_x layers. This is consistent with the known fact that the maximum diameter of the dots is the thickness of this SiO_x layer.[104] Silicon quantum dots are formed as the excess silicon diffuses through the non-stoichiometric layers, limiting the dot size by the thickness of the layers.

Thicker SiO_x layers therefore form larger quantum dots. However, larger dots have weaker quantum confinement. Therefore as the thickness of the SiO_x layer increases beyond 6 nm, the bandgap change is not significant. In addition, thicker SiO_x layers demonstrate a broader photoluminescence peak undoubtedly due to the presence of

smaller dots that have not grown to the maximum thickness of the layer. The photoluminescence spectrum of the 8 nm SRO film being almost identical to the 75 nm single layer spectrum affirms this assumption.

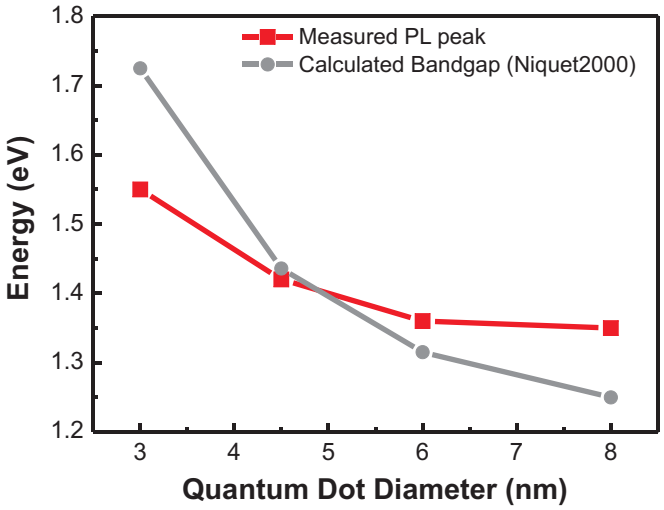

Figure 5.2: Experimental and calculated luminescence peak positions and quantum dot size. The calculated values are from Niquet et al.[16]

As we compare the observed photoluminescence peak values with the theoretical bandgap calculations of Niquet et al[16] in Figure 5.2, a similar trend is observed in spite of large variations in actual values. The dot diameter was assumed to be equal to the thickness of the silicon rich oxide layer. The differences in experimental and calculated values can be attributed to differences in the size and crystallinity of the dots and the variations in interface defects.[26] Furthermore, it is known that thinner layers require higher annealing temperatures for Si recrystallization.[114,118] The annealing temperature also affects silicon dot interfaces and surface states[164] which alter the photoluminescence signal. Exciton binding energy affects photoluminescence and increases for smaller quantum dots. The contributions from each of these effects are difficult to separate out from quantum confinement.

5.2.2 Electrode and Substrate Materials

For comparing electrical conduction phenomena in silicon quantum dot layers, different electrode and substrate materials were used to ensure that the consequent electrical results do indeed characterize the quantum dot layers. They should not be a characteristic of the metal-semiconductor junction formed between the contact metal and the silicon substrate. The work function difference between the electrodes and substrate can affect the type of metal-semiconductor contact formed.

Aluminium and polycrystalline silicon

Degenerate n-type substrates (arsenic doped) were used with resistivity less than 3.5 mΩ cm with aluminium and polycrystalline silicon electrodes. Aluminium, with a work function of 4.08 eV is a commonly used material for IC fabrication. For conventional Al-Oxide-Si junctions, flat band voltages are known to be around -0.82 to -1.08 V for p-type silicon and can further change with the dopant concentration. A Schottky junction with rectifying characteristics is hence formed. The device needs to be specifically designed for ohmic contacts to avoid unwanted characterization of junction properties. Figure 5.3 shows a schematic of the capacitors used for p-i-n type devices with Aluminium or polycrystalline electrodes.

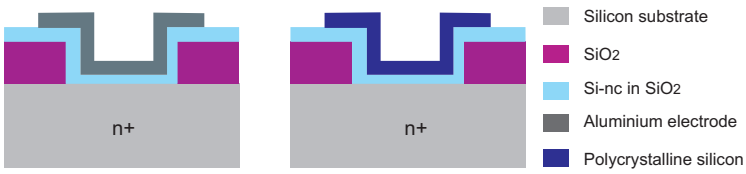

Figure 5.3: p-i-n type devices with Al or polysilicon (boron doped) electrodes.

Polycrystalline silicon comprises of small single crystal grains of silicon separated by thin grain boundaries. These different crystal orientations meet at the grain boundaries creating dangling bonds. The size and quantity of the grains determines the conductivity. On doping this polycrystalline silicon, the dangling bonds are rendered electrically inactive, and they create a barrier which allows conduction through thermionic emission or tunnelling.[165] After its introduction by Faggin,[166,167] polycrystalline Si has aided in

reduction in dimensions for MOS technologies, while simultaneously providing faster circuits with lower power consumption and higher reliability. For polycrystalline silicon devices, the resulting threshold is far less negative than that for aluminium although it still depends on the doping levels.

Boron doped polysilicon film with dopant concentration of 10^{21} atoms/cm^3 and resistivity of 3.85 mΩ cm was deposited using epitaxial silicon from silane at 650°C in *Applied Materials Endura 5500*.

Transparent Conducting Oxide

Aluminium and polycrystalline silicon have the disadvantage of being thick opaque electrodes which do not allow the passage of light. To overcome this drawback and measure the light dependent electrical conduction properties, *transparent conducting oxides* (TCOs) can be used. These TCOs combine optical transparency and good electrical conduction properties to form a suitable replacement electrode.[168,169] In this work, ITO or Indium-doped Tin Oxide (SnO_2) (In_2O_3 90%, SnO_2 10%) has been used as an n-type degenerate semiconductor with p-type degenerate substrates to form an n-i-p type device with quantum dots as the intermediate material. Figure 5.4 shows a schematic of the capacitors used for n-i-p type devices with transparent ITO electrodes.

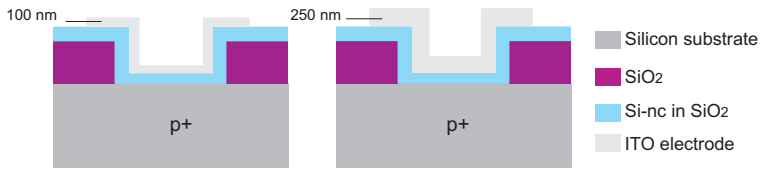

Figure 5.4: n-i-p devices with ITO thickness 100 nm and 250 nm, allowing passage of more than 80% of light through the substrate.

ITO has a work function commonly reported to be 4.7 eV (but it may vary from 4.1 to 5.53 eV). It allows transmission of more than 80% of light (Figure 5.5) and has conductivities high enough for efficient carrier transport. 100 nm and 250 nm ITO layers were deposited using physical vapour deposition (sputtering) on *Applied Materials Centura 5500*, followed by annealing under N_2 for 300°C. The resistivity of ITO was 252.3 $\mu\Omega$

cm and of the p-type substrates was 0.01-0.02 Ω cm.

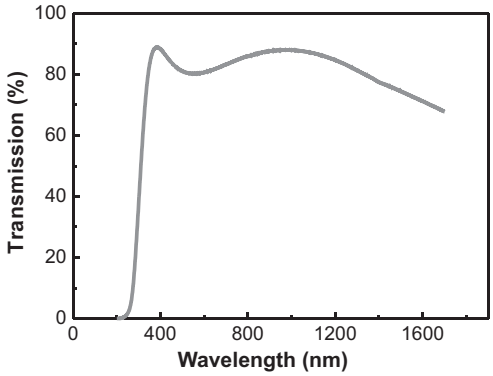

Figure 5.5: Light transmission in ITO versus wavelength.

Samples prepared for characterization

Samples of the lot *T807P* first characterized on full-sheet wafers for photoluminescence were then prepared for electrical characterizations and have been listed in Table 5.1. Three multiple bilayer structures were prepared along with a thicker single layer film for comparison.

Thickness	Al	polycrystalline Si	ITO 100 nm	ITO 250 nm
$(3nm\text{-}1.5nm)^{10}$	T03-Al	T03-poly	T03-ITO100	T03-ITO250
$(4nm\text{-}1.5nm)^{10}$	T04-Al	T04-poly	T04-ITO100	T04-ITO250
$(6nm\text{-}1.5nm)^{10}$	T06-Al	T06-poly	T06-ITO100	T06-ITO250
75 nm	T75-Al	T75-poly	T75-ITO100	T75-ITO250

Table 5.1: Multilayer samples (with 10 bilayers) and a thick single layer sample used for electrical characterizations with different electrode materials.

5.3 Electrical Conduction in Multilayers

Current-voltage measurements can give an insight into current densities in the films, along with the associated electrical conduction phenomena. These electrical measurements therefore permit a comparative analysis between the different active layer structures, i.e. the multilayers with quantum dots of different bandgaps, and a single thick layer structure.

The current-voltage measurements were performed for 49 different chips of area 2.56 mm^2 each, and averaged over the entire wafer. The sweep direction used was -15 V to +15 V. Current-voltage curves are shown in (Figure 5.6) for the four different electrode configurations (Al, poly Si, ITO 100 nm, ITO 250 nm) in each of the silicon quantum dot films.

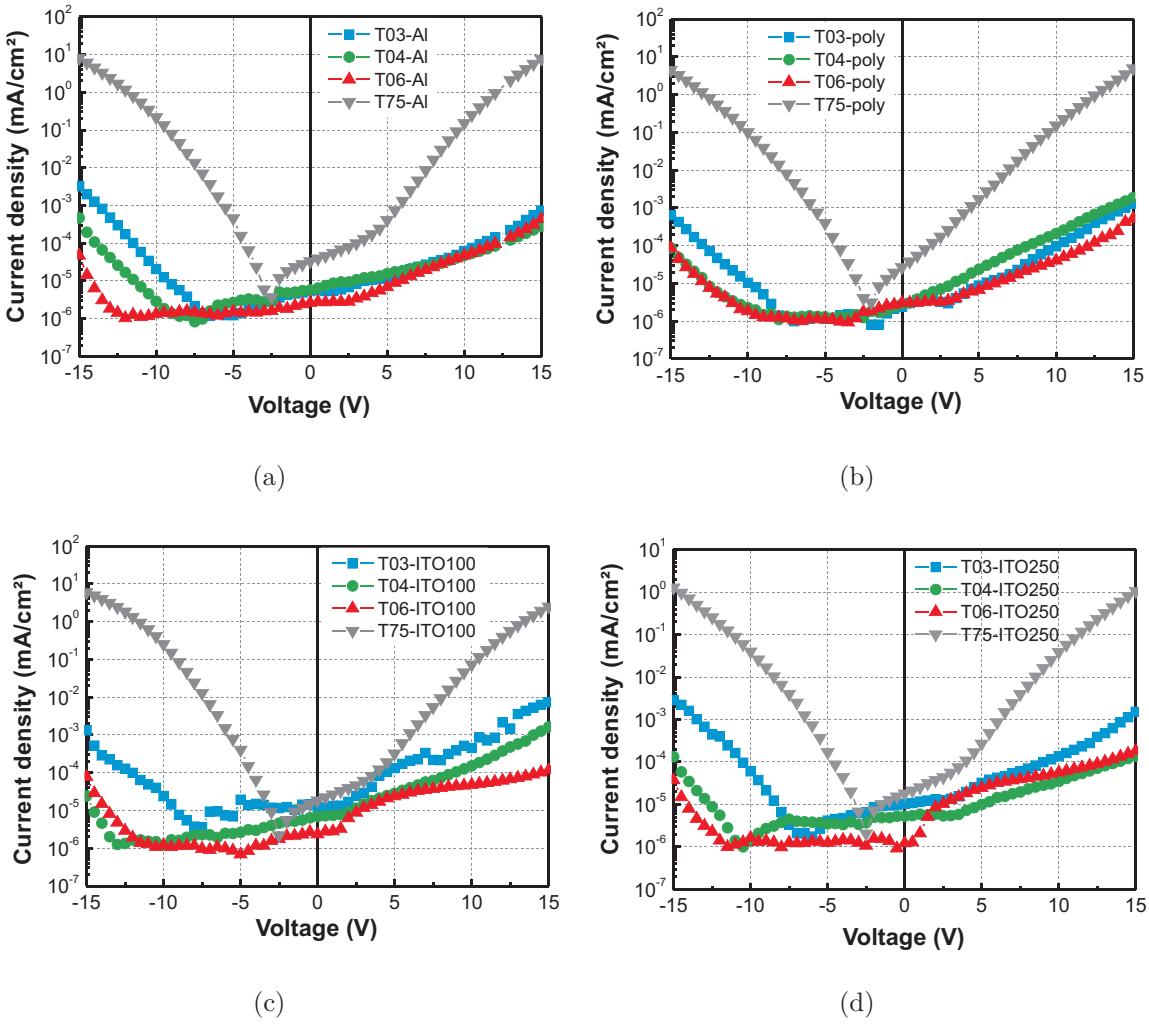

Figure 5.6: Current versus voltage characteristics for different electrode materials - (a) Al, (b) polycrystalline Si, (c) ITO - 100 nm and (d) ITO 250 nm.

The different silicon quantum dot films show similar behaviour in the case of all four electrodes. These measurements ensure that the results of the current-voltage experiments are solely due to the film and not due to the nature of the metal-semiconductor junction

contact. Additionally, the current density is observed to be significantly stronger in the case of the single layer T75 sample, irrespective of the electrode used. This is followed by the T03 (3 nm bilayer). The rest of the multilayer samples conduct even less, and will therefore not be used for further electrical characterizations. Figure 5.7 shows the current densities for samples T03 and T75 for different electrode materials. Similar results further ensure that the silicon quantum dot layer has been characterized and not the metal-semiconductor junction.

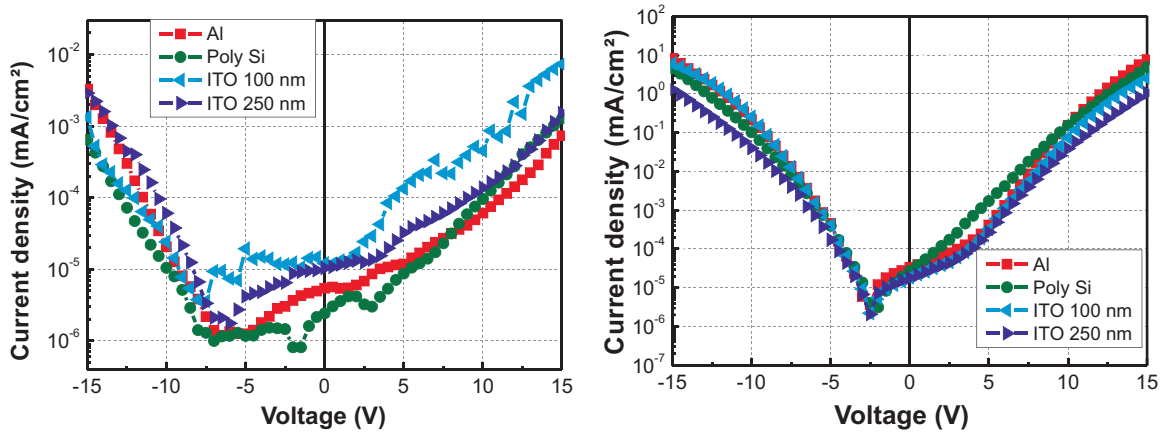

Figure 5.7: I-V characteristics of (a) Multilayer structures (3 nm SRO + 1.5 nm SiO_2)[10] and (b) 75 nm thick SRO single layer structures.

The large differences in the conductivities of the thick single layer and multilayer films will be studied by low temperature conductivity measurements in the next section.

Hysteresis and Charge Trapping

An interesting phenomenon observed in all samples is the non-zero current present at 0 V, during the measurement sweep (-15 to 15 V). The reverse sweep (+15 to -15 V) demonstrates a hysteresis effect, shown in Figure 5.8 for sample T75-poly. The current minima occur at ± 2.5 V, depending on the direction of the scan, forming a hysteresis of width of around 5 V around 0 V. Similar results have been observed by Hossain et al.[170] The observed hysteresis can be attributed to trapping of charge carriers in the quantum dot layer thus creating a built-in potential which adds on to the external bias.

This built-in potential has different signs depending on the charge of the trapped species, hence leading to this hysteresis.[170,171]

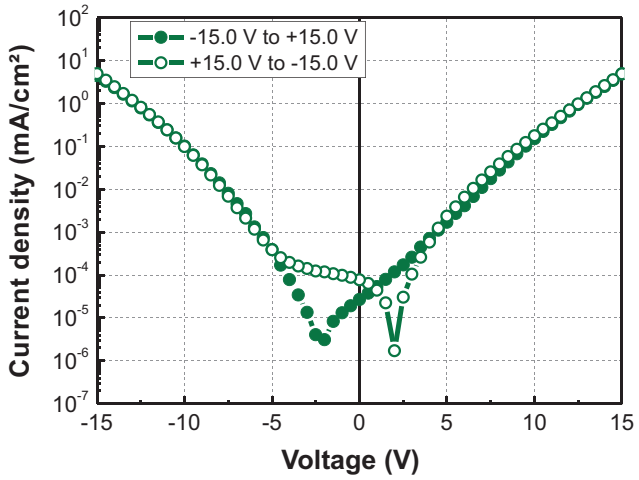

Figure 5.8: Current vs voltage characteristics show hysteresis for T75-poly sample.

For an insight into the origin of traps, in polycrystalline and amorphous semiconductors like these silicon quantum dots, a high density of defects is present due to grain boundaries between crystallites which are loaded with electron and hole traps. These defects also create potential walls and wells, preventing charge carrier flow and influencing electrical conduction.[172]

Furthermore, additional traps may be present even in the stoichiometric SiO_2. These include defects in the oxide layer (*oxide traps*), traps at the Si quantum dot-SiO_2 interface (*interface traps*) and other near-interfacial oxide traps (*border traps*), which lie within 3 nm of the oxide-substrate interface.[173,174] In the case of silicon dots in a single-step deposited layer, traps are present largely due to the large surface to volume ratio at the Si-SiO_2 interface. In the case of the silicon quantum dot multilayers, additional traps may be present at each bilayer interface in the oxide, and also on the surface due to the smaller size of the dots. These ultra-thin layers have higher strain and lattice defects which may further multiply charge trapping. Even though H-passivation post-annealing was performed and is known to passivate Si-O defects, its effectiveness on the other defect states is unclear.[164]

5.4 Low-Temperature Electrical Conductivity

Low temperature current-voltage measurements were carried out from 80 K to 300 K, at every 10 K for elucidation of the conduction mechanism and possible explanations of the differences in single and multilayer structures. In Chapter 3, electrical conductivity was observed to decrease with increasing film thickness for single deposited films. Here, it is indeed surprising that conductivity is still higher in single layers as compared to multilayer structures even though the inter-dot distance has been optimally controlled to be less than 2 nm.

Electrical Conductivity in Multilayers

For multilayer samples (T03-Al), conductivity appears to be temperature independent with less than a decade of conductivity increase between 80K and 300 K. This has been measured at low fields (±1 V, E = 0.21 MV/cm) as higher fields may alter conduction mechanisms. The temperature independence indicates a tunnelling conduction mechanism. This is further evident from Figure 5.9, which shows temperature change in current density (linear and log scale) vs voltage, and conductivity vs 1000/T Arrhenius plot.

At higher electric fields (±12 V, E = 2.5 MV/cm), a visible change in conduction mechanism is observed and will be discussed in the next section.

Electrical Conductivity in Thick Single Layers

Higher electrical conductivity is observed in thick single layer samples (T75-Al) at low fields (±1 V, E = 0.13 MV/cm). At T < 200 K, the conductivity is also apparently temperature independent. However, for T > 200 K, a transition in the temperature dependence is observed. This has also been mentioned in Chapter 3, and previously reported by Rafiq[145] and Yildiz,[149] who attribute it to the activation of thermionic emission. For these thick layer samples, the current nevertheless shows an increase of only less than a decade at low electric fields. The change in conduction mechanism at higher electric fields (±12 V, E = 1.6 MV/cm) is visible and will be explained in the next section.

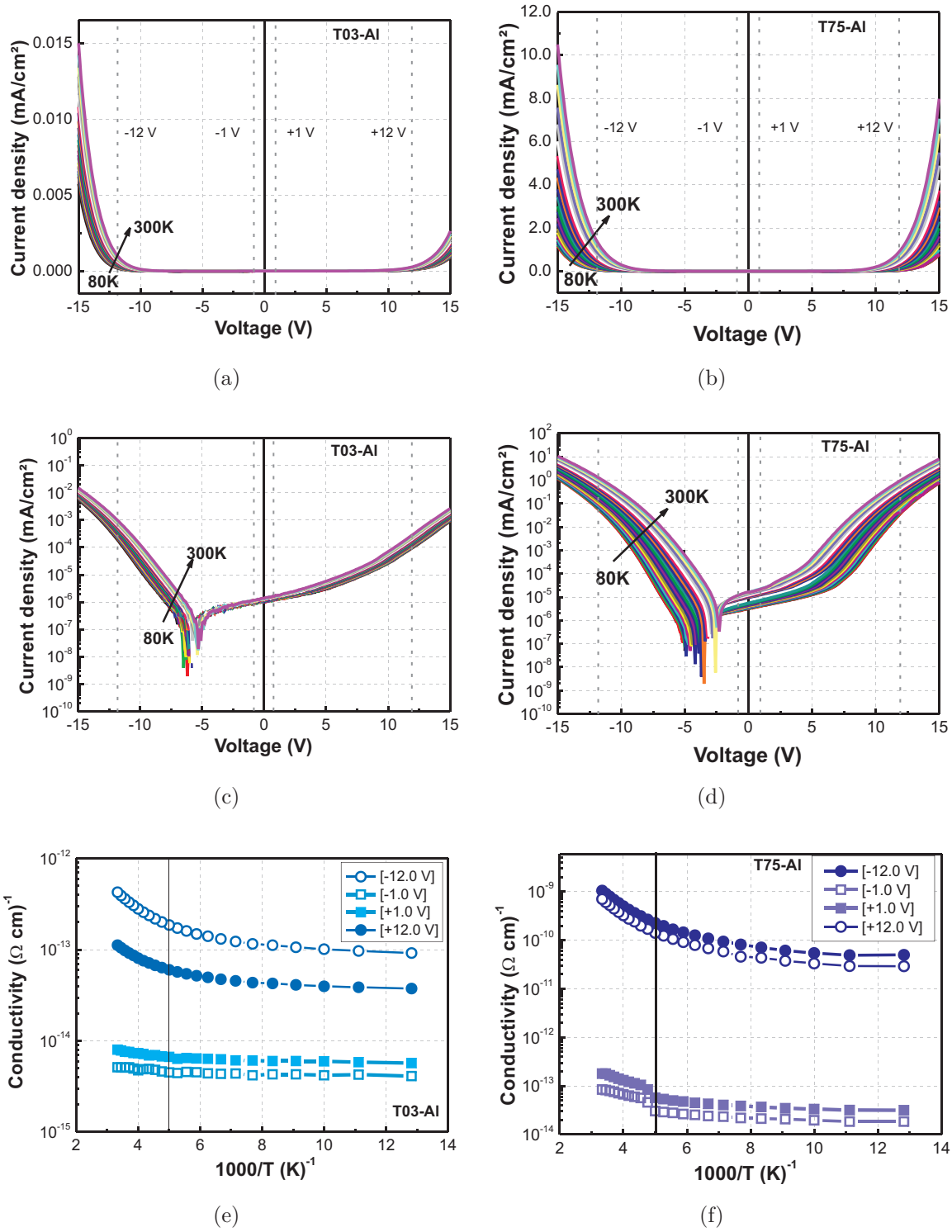

Figure 5.9: Low temperature (80 K - 300 K) electrical conduction characteristics of multilayer (T03-Al:left) and single layer structures (T75-Al:right) with Al electrodes. The current density vs voltage characteristics are shown in the linear scale (a),(b) and log scale (c),(d). Arrhenius plots with conductivity vs 1000/T are shown in (e),(f) for ±1 V and ±12 V.

5.4.1 Poole-Frenkel Conduction

Poole Frenkel is the conduction mechanism in insulators under high electric fields. It occurs due to the field enhanced thermal excitation of trapped electrons into the conduction band. The standard quantitative equation for the Poole-Frenkel emission effect is[175]:

$$J \propto E \exp\left[\frac{-q(\phi_b - \sqrt{qE/\pi\epsilon_i})}{k_b T}\right] \tag{5.1}$$

where J is the current density, E is the electric field, ϕ_b is the barrier height, and ϵ_i is the permittivity of the film with silicon nanocrystals.

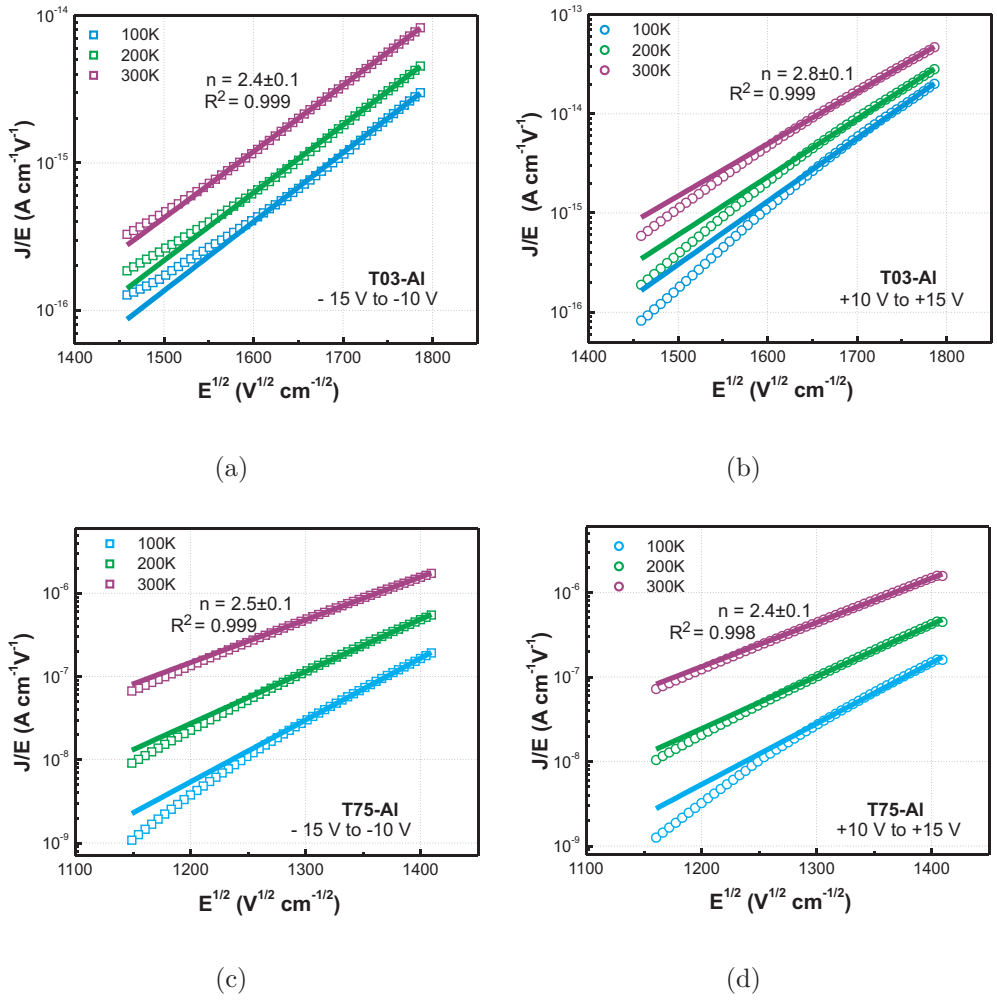

Figure 5.10: J/E vs $\sqrt{E}$ at high electric fields for T03-Al and T75-Al between (a),(c) -15 to -10 volts and (b),(d) +10 to +15 volts respectively. Good fits at 100 K, 200 K and 300 K indicate Poole-Frenkel conduction.

For voltages greater than 10 V, Figure 5.10 shows the Poole-Frenkel model fits for J/E vs $\sqrt{E}$ for multilayer and single layer films with Al electrodes (T03-Al and T75-Al respectively).

The refractive index n was calculated from the permittivity values obtained with the fits, using the relation $\epsilon = \sqrt{n^2 - k^2}$, and assuming $k = 0$ at T = 300 K. The refractive index values correspond well with each other, and also with the expected silicon enrichment. The differences with refractive indices using spectroscopic ellipsometry ($n = 2.05 \pm 0.15$) could be due to other conduction mechanisms that run in parallel as seen from the fits, the non-zero value of k which was omitted in this analysis, and errors from the ellipsometry measurements which have been discussed before.

5.4.2 Elucidating Conduction Mechanisms in Si Quantum Dots

Thickness of the SiO_x Layer and Size of the Si Quantum Dot

Multilayer formation by PECVD occurs by deposition of alternating layers of silicon rich oxide and silicon dioxide. This is done in a multiple-sequence deposition step, with a gas flow stabilisation time of a few seconds between each step and therefore each layer, to change the quality of the deposited film. The as-deposited stoichiometric silicon dioxide is a good insulating material.

On thermal annealing, the quantum dot size reaches a maximum diameter equal to the thickness of the silicon rich oxide layer, though it could also be smaller. The inter-dot distance is the thickness of the SiO_2 layer (1.5 nm), which is less than 2 nm to ensure tunnelling conduction between the dots. The thickness of the multilayers thus formed has been evaluated using spectroscopic ellipsometry, leading to significant yet inevitable errors because of the ultra-small dimensions of the films involved.

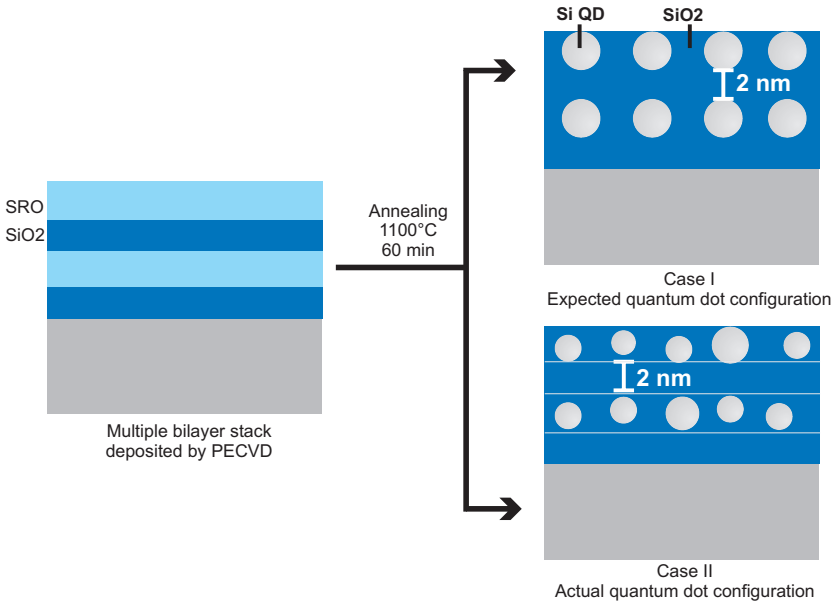

Figure 5.11: Expected and actual quantum dot configuration formed after annealing of the SRO-SiO_2 bilayers. The actual inter-dot distance may be greater than 2 nm, thus leading to decreased conductivity for thicker SRO films in bilayer stacks.

This has been illustrated in Figure 5.11, where we see the interfaces between deposited and annealed silicon dioxide. Defects may be present at the interfaces due to the initial differences between the films leading to differences in the quality of the oxide post-annealing. The quantum dots are not perfectly aligned vertically and the diameter of the Si dots may be smaller than the thickness of the SiO_x layers. This can increase the effective inter-dot distance, consequently decreasing electrical conduction. This is the reason why poor electrical conduction has been observed for silicon rich oxide thicknesses of 4 nm and 6 nm.

Film structure dependent electrical conductivity

The Arrhenius plots (conductivity vs 1000/T) for the different films fabricated during this thesis are compared in Figure 5.12 at -1 V. The best room temperature electrical conductivities were observed for the single layer sample Q30 (Chapter 2 and 3), with the randomly ordered Si quantum dots. The multilayers demonstrate extremely poor conductivities at low voltages because of the presence of a stoichiometric insulating oxide and larger inter-dot distances.

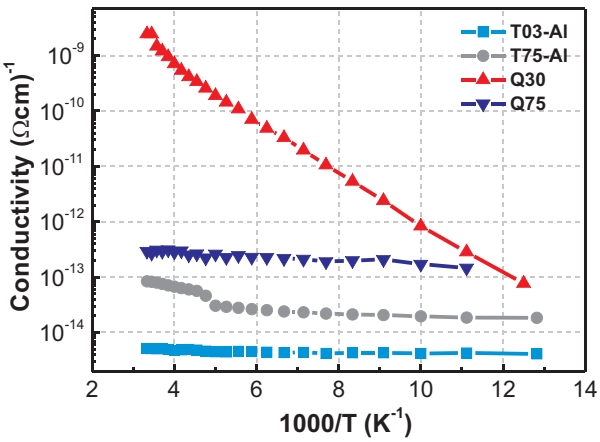

Figure 5.12: Comparison of Arrhenius plots (conductivity vs 1000/T) at -1.0 V for single layer samples Q30 and Q75 (Chapter 2 and 3), T75-Al and multilayers T03-Al. Q30 with disordered quantum dots demonstrates best room temperature conductivity, while poorest conductivity is observed in multilayer structures.

Ordered Dots and Conductivity

An explanation of the effect of quantum dot organization on conduction phenomena is suggested in Figure 5.13. In the ideal case for improved electrical conductivity (*Case I*), all quantum dots are perfectly aligned and the inter-dot distance is always 2 nm or less. All of the dots are expected to participate in the conduction pathways, leading to significant electrical conductivity in the film.

The real scenario is however *Case III*, where the inter-dot distance becomes larger than 2 nm, thus limiting the possibility of tunnelling conduction. This is the situation in samples Q75, T75-Al and T03-Al. There is limited variation in the inter-dot distance in T03-Al multilayers. This distance is uniform and could be greater than 2 nm, thus decreasing tunnelling probability and making percolation paths difficult. Thick single layers with organized quantum dots (Q75, T75-Al) have a slight dispersion in the inter-dot distances improving conductivity pathways. The best room temperature conductivities are observed in the case of single layer structures with randomly organized quantum dots (*Case II*), as the randomness and variations in inter-dot distance provide a percolation path leading to improved conduction in the film (Q30).

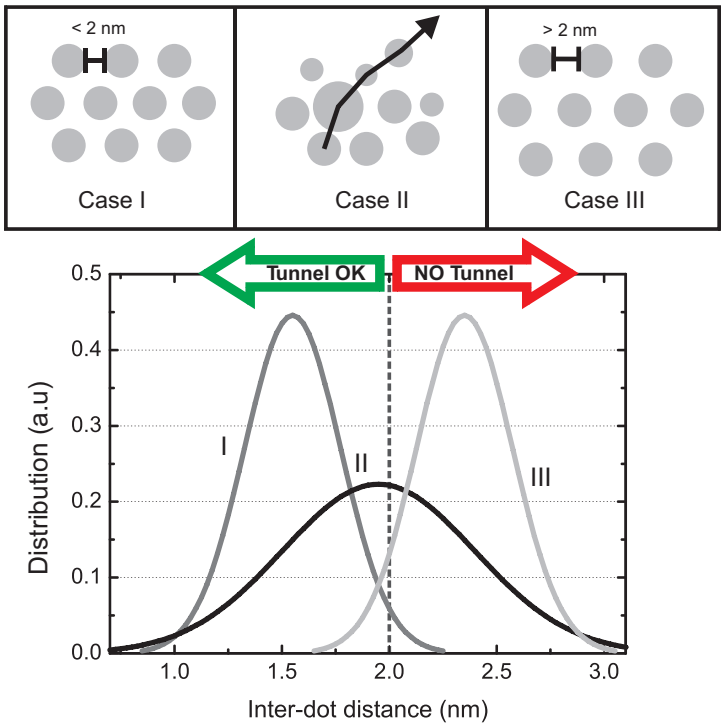

Figure 5.13: Schematic showing the distribution of inter-dot distances in a SiO_2 matrix. For ordered quantum dots in Case I, the inter-dot distance is always less than 2 nm ensuring tunnelling conduction. If this distance is greater than 2 nm like in case III, tunnelling is rather inefficient even in the case of ordered structures. Disorder in the inter-dot distance (case II) can lead to a large variation in distances.

5.5 Illumination Effects on Silicon Nanocrystals

ITO electrodes allow the transmission of up to 80 percent of incident light consequently leading to the measurement of electrical characteristics of the samples under illumination.

Spectral Response

The spectral response of a material describes its sensitivity to optical radiation of different wavelengths. This is done by measuring the photocurrent produced by a incident light intensity and its variation with the wavelength. The relation between the photoelectric sensitivity and wavelength is referred to as the spectral response and it is expressed in terms of photo sensitivity, quantum efficiency etc.

The *photosensitivity* (S) can be described as the ratio of the photocurrent (A) resulting from the incident radiant energy (expressed in Watts). The photosensitivity is expressed in A/W over the range of measured wavelengths. The *quantum efficiency* can also be used to express the spectral response. It describes the number N of electrons or holes that have been detected as a photocurrent divided by the number of the incident photons:

$$QE = N_{Electrons}/N_{Photons} = \frac{S \times 1240}{\lambda} \tag{5.2}$$

where S is the photo sensitivity in A/W at a given wavelength λ in nm.

The spectral response of the multilayer sample (T03-ITO250) and the thick single film (T75-ITO250) have been shown in Figure 5.14, for the spectral range of 430 to 1600 nm and different applied voltages.

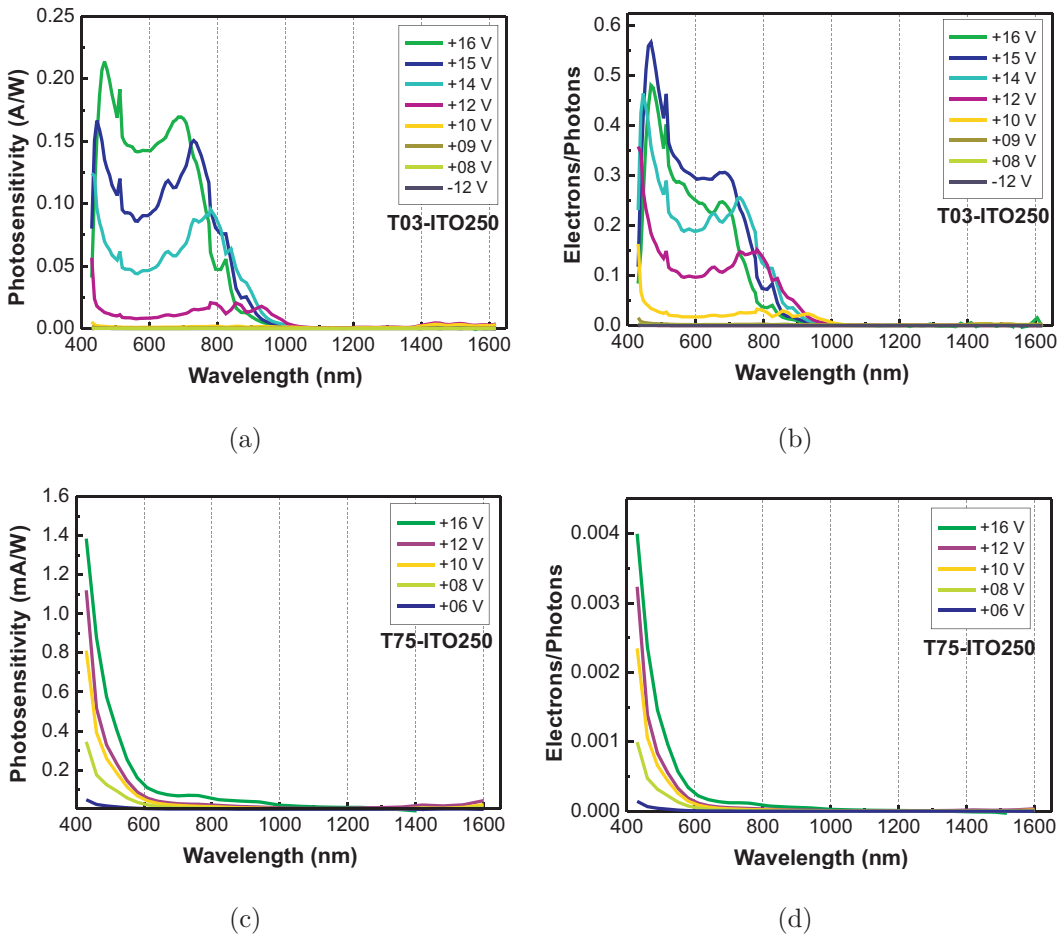

Figure 5.14: Spectral response of multilayer films and single layer films showing (a), (c) photosensitivity and (b), (d) electrons/photons (quantum efficiency). Improved response in the blue-green region is attributed to silicon quantum dots.

Poor conduction at low voltages demonstrated a correspondingly low optical signal and a poor spectral response. In the case of the multilayer sample T03-ITO250, the photosensitivity increases strongly on increasing voltages (Figure 5.14a). As the film begins to conduct at higher electric fields, the line shape of the spectral response in the 600-1200 nm range resembles that of crystalline silicon. Furthermore, for shorter wavelengths of 430-600 nm, an additional improved photoresponse is clearly observed, which can be attributed to absorption and blue-shift of the bandgap in the quantum dots. The quantum efficiency (electrons/photons) traced in Figure 5.14b demonstrates significant response of these multilayer films, with as many as 55 percent incident photons involved in photogenerated current in the green-blue visible spectral range.

For the thick single layer sample T75-ITO250, poor photosensitivity and quantum efficiency (Figure 5.14c and d) was observed in spite of its better electrical conductivity. Again, an improved response is observed in the 430 - 600 nm range which is atypical for bulk crystalline silicon, and can thus be attributed to absorption in silicon quantum dots. The low photosensitivity in the range of mA/W has been published before for similar films by Hossain et al,[170] although they did not demonstrate improved absorption in the blue spectral range. These poor photosensitivity results can be attributed to a larger size distribution of dots and poorer optical confinement in the single layer structures.

Even though these results were only obtained at high applied voltages which are not valid for photovoltaic applications, the improved absorption in the blue-green spectral range is promising for any solar cell integration. Improvement in electrical conductivity of the films can help overcome the drawback of having only high electric field conduction.

5.6 Summary

Silicon quantum dots with tunable bandgaps were fabricated using multilayer depositions on a large scale (on 200 mm wafers). Electrical characterizations were performed with different electrode materials, to ensure that the results are a response of quantum dots

and not of the metal-oxide-semiconductor junction formed. The different electrodes used were aluminium and B-doped polycrystalline silicon in p-i-n devices, and transparent conducting electrode ITO in n-i-p devices.

Poor room temperature electrical conductivity of less than 10^{-14} $m\Omega^{-1}cm^{-1}$ was observed in the multilayers as compared to thick single layers. This can be attributed to larger yet uniform inter-dot distances, in spite of careful control during the deposition process. This occurs as the size of the dots may be smaller than the thickness of the SiO_x layer, increasing the effective distance between dots. Additionally, a large number of interface states and defects introduce charge traps in the multilayer films.

The electrical conductivity in both types of films was observed to be temperature independent at low fields, and follows Poole-Frenkel conduction for high electric fields. Samples with transparent ITO electrodes were then used to evaluate the spectral response. Improved photosensitivity in the green-blue spectral region is obtained in the multilayers, with external quantum efficiencies as high as 55%. The thick single layers show a poor optical response, although the sensitivity to the blue wavelength region is still present.

We have successfully been able to improve either electrical conduction, or optical absorption in silicon quantum dot layers. While these are positive results for any photovoltaic applications, it is necessary to work towards simultaneously improving both these properties, which are requisite for photovoltaic integration.

Conclusion and Outlook

Silicon nanocrystals were fabricated and characterized for applications in silicon based advanced photovoltaic devices. The objectives and results of this research work are divided into three parts and summarized as follows:

1. *Adapting microelectronic techniques for large scale fabrication of silicon quantum dot layers in thick single films and alternating multilayer structures.*
   Plasma Enhanced CVD followed by high-temperature annealing was initially used to fabricate thick single layers (30 - 75 nm) of $SiO_{x<2}$ in a single deposition step. Using Design of Experiments to control the deposition parameters, this deposition procedure was transferred to ultra-thin film depositions. Full control over refractive index (silicon enrichment) and low deposition rates (1 nm/sec) was achieved. Multiple bilayers of 10 alternating bilayers of SiO_x (3 to 8 nm) and SiO_2 (1.5 nm) were then fabricated to control the dot size/band gap (which depends on the SiO_x thickness) and the inter-dot distance (assumed to be the SiO_2 thickness) which controls electrical conductivity.

2. *Understanding the structural properties of the films and quantum confinement in the dots using different morphological characterization techniques.*
   Thick single layer films show a thickness dependant spatially ordered formation of quantum dots which was attributed to the diffusion of Si in the SiO_x during the annealing step. This was made visible by TEM imaging after copper depositions on the silicon dislocations. All these thick films consist of luminescent and crystalline quantum dots, with average diameters around 5 nm.
   Multilayer films allow bandgap control of the quantum dots as the photoluminescence peak positions were observed to shift from 1.35 to 1.55 eV depending on SiO_x

thickness. However, it is difficult to determine the actual bandgap of the dots, as the photoluminescence depends on multiple factors including dote size, film environment, amorphous and crystalline content, defects, film strain etc.

3. *Comparing the electrical and optical properties in thick single layers and multiple bilayers.*

   The thickness dependent arrangement of quantum dots in thick single layers leads to thickness dependent electrical conductivity mechanisms. Disordered dots provide percolation conduction paths, where the low-field at room temperature conductivity ($10^{-9}\Omega^{-1}cm^{-1}$) phenomena can be explained by Nearest Neighbour Hopping. Ordered structures demonstrate temperature independent conductivity ($>10^{-13}\Omega^{-1}cm^{-1}$) which is a sign of tunnelling. Photocarrier generation and improved absorption in the blue range was observed in thick layers, although the external quantum efficiency was less than 0.4%.

   Multilayers show poor conductivity ($<10^{-14}\Omega^{-1}cm^{-1}$) as the thickness and the SiO_2 quality was controlled precisely with the depositions. The size of the dot may be smaller than the SiO_x thickness, increasing the effective inter-dot distance to more than 2 nm and hence decreasing electrical conductivity. Large amounts of charge traps were also observed in spite of H-passivation annealing. The conductivity was observed to be temperature independent, indicating tunnelling at low fields, and Poole-Frenkel conduction at high electric fields. Very strong photosensitivity was observed in the blue-green spectral range at high electric fields, with external quantum efficiencies up to 55%, which is very promising for photovoltaic applications.

Most research efforts involving silicon quantum dots for photovoltaic cells are now evolved around multiple bilayer structures. These layers show improved photoluminescence, bandgap control and significant photosensitivity in the green-blue spectral range. However, we have observed that charge carrier trapping effects were always present and much higher in these multiple bilayer structures. Furthermore, SiO_2 layer thickness of 1.5 nm was not low enough to ensure tunnelling conduction between the dots.

Ordered quantum dot formation and tunnelling conduction is indeed possible in

single layer structures and the slight disorder helps in improving conductivities. On the other hand, these films have a poor optical response, which is not sufficient for photovoltaic applications.

For photovoltaic integration, it is imperative to simultaneously control the band gap and optical properties of the film along with the electrical conduction. Both thick single layer and multiple bilayers need to be examined further.

In the future, efforts should be made to analyse Si diffusion and quantum dot formation in thicker layers based on Si enrichment, thickness and annealing conditions. This can aid in forming self-organized yet luminescent dots in single layer films, which have already demonstrated better electrical conductivities.
Electrical conductivities in multilayers need to be improved significantly, and possible options for doing so include the following:

- Decreasing thickness of the SiO_2 in the multilayer stack to improve tunnelling probability by further decreasing inter-dot distance.
- Decreasing number of multilayers to see the possible effect on conductivity, and increase probable conduction pathways.
- Doping the multilayer samples to improve conductivity.

Sustained efforts to simultaneously improve conductivity and optical activity are therefore possible and imperative for integration of quantum dots into photovoltaic devices.

References

[1] Moore GE. *"Cramming more components onto integrated circuits"*. Electronics **38** (1965).

[2] Canham L. *"Silicon quantum wire array fabrication by electrochemical and chemical dissolution of wafers"*. Appl. Phys. Lett. **57**(10), 1046–1048 (1990).

[3] Cullis AG and Canham LT. *"Visible-light emission due to quantum size effects in highly porous crystalline silicon"*. Nature **353**(6342), 335–338 (1991).

[4] Soref R. *"Silicon-based optoelectronics"*. Proceedings of the IEEE **81**(12), 1687–1706 (1993).

[5] Yuan ZZ, Anopchenko A, Daldosso N, Guider R, Navarro-Urrios D, Pitanti A, Spano R, and Pavesi L. *"Silicon nanocrystals as an enabling material for silicon photonics"*. Proceedings of the IEEE **97**(7), 1250–1268 (2009).

[6] Bogaerts W, Baets R, Dumon P, Wiaux V, Beckx S, Taillaert D, Luyssaert B, Van Campenhout J, Bienstman P, and Van Thourhout D. *"Nanophotonic waveguides in silicon-on-insulator fabricated with CMOS technology"*. Journal of Lightwave Technology **23**(1), 401–412 (2005).

[7] Nature Photonics Editorial. *"Simply silicon"*. Nature Photonics **4**(8), 491 (2010).

[8] Intel Labs. "The 50G silicon photonics link - the world's first silicon-based optical data connection with integrated lasers" (2010). URL `www.intel.com/go/sp`.

[9] Assefa S, Xia FN, Green WMJ, Schow CL, Rylyakov AV, and Vlasov YA. *"CMOS-integrated optical receivers for on-chip interconnects"*. IEEE J. Sel. Topics in Quantum Electron. **16**(5), 1376–1385 (2010).

[10] Greenemeier L. *"Solar sell: Companies that mass marketed PCs turn to photovoltaics"*. Scientific American (2008).

[11] Alivisatos AP. *"Semiconductor clusters, nanocrystals, and quantum dots"*. Science **271**(5251), 933–937 (1996).

[12] Yoffe A. *"Semiconductor quantum dots and related systems: electronic, optical, luminescence and related properties of low dimensional systems"*. Advances in Physics **50**(1), 1–208 (2001).

[13] Brus L. *"Electronic wave-functions in semiconductor clusters - experiment and theory"*. J. Phys. Chem.-US **90**(12), 2555–2560 (1986).

[14] Brus L. *"Zero-dimensional excitons in semiconductor clusters"*. IEEE J. Quantum. Electron. **22**(9), 1909–1914 (1986).

[15] Ledoux G, Guillois O, Porterat D, Reynaud C, Huisken F, Kohn B, and Paillard V. *"Photoluminescence properties of silicon nanocrystals as a function of their size"*. Phys. Rev. B **62**(23), 15942–15951 (2000).

[16] Niquet Y, Delerue C, Allan G, and Lannoo M. *"Method for tight-binding parametrization: Application to silicon nanostructures"*. Phys. Rev. B **62**(8), 5109–5116 (2000).

[17] Schuppler S, Friedman SL, Marcus MA, Adler DL, Xie YH, Ross FM, Chabal YJ, Harris TD, Brus LE, Brown WL, Chaban EE, Szajowski PF, Christman SB, and Citrin PH. *"Size, shape, and composition of luminescent species in oxidized Si nanocrystals and H-passivated porous Si"*. Phys. Rev. B **52**(7), 4910–4925 (1995).

[18] Fujii M, Yoshida M, Hayashi S, and Yamamoto K. *"Photoluminescence from SiO_2 films containing Si nanocrystals and Er: Effects of nanocrystalline size on the photoluminescence efficiency of Er^{3+}"*. J. Appl. Phys. **84**(8), 4525–4531 (1998).

[19] Takagi H, Ogawa H, Yamazaki Y, Ishizaki A, and Nakagiri T. *"Quantum size effects on photoluminescence in ultrafine Si particles"*. Appl. Phys. Lett. **56**(24), 2379–2380 (1990).

[20] Takeoka S, Fujii M, and Hayashi S. *"Size-dependent photoluminescence from surface-oxidized Si nanocrystals in a weak confinement regime"*. Phys. Rev. B **62**(24), 16820–16825 (2000).

[21] Ehbrecht M, Kohn B, Huisken F, Laguna MA, and Paillard V. *"Photoluminescence and resonant Raman spectra of silicon films produced by size-selected cluster beam deposition"*. Phys. Rev. B **56**(11), 6958–6964 (1997).

[22] Lopez M, Garrido B, Garcia C, Pellegrino P, Perez-Rodriguez A, Morante J, Bonafos C, Carrada M, and Claverie A. *"Elucidation of the surface passivation role on the photoluminescence emission yield of silicon nanocrystals embedded in SiO_2"*. Appl. Phys. Lett. **80**(9), 1637–1639 (2002).

[23] Delley B and Steigmeier EF. *"Size dependence of band-gaps in silicon nanostructures"*. Appl. Phys. Lett. **67**(16), 2370–2372 (1995).

[24] Conibeer G, Green M, Cho EC, Konig D, Cho YH, Fangsuwannarak T, Scardera G, Pink E, Huang YD, Puzzer T, Huang SJ, Song DY, Flynn C, Park S, Hao XJ, and Mansfield D. *"Silicon quantum dot nanostructures for tandem photovoltaic cells"*. Thin Solid Films **516**(20), 6748–6756 (2008).

[25] Puzder A, Williamson AJ, Grossman JC, and Galli G. *"Surface chemistry of silicon nanoclusters"*. Phys. Rev. Lett. **88**(9), 097401 (2002).

[26] Koenig D, Rudd J, Green MA, and Conibeer G. *"Impact of interface on the effective band gap of Si quantum dots"*. Sol. Energ. Mat. Sol. C. **93**(6-7), Japan Soc Appl Phys; IEEE; Nagoya Ind Sci Res Inst (2009).

[27] Tsybeskov L, Hirschman KD, Duttagupta SP, Zacharias M, Fauchet PM, McCaffrey JP, and Lockwood DJ. *"Nanocrystalline-silicon superlattice produced by controlled recrystallization rid a-5868-2011"*. Appl. Phys. Lett. **72**(1), 43–45 (1998).

[28] Daldosso N, Luppi M, Ossicini S, Degoli E, Magri R, Dalba G, Fornasini P, Grisenti R, Rocca F, Pavesi L, Boninelli S, Priolo F, Spinella C, and Iacona F. *"Role of the interface region on the optoelectronic properties of silicon nanocrystals embedded in SiO_2"*. Phys. Rev. B **68**(8) (2003).

[29] Wolkin MV, Jorne J, Fauchet PM, Allan G, and Delerue C. *"Electronic states and luminescence in porous silicon quantum dots: The role of oxygen"*. Phys. Rev. Lett. **82**(1), 197–200 (1999).

[30] Walters RJ. *Silicon Nanocrystals for Silicon Photonics*. PhD thesis, California Institute of Technology, (2007).

[31] Delley B and Steigmeier EF. *"Quantum confinement in Si nanocrystals"*. Phys. Rev. B **47**(3), 1397–1400 (1993).

[32] Kovalev D, Heckler H, Ben-Chorin M, Polisski G, Schwartzkopff M, and Koch F. *"Breakdown of the k-conservation rule in Si nanocrystals"*. Phys. Rev. Lett. **81**(13), 2803–2806 (1998).

[33] Kovalev D, Heckler H, Polisski G, and Koch F. *"Optical properties of Si nanocrystals"*. Physica Status Solidi B-basic research **215**(2), 871–932 (1999).

[34] Heitmann J, Muller F, Zacharias M, and Gosele U. *"Silicon nanocrystals: Size matters"*. Adv. Mater. **17**(7), 795–803 (2005).

[35] Pavesi L, Dal Negro L, Mazzoleni C, Franzo G, and Priolo F. *"Optical gain in silicon nanocrystals"*. Nature **408**(6811), 440–444 (2000).

[36] Walters RJ, Bourianoff GI, and Atwater HA. *"Field-effect electroluminescence in silicon nanocrystals"*. Nat. Mater. **4**(2), 143–146 (2005).

[37] Yu Z and Aceves-Mijares M. *"A ultraviolet-visible-near infrared photodetector using nanocrystalline Si superlattice"*. Appl. Phys. Lett. **95**(8) (2009).

[38] Shieh JM, Yu WC, Huang JY, Wang CK, Dai BT, Jhan HY, Hsu CW, Kuo HC, Yang FL, and Pan CL. *"Near-infrared silicon quantum dots metal-oxide-semiconductor field-effect transistor photodetector"*. Appl. Phys. Lett. **94**(24), 241108 (2009).

[39] Khriachtchev L, Rasanen M, and Novikov S. *"Efficient wavelength-selective optical waveguiding in a silica layer containing Si nanocrystals"*. Appl. Phys. Lett. **83**(15), 3018–3020 (2003).

[40] Navarro-Urrios D, Pitanti A, Daldosso N, Gourbilleau F, Rizk R, Pucker G, and Pavesi L. *"Quantification of the carrier absorption losses in Si-nanocrystal rich rib waveguides at 1.54 μ m"*. Appl. Phys. Lett. **92**(5) (2008).

[41] Ghulinyan M, Navarro-Urrios D, Pitanti A, Lui A, Pucker G, and Pavesi L. *"Whispering-gallery modes and light emission from a Si-nanocrystal-based single microdisk resonator"*. Opt. Express **16**(17), 13218–13224 (2008).

[42] Zhang R, Seo S, Milenin A, Zacharias M, and Gosele U. *"Visible range whispering-gallery mode in microdisk array based on size-controlled Si nanocrystals"*. Appl. Phys. Lett. **88**(15) (2006).

[43] Kekatpure RD and Brongersma ML. *"Fundamental photophysics and optical loss processes in Si-nanocrystal-doped microdisk resonators"*. Physical Review A **78**(2), 023829 (2008).

[44] Goodman JW, Leonberger FJ, Kung SY, and Athale RA. *"Optical interconnections for VLSI systems"*. Proceedings of the IEEE **72**(7), 850–866 (1984).

[45] Kimerling LC. *"Silicon microphotonics"*. Appl. Surf. Sci. **159**, 8–13 (2000).

[46] Miller DAB. *"Rationale and challenges for optical interconnects to electronic chips"*. Proceedings of the IEEE **88**(6), 728–749 (2000).

[47] Walters R, Kik P, Casperson J, Atwater H, Lindstedt R, Giorgi M, and Bourianoff G. *"Silicon optical nanocrystal memory"*. Appl. Phys. Lett. **85**(13), 2622–2624 (2004).

[48] Tiwari S, Rana F, Hanafi H, Hartstein A, Crabbe EF, and Chan K. *"A silicon nanocrystals based memory"*. Appl. Phys. Lett. **68**(10), 1377–1379 (1996).

[49] Lombardo S, De Salvo B, Gerardi C, and Baron T. *"Silicon nanocrystal memories"*. Microelectron. Eng. **72**(1-4), 388–394 (2004).

[50] Compagnoni CM, Gusmeroli R, Ielmini D, Spinelli AS, and Lacaita AL. *"Silicon nanocrystal memories: A status update"*. J. Nanosci. Nanotechnol. **7**(1), 193–205 (2007).

[51] Salvo BD. *Silicon Non-Volatile Memories - Paths of Innovation*. John Wiley & Sons, Inc., (2009).

[52] Conibeer G, Green M, Corkish R, Cho Y, Cho EC, Jiang CW, Fangsuwannarak T, Pink E, Huang YD, Puzzer T, Trupke T, Richards B, Shalav A, and Lin KL. *"Silicon nanostructures for third generation photovoltaic solar cells"*. Thin Solid Films **511**, 654–662 (2006).

[53] Cho EC, Park S, Hao X, Song D, Conibeer G, Park SC, and Green MA. *"Silicon quantum dot/crystalline silicon solar cells"*. Nanotechnology **19**(24) (2008).

[54] Hao XJ, Cho EC, Flynn C, Shen YS, Conibeer G, and Green MA. *"Effects of boron doping on the structural and optical properties of silicon nanocrystals in a silicon dioxide matrix"*. Nanotechnology **19**(42) (2008).

[55] Rolver R, Berghoff B, Batzner DL, Spangenberg B, and Kurz H. *"Lateral si/sio$_2$ quantum well solar cells"*. Appl. Phys. Lett. **92**(21) (2008).

[56] The European Photovoltaic Industry Association G. "Solar generation 6 - solar photovoltaic electricity empowering the world", (2011).

[57] Jäger-Waldau A. "PV Status Report 2010 - Research, Solar Cell Production and Market Implementation of Photovoltaics". Technical report, European Commission Joint Research Centre, Institute for Energy, (2010).

[58] International Energy Agency. "Technology Roadmap - Solar Photovoltaic Energy", (2010).

[59] Green MA, Emery K, Hishikawa Y, and Warta W. *"Solar cell efficiency tables (version 37)"*. Prog. Photovoltaics **19**(1), 84–92 (2011).

[60] Takamoto T, Agui T, Yoshida A, Nakaido K, Juso H, Sasaki K, Nakamora K, Yamaguchi H, Kodama T, Washio H, Imaizumi M, and Takahashi M. *"World's highest efficiency triple-junction solar cells fabricated by inverted layers transfer process"*. 2010 35th IEEE Photovoltaic Specialists Conference (PVSC) (2010).

[61] American Society for Testing and Materials (ASTM) Terrestrial Reference Spectra for Photovoltaic Performance Evaluation. "Reference Solar Spectral Irradiance: Air Mass 1.5". URL `http://rredc.nrel.gov/solar/spectra/am1.5/`.

[62] Shockley W and Queisser HJ. *"Detailed balance limit of efficiency of p-n junction solar cells"*. J. Appl. Phys. **32**(3), 510–519 (1961).

[63] Green MA. *"Third generation photovoltaics: Ultra-high conversion efficiency at low cost"*. Prog. Photovoltaics **9**(2), 123–135 (2001).

[64] Nozik AJ. *"Quantum dot solar cells"*. Physica E-low-dimensional Systems & Nanostructures **14**(1-2), 115–120 (2002).

[65] Green MA, Conibeer G, Konig D, Shrestha S, Huang S, Aliberti P, Treiber L, Patterson R, Veettil BP, Hsieh A, Feng Y, Luque A, Marti A, Linares PG, Ca novas E, Antolin E, Marro n DF, Tablero C, Herna ndez E, Guillemoles JF, Huang L, Le Bris A, Schmidt T, Clady R, and Tayebjee M. *"Hot carrier solar cells: Challenges and recent progress"*. 2010 35th IEEE Photovoltaic Specialists Conference (PVSC) , 000057–60 (2010).

[66] Conibeer G. *"Third-generation photovoltaics"*. Materials Today **10**, 42–50 (2007).

[67] Ross RT and Nozik AJ. *"Efficiency of hot-carrier solar-energy converters"*. J. Appl. Phys. **53**(5), 3813–3818 (1982).

[68] Wurfel P. *"Solar energy conversion with hot electrons from impact ionisation"*. Sol. Energ. Mat. Sol. C. **46**(1), 43–52 (1997).

[69] Boudreaux DS, Williams F, and Nozik AJ. *"Hot carrier injection at semiconductor-electrolyte junctions"*. J. Appl. Phys. **51**(4), 2158–2163 (1980).

[70] Konig D, Casalenuovo K, Takeda Y, Conibeer G, Guillemoles JF, Patterson R, Huang LM, and Green MA. *"Hot carrier solar cells: Principles, materials and design"*. Physica E **42**(10), 2862–2866 (2010).

[71] Landsberg PT, Nussbaumer H, and Willeke G. *"Band-band impact ionization and solar-cell efficiency"*. J. Appl. Phys. **74**(2), 1451–1452 (1993).

[72] Kolodinski S, Werner JH, Wittchen T, and Queisser HJ. *"Quantum efficiencies exceeding unity due to impact ionization in silicon solar-cells"*. Appl. Phys. Lett. **63**(17), 2405–2407 (1993).

[73] Schaller RD and Klimov VI. *"High efficiency carrier multiplication in PbSe nanocrystals: Implications for solar energy conversion"*. Phys. Rev. Lett. **92**(18), 186601 (2004).

[74] Luque A and Marti A. *"Increasing the efficiency of ideal solar cells by photon induced transitions at intermediate levels"*. Phys. Rev. Lett. **78**(26), 5014–5017 (1997).

[75] Luque A and Marti A. *"Photovoltaics - towards the intermediate band"*. Nature Photonics **5**(3), 137–138 (2011).

[76] Plass R, Pelet S, Krueger J, Gratzel M, and Bach U. *"Quantum dot sensitization of organic-inorganic hybrid solar cells"*. J. Phys. Chem. B **106**(31), 7578–7580 (2002).

[77] Choi JJ, Lim YF, Santiago-Berrios MB, Oh M, Hyun BR, Sung LF, Bartnik AC, Goedhart A, Malliaras GG, Abruna HD, Wise FW, and Hanrath T. *"PbSe nanocrystal excitonic solar cells"*. Nano Lett. **9**(11), 3749–3755 (2009).

[78] Kim SK, Cho CH, Kim BH, Park SJ, and Lee JW. *"Electrical and optical characteristics of silicon nanocrystal solar cells"*. Appl. Phys. Lett. **95**(14), 143120 (2009).

[79] Hao XJ, Cho EC, Flynn C, Shen YS, Park SC, Conibeer G, and Green MA. *"Synthesis and characterization of boron-doped Si quantum dots for all-Si quantum dot tandem solar cells"*. Sol. Energ. Mat. Sol. C. **93**(2), 273–279 (2009).

[80] Hao XJ, Cho EC, Scarder G, Shen YS, Bellet-Amalric E, Bellet D, Conibeer G, and Green MA. *"Phosphorus-doped silicon quantum dots for all-silicon quantum dot tandem solar cells"*. Sol. Energ. Mat. Sol. C. **93**(9), 1524–1530 (2009).

[81] Gourbilleau F, Dufour C, Rezgui B, and Bremond G. *"Silicon nanostructures for solar cell applications"*. Mater. Sci. Eng. B-Adv. **159-60**, 70–73 (2009).

[82] Wu MH, Mu R, Ueda A, Henderson DO, and Vlahovic B. *"Production of silicon quantum dots for photovoltaic applications by picosecond pulsed laser ablation"*. Mat. Sci. Eng. B-Solid **116**(3), 273–277 (2005).

[83] Rolver R, Berghoff B, Batzner D, Spangenberg B, Kurz H, Schmidt M, and Stegemann B. *"Si/sio$_2$ multiple quantum wells for all silicon tandem cells: Conductivity and photocurrent measurements"*. Thin Solid Films **516**(20), 6763–6766 (2008).

[84] Kirchartz T, Seino K, Wagner JM, Rau U, and Bechstedt F. *"Efficiency limits of si/sio$_2$ quantum well solar cells from first-principles calculations"*. J. Appl. Phys. **105**(10), 104511 (2009).

[85] Maestre D, Palais O, Barakel D, Pasquinelli M, Alfonso C, Gourbilleau F, De Laurentis M, and Irace A. *"Structural and optoelectronical characterization of Si-SiO$_2$/SiO$_2$ multilayers with applications in all Si tandem solar cells"*. J. Appl. Phys. **107**(6), 064321 (2010).

[86] Hong SH, Park JH, Shin DH, Kim CO, Choi SH, and Kim KJ. *"Doping- and size-dependent photovoltaic properties of p-type si-quantum-dot heterojunction solar cells: correlation with photoluminescence"*. Appl. Phys. Lett. **97**(7), 072108 (2010).

[87] Perez-Wurfl I, Hao XJ, Gentle A, Kim DH, Conibeer G, and Green MA. *"Si nanocrystal p-i-n diodes fabricated on quartz substrates for third generation solar cell applications"*. Appl. Phys. Lett. **95**(15), 153506 (2009).

[88] Meillaud F, Shah A, Droz C, Vallat-Sauvain E, and Miazza C. *"Efficiency limits for single junction and tandem solar cells"*. Sol. Energ. Mat. Sol. C. **90**(18-19), 2952–2959 (2006).

[89] Shrestha SK, Aliberti P, and Conibeer GJ. *"Energy selective contacts for hot carrier solar cells"*. Sol. Energ. Mat. Sol. C. **94**(9), 1546–1550 (2010).

[90] Aliberti P, Shrestha SK, Teuscher R, Zhang B, Green MA, and Conibeer GJ. *"Study of silicon quantum dots in a SiO$_2$ matrix for energy selective contacts applications"*. Sol. Energ. Mat. Sol. C. **94**(11), 1936–1941 (2010).

[91] Suckow S, Berghoff B, and Kurz H. *"Geometric broadening in resonant tunneling through Si quantum dots"*. E-MRS 2009 Spring Meeting - Proc. Inorganic and Nanostructured Photovoltaics **2**(1), 207–212 (2010).

[92] Conibeer G, Ekins-Daukes N, Guillemoles JF, Konig D, Cho EC, Jiang CW, Shrestha S, and Green M. *"Progress on hot carrier cells"*. Solar Energy Materials and Solar Cells **93**(6-7), 713–719 (2009).

[93] Timmerman D, Izeddin I, Stallinga P, Yassievich IN, and Gregorkiewicz T. *"Space-separated quantum cutting with silicon nanocrystals for photovoltaic applications"*. Nature Photonics **2**(2), 105–109 (2008).

[94] Liu CY, Holman ZC, and Kortshagen UR. *"Hybrid solar cells from P3HT and silicon nanocrystals"*. Nano Lett. **9**(1), 449–452 (2009).

[95] Prezioso S, Hossain SM, Anopchenko A, Pavesi L, Wang M, Pucker G, and Bellutti P. *"Superlinear photovoltaic effect in Si nanocrystals based metal-insulator-semiconductor devices"*. Appl. Phys. Lett. **94**(6) (2009).

[96] Beard MC, Knutsen KP, Yu P, Luther JM, Song Q, Metzger WK, Ellingson RJ, and Nozik AJ. *"Multiple exciton generation in colloidal silicon nanocrystals"*. Nano Lett. **7**(8), 2506–2512 (2007).

[97] Strumpel C, McCann M, Beaucarne G, Arkhipov V, Slaoui A, Svrcek V, del Canizo C, and Tobias I. *"Modifying the solar spectrum to enhance silicon solar cell efficiency - an overview of available materials"*. Sol. Energ. Mat. Sol. C. **91**(4), 238–249 (2007).

[98] Svrcek V, Slaoui A, and Muller JC. *"Silicon nanocrystals as light converter for solar cells"*. Thin Solid Films **451**, 384–388 (2004).

[99] Malguth E, Roczen M, Gref O, Schoepke A, and Schmidt M. *"Development of ultra-thin tunneling oxides and Si/SiO_2 nanostructures for the application in silicon solar cells"*. Phys. Status. Solidi. A **208**(3), 612–615 (2011).

[100] Nesbit LA. *"Annealing characteristics of Si-rich SiO_2 films"*. Appl. Phys. Lett. **46**(1), 38–40 (1985).

[101] Shimizuiwayama T, Nakao S, and Saitoh K. *"Visible photoluminescence in Si+ implanted thermal oxide films on crystalline Si"*. Appl. Phys. Lett. **65**(14), 1814–1816 (1994).

[102] Littau KA, Szajowski PJ, Muller AJ, Kortan AR, and Brus LE. *"A luminescent silicon nanocrystal colloid via a high-temperature aerosol reaction"*. J. Phys. Chem.-US **97**(6), 1224–1230 (1993).

[103] Gago R, Vazquez L, Cuerno R, Varela M, Ballesteros C, and Albella JM. *"Production of ordered silicon nanocrystals by low-energy ion sputtering"*. Appl. Phys. Lett. **78**(21), 3316–3318 (2001).

[104] Zacharias M, Heitmann J, Scholz R, Kahler U, Schmidt M, and Blasing J. *"Size-controlled highly luminescent silicon nanocrystals: A SiO/SiO_2 superlattice approach"*. Appl. Phys. Lett. **80**(4), 661–663 (2002).

[105] Patrone L, Nelson D, Safarov VI, Sentis M, Marine W, and Giorgio S. *"Photoluminescence of silicon nanoclusters with reduced size dispersion produced by laser ablation"*. J. Appl. Phys. **87**(8), 3829–3837 (2000).

[106] Ding ZF, Quinn BM, Haram SK, Pell LE, Korgel BA, and Bard AJ. *"Electrochemistry and electrogenerated chemiluminescence from silicon nanocrystal quantum dots"*. Science **296**(5571), 1293–1297 (2002).

[107] Holmes JD, Ziegler KJ, Doty RC, Pell LE, Johnston KP, and Korgel BA. *"Highly luminescent silicon nanocrystals with discrete optical transitions"*. J. Am. Chem. Soc. **123**(16), 3743–3748 (2001).

[108] Kim TY, Park NM, Kim KH, Sung GY, Ok YW, Seong TY, and Choi CJ. *"Quantum confinement effect of silicon nanocrystals in situ grown in silicon nitride films"*. Appl. Phys. Lett. **85**(22), 5355–5357 (2004).

[109] Jiang CW and Green MA. *"Silicon quantum dot superlattices: Modeling of energy bands, densities of states, and mobilities for silicon tandem solar cell applications"*. J. Appl. Phys. **99**(11), 114902 (2006).

[110] Applied Materials. *DCVD Process: Concepts and Measurements - Student Guide.*

[111] Bedjaoui M, Despax B, Caumont M, and Bonafos C. *"Si nanocrystal-containing SiO_x ($x < 2$) produced by thermal annealing of PECVD realized thin films"*. Mat. Sci. Eng. B-Solid **124**, 508–512 (2005).

[112] Caristia L, Nicotra G, Bongiorno C, Costa N, Ravesi S, Coffa S, De Bastiani R, Grimaldi MG, and Spinella C. *"The influence of hydrogen and nitrogen on the formation of si nanoclusters embedded in sub-stoichiometric silicon oxide layers"*. Microelectron. Reliab. **47**(4-5), 777–780 (2007).

[113] Shi GH, Xu G, and Han GR. *"Preparation and photoluminescence of nanocrystalline Si-rich silicon oxide films by PECVD"*. Mater. Lett. **61**(2), 463–465 (2007).

[114] Zacharias M, Blasing J, Veit P, Tsybeskov L, Hirschman K, and Fauchet PM. *"Thermal crystallization of amorphous Si/SiO_2 superlattices"*. Appl. Phys. Lett. **74**(18), 2614–2616 (1999).

[115] Chen XY, Lu YF, Tang LJ, Wu YH, Cho BJ, Xu XJ, Dong JR, and Song WD. *"Annealing and oxidation of silicon oxide films prepared by plasma-enhanced chemical vapor deposition"*. J. Appl. Phys. **97**(1), 014913 (2005).

[116] Daldosso N, Das G, Larcheri S, Mariotto G, Dalba G, Pavesi L, Irrera A, Priolo F, Iacona F, and Rocca F. *"Silicon nanocrystal formation in annealed silicon-rich silicon oxide films prepared by plasma enhanced chemical vapor deposition"*. J. Appl. Phys. **101**(11), 113510 (2007).

[117] Hinds BJ, Wang F, Wolfe DM, Hinkle CL, and Lucovsky G. *"Investigation of postoxidation thermal treatments of Si/SiO_2 interface in relationship to the kinetics of amorphous Si suboxide decomposition"*. J. Vac. Sci. Technol. B **16**(4), 2171–2176 (1998).

[118] Zacharias M and Streitenberger P. *"Crystallization of amorphous superlattices in the limit of ultrathin films with oxide interfaces"*. Phys. Rev. B **62**(12), 8391–8396 (2000).

[119] Yi LX, Heitmann J, Scholz R, and Zacharias M. *"Si rings, Si clusters, and Si nanocrystals-different states of ultrathin SiO_x layers"*. Appl. Phys. Lett. **81**(22), 4248–4250 (2002).

[120] Godefroo S, Hayne M, Jivanescu M, Stesmans A, Zacharias M, Lebedev OI, Van Tendeloo G, and Moshchalkov VV. *"Classification and control of the origin of photoluminescence from Si nanocrystals"*. Nature Nanotechnology **3**(3), 174–178 (2008).

[121] Gosele U. *"Shedding new light on silicon"*. Nature Nanotechnology **3**(3), 134–135 (2008).

[122] Pai PG, Chao SS, Takagi Y, and Lucovsky G. *"Infrared spectroscopic study of SiO_x films produced by plasma enhanced chemical vapor-deposition"*. J. Vac. Sci. Technol. A **4**(3), 689–694 (1986).

[123] Tsu DV, Lucovsky G, and Davidson BN. *"Effects of the nearest neighbors and the alloy matrix on SiH stretching vibrations in the amorphous SiO_r-H (0-less-than-r-less-than-2) alloy system"*. Phys. Rev. B **40**(3), 1795–1805 (1989).

[124] Buffet N. "Précipitation de nanocristaux de silicium dans une matrice SiO_2 à partir d'un oxyde sous stoechiométrique SiO_x (enrichi en silicium) elaboré par dépôt chimique en phase vapeur à basse pression (LPCVD).". Master's thesis, (2000).

[125] JA Woollam Co, Inc. "Ellipsometry tutorial". URL `http://www.jawoollam.com/`.

[126] San Andres E, del Prado A, Martil I, Gonzalez G, Martinez FL, Bravo D, Lopez FJ, and Fernandez M. *"Physical properties of plasma deposited SiO_x thin films"*. Vacuum **67**(3-4), 525–529 (2002).

[127] Bruggeman D. *"Dielectric constant and conductivity of mixtures of isotropic materials"*. Ann. Phys. **24**, 236 (1935).

[128] Bauer G and Richter W. *Optical Characterization of Epitaxial Semiconductor Layers*. Springer-Verlag Berlin Heidelberg, (1996).

[129] Jellison GE and Modine FA. *"Parameterization of the optical functions of amorphous materials in the interband region"*. Appl. Phys. Lett. **69**(3), 371–373 (1996).

[130] Delerue C, Allan G, and Lannoo M. *"Theoretical aspects of the luminescence of porous silicon"*. Phys. Rev. B **48**(15), 11024–11036 (1993).

[131] Dinh LN, Chase LL, Balooch M, Siekhaus WJ, and Wooten F. *"Optical properties of passivated Si nanocrystals and SiO_x nanostructures"*. Phys. Rev. B **54**(7), 5029–5037 (1996).

[132] Ternon C. *Nanostructures luminescentes à base de silice et de silicium: de l'élaboration par pulvérisation magnétron réactive à la modélisation de la photoluminescence.* PhD thesis, Université de Caen, (2002).

[133] Yurtsever A, Weyland M, and Muller DA. *"Three-dimensional imaging of nonspherical silicon nanoparticles embedded in silicon oxide by plasmon tomography".* Appl. Phys. Lett. **89**(15), 151920 (2006).

[134] Fitting HJ, Kourkoutis LF, Salh R, Zamoryanskaya MV, and Schmidt B. *"Silicon nanocluster aggregation in SiO_2:Si layers".* Phys. Status. Solidi. A **207**(1), 117–123 (2010).

[135] Langford JI and Wilson AJC. *"Scherrer after 60 years - survey and some new results in determination of crystallite size".* J. Appl. Crystallogr. **11**(APR), 102–113 (1978).

[136] Krill CE and Birringer R. *"Estimating grain-size distributions in nanocrystalline materials from X-ray diffraction profile analysis".* Philos. Mag. A **77**(3), 621–640 (1998).

[137] Dash WC. *"Copper precipitation on dislocations in silicon".* J. Appl. Phys. **27**(10), 1193–1195 (1956).

[138] Seibt M, Griess M, Istratov AA, Hedemann H, Sattler A, and Schroter W. *"Formation and properties of copper silicide precipitates in silicon".* Phys. Status. Solidi. A **166**(1), 171–182 (1998).

[139] Nes E and Washburn J. *"Transmission electron microscope investigation of growth of copper precipitate colonies in silicon".* J. Appl. Phys. **44**(8), 3682–3688 (1973).

[140] Buljan M, Desnica UV, Ivanda M, Radic N, Dubcek P, Drazic G, Salamon K, Bernstorff S, and Holy V. *"Formation of three-dimensional quantum-dot superlattices in amorphous systems: Experiments and Monte Carlo simulations".* Phys. Rev. B **79**(3), 035310 (2009).

[141] Zhang ZY and Lagally MG. *"Atomistic processes in the early stages of thin-film growth".* Science **276**(5311), 377–383 (1997).

[142] Ratto F, Locatelli A, Fontana S, Kharrazi S, Ashtaputre S, Kulkarni SK, Heun S, and Rosei F. *"Diffusion dynamics during the nucleation and growth of Ge/Si nanostructures on Si(111)".* Phys. Rev. Lett. **vol.96, no.9**, 096103/1–4 (2006).

[143] Lee H, Johnson JA, He MY, Speck JS, and Petroff PM. *"Strain-engineered self-assembled semiconductor quantum dot lattices".* Appl. Phys. Lett. **78**(1), 105–107 (2001).

[144] Scardera G, Puzzer T, Perez-Wurfl I, and Conibeer G. *"The effects of annealing temperature on the photoluminescence from silicon nitride multilayer structures".* J. Cryst. Growth **310**(15), 3680–3684 (2008).

[145] Rafiq MA, Tsuchiya Y, Mizuta H, Oda S, Uno S, Durrani ZAK, and Milne WI. *"Hopping conduction in size-controlled Si nanocrystals".* J. Appl. Phys. **100**(1), 014303 (2006).

[146] Durrani ZAK and Rafiq MA. *"Electronic transport in silicon nanocrystals and nanochains"*. Microelectron. Eng. **86**(4-6), 456–466 (2009).

[147] Puglisi RA, Vecchio C, Lombardo S, Lorenti S, and Camalleri MC. *"Charge transport in ultrathin silicon rich oxide/SiO_2 multilayers under solar light illumination and in dark conditions"*. J. Appl. Phys. **108**(2), 023701 (2010).

[148] Yu D, Wang CJ, Wehrenberg BL, and Guyot-Sionnest P. *"Variable range hopping conduction in semiconductor nanocrystal solids"*. Phys. Rev. Lett. **92**(21), 216802 (2004).

[149] Yildiz A, Serin N, Serin T, and Kasap M. *"Crossover from Nearest-Neighbor Hopping conduction to Efros-Shklovskii Variable-Range Hopping conduction in hydrogenated amorphous silicon films"*. Jpn. J. Appl. Phys. **48**(11), 111203 (2009).

[150] Riera M, Rodriguez JA, Barreto J, and Dominguez C. *"Modeling of non-stoichiometric silicon oxides obtained by plasma enhanced chemical vapour deposition process"*. Thin Solid Films **515**(7-8), 3380–3386 (2007).

[151] Kushner M. *"Plasma chemistry of $He/O_2/SiH_4$ and $He/N_2O/SiH_4$ mixtures for remote plasma-activated chemical-vapor-deposition of silicon dioxide"*. J. Appl. Phys. **74**(11), 6538–6553 (1993).

[152] Smith D. *"Controlling the plasma chemistry of silicon-nitride and oxide deposition from silane"*. J. Vac. Sci. Technol. A **11**(4, Part 2), 1843–1850 (1993).

[153] Rath JK, Liu Y, Brinza M, Verkerk A, van Bommel C, Borreman A, and Schropp REI. *"Recent advances in very high frequency plasma enhanced CVD process for the fabrication of thin film silicon solar cells"*. Thin Solid Films **517**(17), 4758–4761 (2009).

[154] Chowdhury A, Mukhopadhyay S, and Ray S. *"Effect of electrode separation on PECVD deposited nanocrystalline silicon thin film and solar cell properties"*. Sol. Energ. Mat. Sol. C. **94**(9, Sp. Iss. SI), 1522–1527 (2010).

[155] Hsieh S, Chang C, and Hsu S. *"Characteristics of low temperature and low energy plasma enhanced chemical vapor deposited SiO_2"*. J. Appl. Phys. **74**(4), 2638–2648 (1993).

[156] Batey J and Tierney E. *"Low-temperature deposition of high-quality silicon dioxide by plasma-enhanced chemical vapor-deposition"*. J. Appl. Phys. **60**(9), 3136–3145 (1986).

[157] Stasiak J, Batey J, Tierney E, and Li J. *"High-quality deposited gate oxide MOSFETs and the importance of surface preparation"*. IEEE Electr. Device. L. **10**(6), 245–248 (1989).

[158] Batey J, Tierney E, and Nguyen T. *"Electrical characteristics of very thin SiO_2 deposited at low substrate temperatures"*. IEEE Electr. Device. L. **8**(4), 148–150 (1987).

[159] Silalahi STH, Yang HY, Pita K, and Mingbin Y. *"Rapid thermal annealing of sputtered silicon-rich oxide/SiO_2 superlattice structure"*. Electrochem. Solid St. **12**(4), K29–K32 (2009).

[160] Iwayama TS, Hama T, Hole DE, and Boyd IW. *"Enhanced luminescence from encapsulated silicon nanocrystals in SiO_2 with rapid thermal anneal"*. Vacuum **81**(2, Sp. Iss. SI), 179–185 (2006).

[161] Koukos K, Bedel-Pereira E, Gauthier-Lafaye O, Scheid E, Bouscayrol L, Franc B, Arguel P, Bonnefont S, Lozes-Dupuy F, and Sarrabayrouse G. *"Effect of annealing conditions on photoluminescence properties of low-pressure chemical vapour deposition-grown silicon nanocrystals"*. Jpn. J. Appl. Phys. **47**(1, Part 1), 130–132 (2008).

[162] Iacona F, Bongiorno C, Spinella C, Boninelli S, and Priolo F. *"Formation and evolution of luminescent Si nanoclusters produced by thermal annealing of SiO_x films"*. J. Appl. Phys. **95**(7), 3723–3732 (2004).

[163] Scardera G, Bellet-Amalric E, Bellet D, Puzzer T, Pink E, and Conibeer G. *"Formation of a Si-Si_3N_4 nanocomposite from plasma enhanced chemical vapour deposition multilayer structures"*. J. Cryst. Growth **310**(15), 3685–3689 (2008).

[164] Hiller D, Goetze S, and Zacharias M. *"Rapid thermal annealing of size-controlled Si nanocrystals: Dependence of interface defect density on thermal budget"*. J. Appl. Phys. **109**(5), 054308 (2011).

[165] French P. *"Polysilicon: a versatile material for microsystems"*. Sensor. Actuat. A-Phys. **99**(1-2), 3–12 (2002).

[166] Faggin F and Klein T. *"Silicon gate technology"*. Solid-State Electron. **13**(8), 1125–1130 (1970).

[167] "The Intel 4004 - Silicon Gate Technology - a testimonial from Federico Faggin its designer, on the first microprocessor's thirtieth birthday". URL `http://www.intel4004.com/sgate.htm`.

[168] Kim H, Gilmore C, Pique A, Horwitz J, Mattoussi H, Murata H, Kafafi Z, and Chrisey D. *"Electrical, optical, and structural properties of indium-tin-oxide thin films for organic light-emitting devices"*. J. Appl. Phys. **86**(11), 6451–6461 (1999).

[169] Minami T. *"Transparent conducting oxide semiconductors for transparent electrodes"*. Semicond. Sci. Technol. **20**(4), S35–S44 (2005).

[170] Hossain SM, Anopchenko A, Prezioso S, Ferraioli L, Pavesi L, Pucker G, Bellutti P, Binetti S, and Acciarri M. *"Subband gap photoresponse of nanocrystalline silicon in a metal-oxide-semiconductor device"*. J. Appl. Phys. **104**(7), 074917 (2008).

[171] Prezioso S, Anopchenko A, Gaburro Z, Pavesi L, Pucker G, Vanzetti L, and Bellutti P. *"Electrical conduction and electroluminescence in nanocrystalline silicon-based light emitting devices"*. J. Appl. Phys. **104**(6), 063103 (2008).

[172] Sah CT. *Fundamentals of Solid-State Electronics*. World Scientific Publishing Co. Pte. Ltd., (1992).

[173] Fleetwood D. *"'Border traps' in MOS devices"*. IEEE T. Nucl. Sci. **39**, 269–271 (1992).

[174] Fleetwood D, Winokur P, Reber R, Meisenheimer T, Schwank J, Shaneyfelt M, and Riewe L. *"Effects of oxide traps, interface traps, and border traps on metal-oxide-semiconductor devices"*. J. Appl. Phys. **73**(10, Part 1), 5058–5074 (1993).

[175] Sze S. *Physics of Semiconductor Devices*. John Wiley & Sons, Inc, (1981).

Appendix A

Quantum Confinement in Nanocrystals

A simplified approach to understanding confined electrons is by using the famous *particle-in-a-box* problem of quantum mechanics in a 1-D case which can be solved for energies and wavefunctions using the *Schrödinger equation*. The time-independent Schrödinger equation is given by:

$$\left[-\frac{\hbar^2}{2m}\nabla^2(\vec{r}) + V(\vec{r})\right]\psi(\vec{r}) = E\psi(\vec{r}) \tag{A.1}$$

where $\mid \psi(\vec{r}) \mid$ is the wave function that describes the behaviour of an electron in space.
$(\mid \psi(\vec{r}) \mid)^2$ is the probability to find an electron at position $\vec{r}$.
$\nabla^2 = \frac{\delta^2}{\delta x^2} + \frac{\delta^2}{\delta y^2} + \frac{\delta^2}{\delta z^2}$ is the Laplacian operator.

To demonstrate the presence of discrete energy levels, we first start with the particle-in-a-box problem in a 1-D case. Let us assume that the electron is confined to a volume of solid material (a box), which can be modeled as a potential well of size a with infinitely high walls as depicted in Figure A.1a. The Schrödinger equation in 1D (having only an x component) is then given by:

$$\left[-\frac{\hbar^2}{2m}\right]\frac{\delta^2\psi(x)}{\delta x^2} = E\psi(x) \tag{A.2}$$

The wave function of the electron must be continuous at the walls of the well. Therefore, the boundary conditions are that the probability to encounter the electron outside the

box, or at its boundaries is zero.

$$| \psi(0) |^2 = | \psi(a) |^2 = 0 \Rightarrow \psi(0) = \psi(a) = 0 \tag{A.3}$$

This is just a second order differential equation, whose trial-solution is given by:

$$\psi(x) = Asin(kx) + Bcos(kx) \tag{A.4}$$

Using the boundary conditions from Equation A.3 in Equation A.4, we get $B = 0$ and

$$\psi(a) = Asin(ka) = 0 \Rightarrow ka = n\pi \Rightarrow k = \frac{n\pi}{a} \; where \, n = 1,2,3,... \tag{A.5}$$

Substituting Equation A.5 in Equation A.2 after double differentiating, we get the solution:

$$E = \frac{\hbar^2 k^2}{2m} = \frac{\hbar^2 n^2 \pi^2}{2ma^2} \tag{A.6}$$

Equation A.6 shows the nature of the energy states as $n = 1, 2, 3...$ corresponds to the discrete excitation levels. The allowed energies are discrete (as shown in Figure A.1b) and are represented in the *E-k diagram*. As a decreases, the energy levels become more widely spaced. And when a is in the range of the *Bohr exciton radius*, i.e. the natural separation between electron-hole pairs, spatial electron confinement results in the quantization of energy levels.

For the case of quantum dots, we extend this argument in three dimensions. The Schrödinger equation as defined in Equation A.2 will now have x, y and z components. On solving, we get the allowed values of k as

$$k_i = \frac{n_i \pi}{a}, \; where \, i = x,y,z \tag{A.7}$$

Similarly, the energy is given by:

$$E = \frac{\hbar^2 \pi^2}{2m} \frac{({n_x}^2 + {n_y}^2 + {n_z}^2)}{a^2} \tag{A.8}$$

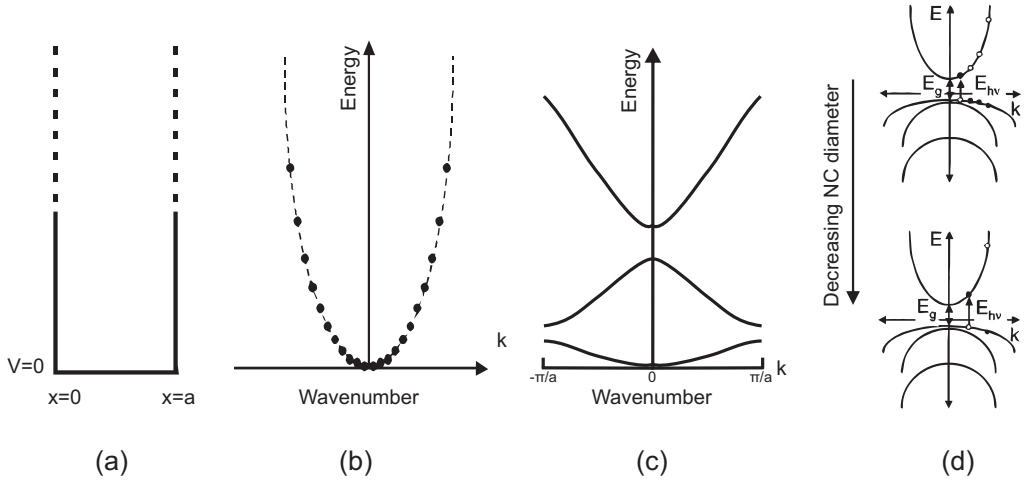

Figure A.1: a) depicts an infinite potential well. b) The E-k diagram shows the discrete energies as only certain values of k are allowed, as seen from equation A.6. c) represents the E-k diagram showing the formation of energy gaps; d) shows the E-k diagram modelled for quantum dots. As the size of the quantum dots decreases, the bandgap increases and the allowed energy levels also become more widely spaced.[a]

Considering a cubic box, for $n = n_x = n_y = n_z$,

$$E = 3\frac{\hbar^2\pi^2}{2m}\frac{n^2}{a^2} \tag{A.9}$$

The extra factor of 3 comes in due to 3D confinement. For a given confined energy level, a quantum dot has a diameter which is $\sqrt{3}$ the width of the corresponding quantum well. This is just a simple treatment considered here for confinement in a cubic quantum dot. In reality, the potential barrier is not an infinite cubic box but rather a finite spherical well[b].

For a spherical quantum dot of diameter a the confinement is slightly greater and the factor slightly larger than $\sqrt{3}$. Also, some other factors that should be noted in this approximation are that the "particle" in a box is not a single electron, but rather multiple excitons. Additionally, this "box" is not empty, and the electron is instead confined to a semiconductor lattice of finite dimensions[c]. In spite of these assumptions, we can approximate fairly well the change in diameter with size for quantum confined systems.

[a]Murray CB, Kagan CR and Bawendi MG CB, Kagan CR and Bawendi MG. Annu. Rev. Mater. Sci. 30, 545-610 (2000)
[b]Brus LE. J. Chem. Phys. 80, 4403 (1984)
[c]Efros AL and Rosen M. Annu. Rev. Mater. Sci. 30, 475-521 (2000)

Appendix B

Experimental Design

Run ♯	A N_2O sccm	B SiH_4 sccm	C Pressure Torr	D Power Watt	E Time sec	Thickness nm	Rate nm/s	n -
1*	32	15	6	82	6.5	7.86	1.21	2.11
2	48	24	9	50	10	15.63	1.56	2.05
3	16	6	9	50	10	8.26	0.83	1.56
4	48	6	3	82	3	2.85	0.95	2.17
5	32	24	3	114	3	3.98	1.33	2.36
6	48	6	3	50	10	6.61	0.66	1.56
7	16	15	3	114	10	9.79	0.98	2.21
8	48	24	3	114	10	12.28	1.23	1.96
9	16	24	9	50	3	4.28	1.43	2.12
10	16	6	3	50	3	2.26	0.75	2.11
11	48	6	9	114	10	8.32	0.83	1.52
12*	32	15	6	82	6.5	7.86	1.21	2.09
13	32	15	9	82	6.5	9.79	1.51	1.64
14	48	24	3	50	3	3.16	1.05	2.15
15	48	6	9	50	6.5	6.41	0.99	1.56
16	16	6	9	114	3	3.16	1.05	1.81
17	16	15	6	82	6.5	7.05	1.09	1.99
18	16	24	3	50	10	5.94	0.59	2.58
19	48	24	9	114	3	6.27	2.09	1.79
20	16	6	3	114	6.5	5.4	0.83	1.67
21	16	6	9	50	10	8.5	0.85	1.59
22	16	24	9	114	10	15.29	1.53	2.2
23	48	15	3	114	3	3.89	1.3	1.89
24	48	6	6	50	3	2.99	1	1.79
25*	32	15	6	82	6.5	7.91	1.22	2.09
26	16	14	5.5	115	3	4.2	1.4	1.99
27	16	14	5.5	115	10	11.18	1.12	1.99

Table B.1: Runs used in the D-Optimal design. Run 1, 12 and 25 were repeated for testing the reproducibility of the process. All runs were performed with helium gas flow 1900 sccm, inter-electrode distance 400 mils, chamber temperature 480°C and rf frequency 13.56 MHz.

Complete quadratic equation with interactions for controlling layer thickness with different deposition parameters in plasma enhanced chemical vapour deposition.

$$
\begin{aligned}
Thickness \;=\; & -1.72843 \\
& +0.17950 \times N_2O \\
& -0.14348 \times SiH_4 \\
& +0.12613 \times Pressure \\
& +0.024671 \times Power \\
& -0.093852 \times time \\
& +4.24270 \times 10^{-3} \times N_2O \times SiH_4 \\
& -4.17773 \times 10^{-3} \times N_2O \times Pressure \\
& -9.20602 \times 10^{-4} \times N_2O \times Power \\
& +2.88742 \times 10^{-3} \times N_2O \times time \\
& +0.029700 \times SiH_4 \times Pressure \\
& +1.45454 \times 10^{-3} \times SiH_4 \times Power \\
& +0.025286 \times SiH_4 \times time \\
& -3.64812 \times 10^{-3} \times Pressure \times Power \\
& +0.049997 \times Pressure \times time \\
& +3.23809 \times 10^{-3} \times Power \times time \\
& -2.00590 \times 10^{-3} \times N_2O^2 \\
& -9.70800 \times 10^{-3} \times SiH_4^2
\end{aligned}
$$

Complete quadratic equation with interactions for controlling deposition time in plasma enhanced chemical vapour deposition of silicon rich oxides, calculated using

Design of Experiments.

$$
\begin{aligned}
Deposition\ Rate \;=\; & +0.60376 \\
& -1.11680 \times 10^{-3} \times N_2O \\
& +0.013775 \times SiH_4 \\
& +0.027425 \times Pressure \\
& +1.17616 \times 10^{-3} \times Power \\
& -0.030699 \times time \\
& +4.22927 \times 10^{-4} \times N_2O \times SiH_4 \\
& +4.34268 \times 10^{-3} \times SiH_4 \times Pressure \\
& +2.49948 \times 10^{-4} \times SiH_4 \times Power \\
& -2.84443 \times 10^{-3} \times Pressure \times Power \\
& -1.61863 \times 10^{-3} \times SiH_4^2
\end{aligned}
$$

Résumé en Français

Ce travail traite de l'élaboration et de la caractérisation de boîtes quantiques de silicium dans une matrice de SiO_2 pour des applications photovoltaïques.

Les Nanocristaux de Silicium

Les technologies à base de matériaux semi-conducteurs sont présentes dans tous les produits électroniques modernes. La technologie CMOS (Complementary Metal Oxide Semiconductor) est une technologie de fabrication de composants électroniques. Le silicium, avec sa bande d'énergie interdite de 1.12 eV, est au cœur des technologies modernes dans le monde de la microélectronique. Malgré son gap indirect, le silicium est le matériau majoritairement utilisé dans le monde du photovoltaïque.

Du fait de son gap indirect, le silicium est un émetteur inefficace de la lumière. Historiquement, il n'était pas utilisé pour les applications optiques. La découverte de l'émission de la lumière dans le silicium poreux et nanostructuré a permis plusieurs applications potentielles, transversales aux domaines de la microélectronique, le photovoltaïque et la photonique. Ces applications incluent notamment les mémoires non-volatiles, les lasers, les diodes électroluminescentes (LED), et les cellules photovoltaïques de troisième génération qui sont le principal objet de cette thèse.

L'amélioration des propriétés optiques du silicium a été obtenue grâce au confinement quantique des électrons et des trous dans l'espace, en permettant de réduire les recombinaisons non-radiatives dans le silicium. Dans une boîte quantique (ou nanocristal), ce confinement se fait dans les trois directions de l'espace lorsque la taille du

nanocristal est inférieure au rayon de Bohr de l'exciton, qui est voisine de 5 nm pour le silicium. Une autre conséquence, due au confinement quantique, est le changement de gap du silicium lorsque la taille des nanocristaux diminue. Les nanocristaux sont noyés dans une matrice diélectrique à base de silicum, telles que SiO_2, Si_3N_4 et SiC. La distance entre les nanocristaux étant supposée d'être suffisamment faible pour permettre la conduction électrique à travers une matrice diélectrique.

Les technologies à base de nanocristaux de silicium sont à la fois compatible avec les technologies CMOS de la microélectronique et les technologies de l'industrie photovoltaïque, puisque la plupart des cellules/panneaux PV commerciaux sont principalement à base de silicium massif. Une grande partie des pertes dans une cellule à simple jonction solaire est due à la thermalisation des porteurs chauds et des photons non absorbés. L'efficacité d'une cellule solaire à simple jonction se trouve ainsi limitée à la valeur théorique de 31%, plus connue comme la limite Shockley Queisser.

Cette limite peut être dépassée, en utilisant des dispositifs multi-jonctions avec des nanocristaux de silicium dont le gap est contrôlé. Outre ces cellules tandem solaire, d'autres cellules peuvent être réalisées comme les cellules de porteurs chauds, la génération de multi-excitons, etc.

Avant l'incorporation de ces boîtes quantiques dans les dispositifs réels, il est important d'examiner leurs techniques de fabrication, leur structure, ainsi que leurs propriétés optiques et électriques.

Développement de Monocouches avec Nanocristaux de Silicium

Les nanocristaux de silicium sont fabriqués par la technique de Dépôt Chimique en Phase Vapeur assisté par Plasma (PECVD) avec les précurseurs SiH_4 et N_2O. Ces précurseurs réagissent pour former un oxyde de silicium, sous-stœchiométrique en oxygène, donc contenant un excès de silicium (SiO_x, $x < 2$). Trois couches d'épaisseur 30 nm (Q30), 50 nm (Q50) et 75 nm (Q75) ont été réalisées dans les mêmes conditions de dépôt.

Le recuit, à haute température, de ces couches enrichies en silicium, permet la séparation des phases, formant ainsi du silicium et de l'oxyde de silicium stœchiométrique (SiO_2). Pour les échantillons composés d'une seule couche épaisse, la taille des nanocristaux et la distance entre chacun d'eux n'est pas contrôlée. Par conséquent, les boîtes quantiques noyées dans la matrice d'oxyde SiO_2 sont aléatoirement réparties.

Les propriétés structurelles de ces films peuvent être évaluées par FTIR et ellipsométrie. La technique de Spectroscopie Infrarouge à Transformée de Fourier (FTIR) est utilisée pour évaluer l'enrichissement en silicium de ces couches (SiO_x, $x = 1.56$). Ceci est fait en utilisant le pic de l'élongation des liaisons Si-O qui se déplace en fonction de l'excès de silicium. De plus, ce pic confirme, après le recuit, la séparation des phases Si et SiO_x , en montrant la transition de SiO_x en SiO_2 et Si. L'ellipsométrie spectroscopique est une autre méthode rapide et sans-contact. Cette technique est utilisée pour estimer l'enrichissement en silicium dans ces couches à l'aide de la mesure des indices optiques, et permet de déterminer la fraction de chaque matériau (a-Si, c-Si et SiO_2) après le recuit.

Les propriétés des boîtes quantiques de silicium, i.e. la taille des nanocristaux, le gap correspondant, la cristallinité, les propriétés optiques, etc. peuvent aussi être évaluées. La spectroscopie de photoluminescence montre que le gap augmente jusqu'à 1.45 eV, ce qui est supérieur à celui du silicum massif, et confirme ainsi l'hypothèse du confinement quantique. La diffractométrie par rayons X en incidence rasante montre les pics de Si cristallin, et confirme que les boîtes quantiques ont une structure cristalline. La largeur à mi-hauteur des pics nous permet d'évaluer la taille des grains (i.e. les nanocristaux). La technique de Microscopie Electronique en Transmission (TEM) permet de visualiser les boîtes quantiques, et donne une estimation de leur densité et de leur taille.

L'ensemble de ces trois techniques peuvent être utilisées pour évaluer la taille moyenne des nanocristaux, qui a été trouvée voisine de 5 nm. Cependant, une grande distribution de tailles et la présence d'éventuels défauts luminescents empêchent une évaluation précise.

Organisation des Nanocristaux de Si dans les Monocouches

Les nanocristaux formés après le recuit à haute température ont un grand nombre de défauts (fautes d'empilement, dislocations). Il est connu que dans le silicium, le cuivre a une forte affinité pour les dislocations. Du cuivre a donc été déposé sur les échantillons au cours de la préparation des lames TEM pendant le polissage. Ce cuivre s'est déposé précisément sur les zones où des nanocristaux de silicium étaient présents ; cela nous a permis d'évaluer l'organisation des nanocristaux dans la matrice d'oxyde SiO_2.

Une organisation des nanocristaux de Si a été observée selon l'épaisseur des couches. Une organisation différente est observée pour les 3 couches, malgré leur stœchiométrie identique. Dans le cas de la couche la plus mince de 30 nm (Q30), les boîtes quantiques sont aléatoirement organisées dans l'oxyde, alors que pour la couche de 75 nm d'épaisseur (Q75), une organisation quasi-hexagonale est observée, montrant un super-réseau des nanocristaux.

Cette organisation peut être attribuée à la diffusion du silicium dans les couches de SiO_x, pendant l'étape de recuit. Pour les conditions de recuit et d'enrichissement de silicium utilisées dans ce chapitre, la longueur de diffusion de Si a été évaluée à 12 nm. Les interfaces de la couche et les limites de la couche mince Q30 sont susceptibles de jouer un rôle important dans la limitation de la diffusion de Si, formant des dots dans un ordre aléatoire. Dans le cas de la couche Q75, la diffusion est moins susceptible d'être affectée par les limites, conduisant à l'auto-organisation de boîtes quantiques de silicium.

Les différences observées dans l'organisation des boîtes quantiques ont également une conséquence sur la conductivité électrique et les mécanismes de conduction associés. Ils ont été évalués par des mesures courant-tension à température ambiante, et à basse température. Les mécanismes de conduction montrent de la conduction par Hopping qui dépend de la température pour les couches Q30 avec organisation aléatoire des nanocristaux. Pour l'échantillon Q75, avec des nanocristaux ordonnés, la température n'a pas d'influence sur la conductivité, représentatif d'une conduction tunnel. Cependant, la

conductivité la plus faible est observée dans les couches Q75. Par effet, elle peut être attribuée à une distance entre nanocristaux bien plus uniforme, bloquant la conduction tunnel.

Par ailleurs, les mesures de capacité-tension démontrent l'élargissement de l'hystérésis sous éclairage qui peut être attribué à la génération des porteurs par la lumière dans Q75. Ceci est un résultat positif pour l'intégration des nanocristaux de Si dans les dispositifs photovoltaïques.

Des Monocouches aux Multicouches

Des monocouches épaisses d'oxyde enrichi en silicium permettent la formation non contrôlée de boîtes quantiques dans une matrice de SiO_2. Ce problème peut être surmonté en utilisant des alternances de bicouches (multicouches) d'oxyde de silicium enrichi et de SiO_2. La distance entre les nanocristaux est désormais contrôlée précisément, dans une direction de l'espace, par l'épaisseur de la couche de SiO_2, et la taille des dots est limitée par l'épaisseur de la couche d'oxyde de silicium enrichie.

Cependant, la fabrication à grande échelle de ces structures est difficile dans un réacteur PECVD industriel, les vitesses de dépôt étant de l'ordre de 1 nm/s. Plusieurs paramètres jouent un rôle dans le contrôle de la vitesse de dépôt et de l'enrichissement de silicium.

Un Plan d'Expériences a été réalisé afin d'établir un modèle complet du second degré, montrant l'influence des débits de SiH_4 et de N_2O, de la puissance du plasma, de la pression de la chambre et du temps de dépôt sur l'épaisseur de la couche, la vitesse du dépôt et l'indice de réfraction, ce dernier étant lié à l'enrichissement en Si de la couche. Les autres paramètres comme le flux d'hélium et la distance inter-électrodes ont été maintenus constants.

Le débit de silane et la pression de la chambre ont été identifiés comme étant les paramètres dont l'influence est la plus grande sur le procédé de dépôt. Ces paramètres

permettent de déterminer les conditions nécessaires pour obtenir l'épaisseur et l'enrichissement désirées.

Des échantillons avec 10 bicouches (3 nm de SiO_x et 1.5 nm de SiO_2) ont été réalisés et recuits à 1000, 1050 et 1100 ° C pendant 5, 20 et 60 minutes. Une analyse des conditions de recuit montre des débuts de photoluminescence à partir de 1100°C, dont l'intensité augmente avec le temps de recuit. Les images TEM montrent également une séparation visible de SiO_x en Si et SiO_2. Cependant, l'environnement du film joue un rôle majeur dans la formation des nanocristaux. Nous avons observé que la photoluminescence dépend fortement de l'épaisseur de la couche de SiO_2, du nombre d'alternances dans les multicouches etc. Ces différences peuvent apparaître à cause des contraintes existant dans les boîtes quantiques, la quantité de silicium cristallin et de l'amorphe etc.

Caractérisations Optiques et Electriques des Nanocristaux de Silicium

Les nanocristaux de silicium avec des bandes interdites contrôlées ont été fabriqués en utilisant des dépôts multicouches sur une grande échelle (sur des plaques 200 mm). Des caractérisations électriques ont été réalisées avec des matériaux différents pour l'électrode, pour s'assurer que la réponse est celle des boîtes quantiques et non celle de la jonction métal-oxyde-semiconducteur. Les différentes électrodes utilisées sont d'aluminium, de silicium polycristallin dopé B dans des dispositifs de type p-i-n, ainsi que l'électrode transparente et conductrice (l'ITO) dans les dispositifs de type n-i-p.

En comparaison avec les monocouches épaisses, une mauvaise conductivité électrique à température ambiante de moins de $10^{-14}\mathrm{m}\Omega^{-1}\mathrm{cm}^{-1}$ a été observée dans les multicouches. Cela peut être attribué à une distance trop grande mais uniforme entre les nanocristaux, malgré un contrôle soigneux pendant le processus de dépôt. Cela se produit car la taille des nanocristaux peut être plus petite que l'épaisseur de la couche de SiO_x ; ce qui augmente la distance effective entre les dots. De plus, un grand nombre d'états d'interface et des défauts peuvent introduire des pièges dans les multicouches.

La conductivité électrique dans les deux types de couches est indépendante de la température pour des champs faibles, et suit la conduction Poole-Frenkel pour des champs électriques élevés. Les échantillons avec des électrodes d'ITO transparentes ont ensuite été utilisés pour évaluer la réponse spectrale. La photosensibilité est améliorée dans la région bleu-vert du spectre pour les multicouches, avec des efficacités quantiques externes élevées allant jusqu'à 55 %. Les monocouches épaisses montrent une mauvaise réponse optique, bien que leur sensibilité dans la région de longueur d'onde bleue-verte est toujours présente.

Conclusion

Nous avons réussi à améliorer soit la conduction électrique, soit l'absorption optique dans des couches de silice à nanocristaux de silicium. Ce sont des résultats positifs pour toutes les applications photovoltaïques, mais il est nécessaire de travailler sur l'amélioration simultanée de ces deux propriétés, qui sont exigées pour l'intégration photovoltaïque.